Deformation of Al_3Ti Base Intermetallic Phases:

A Contribution to the Evaluation of the Mechanical Properties and of the Mechanisms of Deformation

Thèse présentée à l'Institut de Métallurgie Structurale

Université de Neuchâtel

Pour l'obtention du titre de Docteur ès Sciences

par

Reto Lerf

Ing. en science des Matériaux ETHZ

Directeur de thèse: Prof. D.G. Morris

Novembre 1992

im Andenken an meine Mutter ...

IMPRIMATUR POUR LA THÈSE

A contribution of the Evaluation of the Mechanical Properties and of the Mechanisms of Deformation

de M. Reto Lerf

UNIVERSITÉ DE NEUCHÂTEL

FACULTÉ DES SCIENCES

La Faculté des sciences de l'Université de Neuchâtel
sur le rapport des membres du jury,

MM. D.G. Morris, W. Form, P. Furrer (Alusuisse-Lonza, Neuhausen) et J.-L. Martin (EPF-Lausanne)

autorise l'impression de la présente thèse.

Neuchâtel, le 15 avril 1993

Le doyen :

A. Robert

Contents

1. Introduction

Encouraged by the discovery of the ductilisation of polycrystalline Ni_3Al other intermetallic compounds have attracted interest as structural materials for high temperature application. Therefore, during the late 1980's, research in intermetallic compounds formed by elements with low densities become increasingly more widespread. Lightweight, heat resistant materials will allow for weight saving in all kinds of combustion engines, particulary gas turbines, and in the fuselage of future space aircraft. The weight reduction in these compounds would lead to fuel savings and an increase in pay-load.

One example of such a material can be found in the group of the Al_3X-based aluminides, where X is a group IVB or VB transition metal. Due to their high aluminium content, they have low densities (generally below 4 gcm^{-3}) and a protective Al_2O_3 layer at the surface, which leads to good oxidation and corrosion resistance. In spite of their high aluminium content, they exhibit a high melting point: $T_m \geq 1300°C$. Unfortunately, the binary Al_3X phases are daltonides and, in addition, they melt incongruently. Therefore, their preparation causes some difficulties. The earliest works published on these intermetallics reported an extreme britleness at low temperatures and related the britle behaviour to the tetragonal crystal structure which exhibits an unsufficient number of deformation systems. Cubic trialuminides had been proposed to augment the number of active deformation systems.

This was the state of knowledge at the beginning of the following thesis. The goal and challenge of the research was to understand the mechanisms which relate the microstructure to the mechanical properties of these trialuminides. With this knowledge, improved materials with properties meeting the demands of industry can be designed and brought to the weight saving applications mentioned.

Other, obvious methods to improve the ductility are embedding the brittle material in a ductile matrix or reinforcing the brittle material with a ductile second phase. Both types of two phase materials, in which Al_3X-based aluminides form the hard but brittle phase, can be prepared by powder metallurgy techniques. These two phase materials will be presented in a separate chapter.

2. Literature Review

2.1 Fundamental Properties of Al_3X-Base Intermetallic compounds

2.1.1 Structural Relationships

The most important long period ordered structures in the Al_3Ti base intermetallic compounds are the DO_{22} (Strukturbericht designation), or tI8 (Pearson symbol), and the $L1_2$, or cP4, structures. The Al_3Ti phase and, for example, Al_3V, Al_3Nb and Al_3Ta form crystals with the DO_{22} structure. Al_3Sc and ternary alloyed Al_5Ti_2M (where, for example, M = Cr, Mn, Fe, Co, Ni and Cu) crystallize in the $L1_2$ structure. Both unit cells are closely related, i.e. the tetragonal DO_{22}-type structure is derived from the cubic $L1_2$-type structure by introducing an antiphase boundary (APB) with a displacement vector of the type $^1/_2$ [110] on every (001) plane, as shown in figure 2.1.

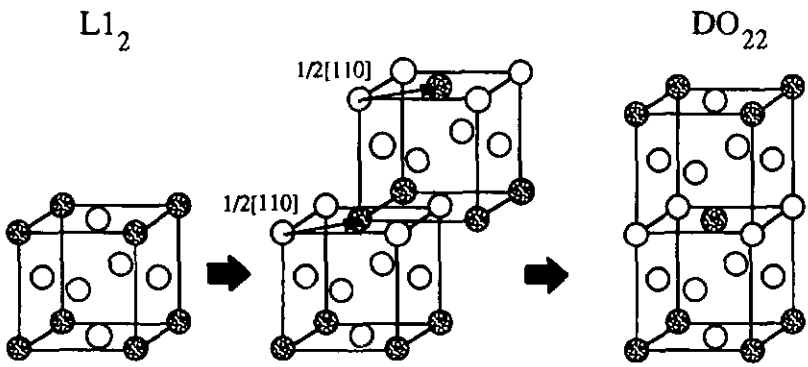

Figure 2.1: Structures of the types $L1_2$ and DO_{22}. The DO_{22} structure can be derived from $L1_2$ by an APB on each even (001) plane. Open circles represent Al, shaded circles represent Ti.

Electronic model simulations by Nicholson et al. [1] suggest that the tetragonal distortion of the lattice for Al_3Ti ($^c/_a = 2.23$) stabilizes the DO_{22} structure. For a trialuminide with the ideal $^c/_a$ ratio of 2, the energetically favorable structure would be $L1_2$. Exactly this effect, i.e., lowering the $^c/_a$ ratio, results when Al_3Ti is alloyed with an element out of the group of d transition metals mentioned above. Complementary, Eberhart, Kumar and MacLaren [2] find that dilute alloying of Cr, Mn, Fe introduces an amount of d character into the aluminium sp-bonding region of Al_3Ti type compounds. The d states are localized in energy and firstly, increase the

isotropy of the bonding (reducing the $^c/_a$ ratio) and, secondly, induce preferential ordering of the second neighbour Al atoms consistent with the $L1_2$ crystal structure.

The discrete variational Xα cluster calculations are accomplished for γ TiAl by Morinaga, Saito, Yukawa and Adachi [3]. The addition of certain third elements, M, weakens the Al*p* - Ti*d* interactions but enhances *d-d* bonding in terms of M*d* - Ti*d* interactions. The *p-d* covalent bonds with the lower coordination number are highly directional. High directionality of the bonds increases the shear strength and gives a large barrier to shear deformation. The simulations by Morinaga et al. show that the M*d* - Ti*d* interactions increase and the M*d* - Al*p* interactions decrease in the order of decreasing atomic number between Cu and V. Since V alloyed trialuminides crystalize in the DO_{22} structure, Al_5Ti_2Cr and Al_5Ti_2Mn are expected to have the lowest strength and the most symmetrical properties, as far as the results for TiAl based intermetallics can be transfered to Al_3Ti based alloys.

The Pettifor structure map for A_3B compounds shows pseudobinary Al_3Ti based phases exhibiting the DO_{22} or the $L1_2$ crystal structure in direct vicinity [4]. This map suggests that it should be possible to move from one structural domain to another by suitable addition of a third alloying element. Unfortunately, the Pettifor maps restrict only the number of the candidates for the third element, but it does not predict if a such alloyed phase exist, if this ternary compound exhibits really the $L1_2$ structure or at which amount the third element has to be added. Using Petnifors' criterion of the average Mendeleev numbers [4], the possible candidates for alloying elements to transform Al_3Ti into a trialuminide with $L1_2$ structure are the group VIA to group IIB transition metals. At least for the fourth row transition metals this prediction is correct.

However, the list of the transition metals which, alloyed to about 10 at-%, change the tetragonal DO_{22} lattice of Al_3Ti into the cubic $L1_2$ long range ordered structure is not complete and still under investigation. In 1965, Raman and Schubert [5] publishes a work on the constitution of some alloys related to Al_3Ti. This paper reports the $L1_2$ crystal structure of $Al_{62}Ti_{25}Cu_{13}$ and $Al_{67}Ti_{25}Ni_8$. Later, in 1981, Seibold finds in her research on the ternary Al-Ti-Fe system [6] the phase $Al_{22}Ti_8Fe_3$, which forms $L1_2$ crystals. Only in the last few years, the $L1_2$ stabilizing effect of Co [7], Mn [8] and Cr [9] is discovered.

2.1.2 Deformation Systems

Considering a fcc lattice as a base for the explanation of the Burgers vectors, in the ordered $L1_2$ superstructure, the dislocation with $b = {}^a/_2\langle 110\rangle$ is only a partial of a so called superdislocation (see figure 2.2). The whole Burgers vector of the superdislocation is $b = a\langle 110\rangle$. The dissociation of the superdislocation means that an APB ribbon is spread out between the two

superpartials. Moving this dislocation, the leading partial will create an order fault, which will be annihilated by the trailing partial. The equilibrium separation of the pair of dislocations is determined by the balance between the elastic repulsion of the dislocation and the attraction caused by the APB and its energy. The usual glide plane for dislocations having a $^{a}/_{2}$<110> Burgers vector in a fcc lattice is the octahedral {111} type. In the ordered $L1_2$ structure, the same glide plane is found. However, the superdislocations may be able to cross-slip into cubic {100} planes as will be discussed in section 2.2.

Another Burgers vector lying in the cubic plane of the $L1_2$ crystal structure is possible, i.e. $b = a$<100>. A dislocation with this b is not dissociated and will glide in the {100} plane, i.e. a second closest-packed plane.

A simple energetical consideration explains which of the two glide systems mentioned above is more probable for $L1_2$ structures. Considering that the line tension of a dislocation is proportional to the square of the length of its Burgers vector, dissociation into two partials of $^{b}/_{2}$ means an decrease of the energy of a dislocation. In the point of view of this first order approximation both linear faults, the $b = {}^{a}/_{2}$<110> + $^{a}/_{2}$<110> superdislocation and the a<100> dislocation have the same energy. But the closest-packed {111} plane provides easier glide for the dissociated superdislocation, so that {111}<110> is the most favorable glide system at low temperatures.

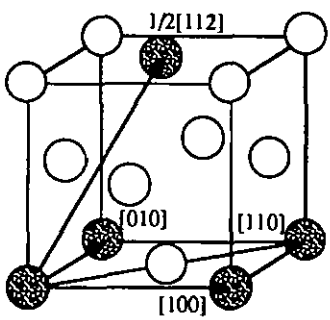

Figure 2.2: The possible Burgers vectors in DO_{22}. Those in the basal plane, <100], and <110] are identical to the Burgers vectors <100> and <110> found in $L1_2$. $^{1}/_{2}$<112] is also the twinning vector in DO_{22}. Only half of the DO_{22} unit cell is shown. Open circles represent Al, shaded circles represent Ti.

The basal plane of the DO_{22} and the $L1_2$ superstructure are identical. Hence, these two types of dislocation with Burgers vector lying in the (001) plane, are also found in the DO_{22} lattice, i.e.

$b = a[100]$ and $b = a[110]$. A third Burgers vector, namely $b = {}^{a}/_{2}\langle 112]$ * may exist. (See figure 2.2). The glide plane of a dislocation with $b = {}^{a}/_{2}\langle 112]$ would be {111}. But this is also the twinning system for deformation twins, with the four twinning planes {111} and ${}^{a}/_{6}\langle 11\bar{2}]$ shear vectors. This type of twin is called an ordered twin because it does not disturb the first nearest neighbour (NN) configuration in the DO_{22} structure. Three consecutive layers parallel to {111} composed of large, medium and small circles are shown in figure 2.3 to illustrate the NN configuration. Only shear in $[11\bar{2}]$ direction conserves the NN relations, $[1\bar{2}1]$ and $[\bar{2}11]$ are not equivalent.

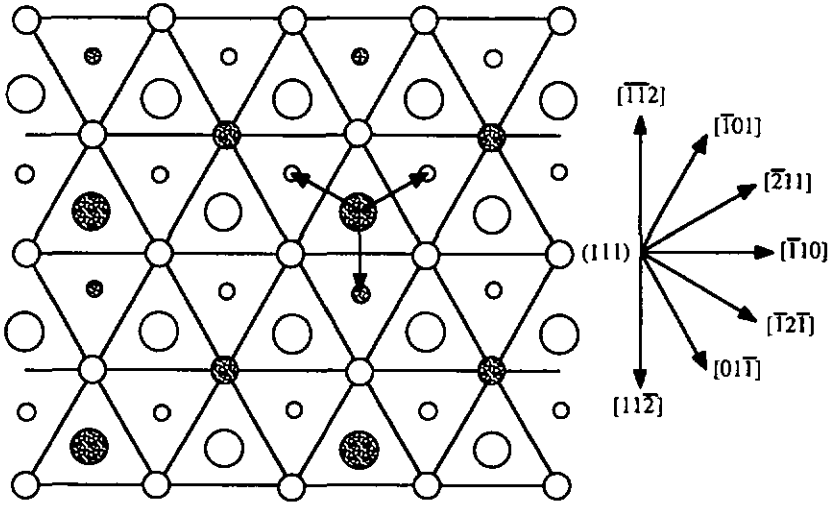

Figure 2.3 First nearest neighbour configuration in the DO_{22} structure. Three consecutive layers parallel to {111} are labelled with large, medium and small circles. Shear direction for the ordered twinning is $\langle 11\bar{2}]$. Open circles represent Al, shaded circles represent Ti.

2.1.3 Binary Al_3Ti

Aluminium and titanium form the compound Al_3Ti with exact stoichiometric composition. After the binary phase diagram Al-Ti [10], there is no detectable range of solid solubility. Hence, Al_3Ti is a so called Daltonide. It contains as single phase 75 at-% Al and 25 at-% Ti. A peritectic reaction at 1360 °C forms the intermetallic compound Al_3Ti, which solidifies directly

---

* : The mixed notations $\langle \ldots]$ and $(\ldots)$ mean that $L1_2$ indices are used for the tetragonal DO_{22} lattice, i.e. permutations are possible on the two first indices and the third one is fixed. For example, the ${}^{1}/_{2}[112]$ vector in figure 2.2 is in tetragonal notation ${}^{1}/_{2}[111]$.

in the DO_{22} structure. There is no order-disorder transition nor polymorphous reaction down to room temperature. The lattice parameters of the tetragonal DO_{22} structure are $a = 0.3848$ nm and $c = 0.8596$ nm, i.e. $^c/_a = 2.23$ [11]. The density p of Al_3Ti can be calculated as $p = 3.36$ gcm^{-3}. The binary phase diagram as proposed by Massalski and his co-editors [10] is shown in figure 2.4.

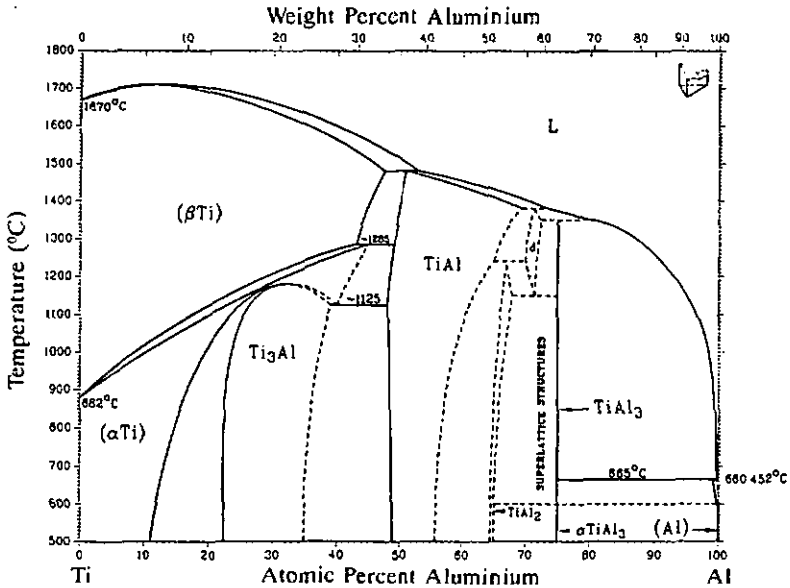

Figure 2.4 The Al-Ti binary phase diagram. The Ti-rich corner is still controversial. (After Masslaski and co-editors [10])

A systematic research undertaken on the mechanical properties of Al_3Ti and related compounds is first published by the group around Yamaguchi [12,13,14]. Their investigations comprise mainly high temperature compression testing, oxidation behaviour and TEM analysis. At temperatures up to 620 °C, Al_3Ti behaves in a brittle manner, which means that even in compression samples fail after only a few ‰ of plastic strain. The yield stress undergoes a sharp drop in the range of 400 °C to 600 °C, falling from about 170 MPa at low temperatures to about 70 MPa at high temperatures. The deformation mode at temperatures below 620 °C is ordered twinning of the type $\{111\}\langle 11\bar{2}\rangle$. Above 620 °C, good ductility in compression is observed, and the four $\{111\}\langle 11\bar{2}\rangle$ - type twinning systems are augmented by

slip along <110] and <100]. Yamaguchi explains the increase in fracture strain in terms of the von Mises criterion: Below 620 °C, only the four twinning systems carry the deformation. At higher temperature, dislocation slip becomes active and a greater number of deformation systems is available [12]. Hence, the von Mises criterion is fulfilled, i.e. at least five independent deformation systems are active and an uniform deformation of a polycrystal material is possible.

A crystal with the DO_{22} structure is not necessarily brittle. The Ni_3V phase exhibits the same crystal structure (a = 0.3542 nm, c = 0.7173 nm and $^c/_a$ =2.025 [11]) and the same ordered twinning is the important deformation mode at RT as in Al_3Ti, as is shown by Vanderschaeve and Sarrazin [15]. Although this material is characterized by a high yield stress and a high work hardening rate, good ductility in compression is observed, both for single crystals as well as for polycrystalline samples [16].

Again, it is Yamaguchi and his co-workers who propose ternary alloying additions to Al_3Ti to augment ductility [13]. Elements as Li, Zr and Hf are seen to improve room temperature ductility to some extent by promoting slip of <110] superdislocations on (001). On the other hand, elements like V improve ductility due to the increase of the activity of ordered twinning. However, for both types of alloying additions the ductility in compression does not exceed a few %. Such a poor ability of plastic deformation has no technical use and another method for improvement of ductility must be found.

2.1.4 Ternary Al_5Ti_2M Type Phases

A standard approach to achieve more ductility for a low symmetry polycrystal material as Al_3Ti is to augment its structural symmetry. As presented before, the tetragonal DO_{22} structure and the high symmetry, fcc based $L1_2$ structure are closely related. From the list of elements which alter the DO_{22} structure to a cubic Al_5Ti_2M type, this $L1_2$ phase is reported only in the Mn [8, 17], Fe [6, 18], Ni and Cu [5, 18] containing ternary equilibrium diagrams. From these ternary phase diagrams the Al-Ti-Fe system is relatively well established. The recent work of Mazdiyasni, Miracle, Dimiduk, Mendiratta and Subramanian [18] confirm the prior investigations by Seibold [6]. Figure 2.5 shows the Al-rich corner of the Al-Ti-Fe equilibrium diagram as isothermal sections at a) 1200 °C and b) 800 °C. The $L1_2$ single phase field seems to be restricted and shifted towards higher Fe contents at 800 °C compared to the 1200 °C isotherm.

The other ternary phase diagrams are controversial (Al-Ti-Ni and Al-Ti-Cu) or poorly established (Al-Ti-Mn) concerning the existence and the extent of the $L1_2$ phase field. For an overview see ref. [19].

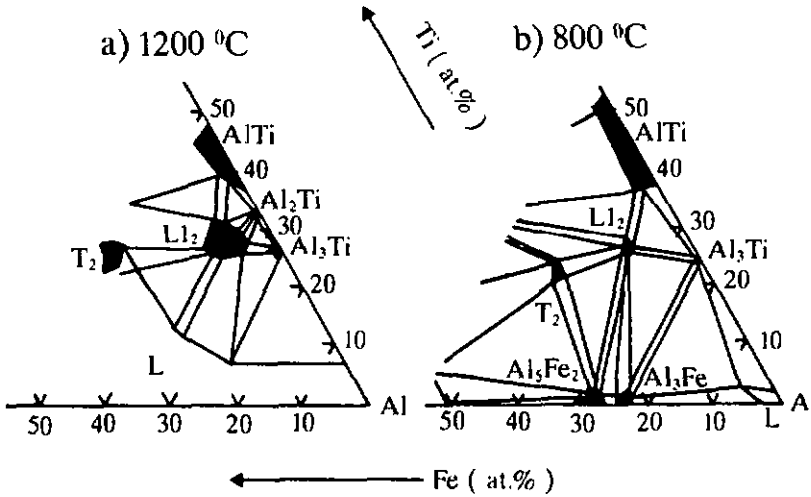

Figure 2.5: Al-rich corner of the Al-Ti-Fe equilibrium diagram, a) isotherm at 1200 °C, after [18] and b) isotherm at 800 °C after [6].

The earliest investigations on the mechanical behaviour of Al_5Ti_2M type trialuminides are published in 1988 by Kumar and Pickens, who studied an $Al_{22}Ti_8Fe_3$ compound with the $L1_2$ structure [20]. The results of compression tests are reported as 0.2 % offset yield strength in the temperature range from -196 °C up to 750 °C. The yield stress is almost constant at about 400 MPa between the temperature of liquid nitrogen and 200 °C, increases then and exhibits a peak of 475 MPa at about 400 °C. At 750 °C, the yield stress drops towards 300 MPa. Neither ductility data are presented nor is the positive temperature dependence of the yield strength commented.

Later publications report low ductility in bend and tensile tests for Al_5Ti_2M type alloys, for an overview see ref. [21]. The most widely accepted explanation for this lack of ability for plastic deformation in these materials are theories comparing the strength or energy of atomic bonds to the critical shear stress to drive a dislocation trough the crystal. In other words, the energy for propagation of a crack is compared to the energy absorbed by the crystal by emitting dislocations from the crack tip. In a material which exhibits a low resistance against crack propagation, the crack tip remains sharp, i.e. no blunting of the crack tip on a atomic level occurs. In a paper presented by Rice and Thomson [22], the authors relate crack tip blunting to the emission of dislocations from the crack tip. They find a strong tendency for crystals to be

either completely ductile, or completely brittle, so far as dislocation emission in concerned. If the condition $\mu b/\gamma_s > 7.5 - 10$ is satisfied (where μ is the shear modulus, b the Burgers vector and γ_s the true surface energy of the crack plane), the crack is expected to remain sharp, i.e. the crystal behaves in a brittle manner and fails by cleavage. Turner, Powers and Wert deduce a value for the surface energy of the crack plane in $Al_{67}Ti_{25}Ni_8$ and estimate $\gamma_s \approx 2.4$ Jm^{-2} [23]. Knowing that this rough estimation scales with the melting temperature, this value is valid for any trialuminide. Using the Burgers vector $b = a\langle 011\rangle = 0.56$ nm and $\mu = 80$ GPa [23] for Al_5Ti_2Fe, the Rice-Thomson ratio is calculated as $\mu b/\gamma_s \approx 19$. (A single $^a/_2\langle 011\rangle$ partial dislocation cannot slip away from the crack tip.) Hence, Al_3X based intermetallics are expected to have poor fracture toughness and failure will occur by cleavage.

Using selected area electron channeling pattern, George and his co-workers show that there is not an exclusive type of cleavage planes [24, 25]. Investigating different $L1_2$ trialuminides, they observe that the cleavage plane occuring most frequently is of the {110} type. For example, of the eight cleavage facets examined in an $Al_{66}Ti_{23}Fe_6V_5$ alloy, six are of the {110} type and two are of the {100} type. This finding is compared to the results of computer simulations for Al_3Sc and Al_3Ti accomplished by Fu [26]. For the Al_3Sc, exhibiting the $L1_2$ crystal structure, the cleavage strength is found to be about 19 GPa and essentially independent of the crystallographic plane. This is significantly less than the value reported for Ni_3Al, where the cleavage strength of (110) planes is estimated as about 27 GPa [25]. It is concluded that the availability of more than one plane with low cleavage strength contributes to the brittleness of Al_3Ti-based intermetallic compounds. At the same time, fracture toughness measurements are made using 4-point bend testing [25]. For the quarternary Fe and V modified alloy mentioned above, the fracture toughness is reported as $K_{Ic} = 2.1$ $MNm^{-1.5}$. The final conclusion in all three papers [24, 25, 26] is that the brittleness of trialuminides is related to their intrinsically low cleavage strength.

2.2 Temperature Dependent Strengthening Mechanisms

2.2.1 Introduction

The following section provides an overview of the models proposed in the literature of three dislocation pinning mechanisms at intermediate temperatures. Since a complete list of strengthening mechanisms would exceed the frame of the present thesis, only the models of those relevant to the actual investigations will be presented. The subjects are treated in the order of the strengthening they can offer: Strain ageing stands at the beginning, followed by antiphase boundary relaxation and cube cross-slip leading to the so called anomalous strengthening.

2.2.2 Strain Ageing

Dynamic strain ageing (DSA) is a phenomenon manifest as Lüders' bands or Portevin-LeChâtelier effect in many common interstitial and substitutional alloys. DSA is characterized by an inhomogeneous flow stress often called serrated or jerky flow, and is caused by segregation of solute atoms to dislocations. Two principally different models are proposed.

1) Cottrell postulates an "atmosphere" of solutes around the dislocations to explain strain ageing [27]. The locally higher concentration of solute atoms pins the dislocations and gives rise to a moderate hardening which can be understood as the difference in the shear stress to move a dislocation through the atmosphere or through the lattice far away from the solute cloud. At a certain temperature solute diffusion becomes rapid enough to be dragged along with the moving dislocation. The speed of the dislocation is then restricted to the speed of migration of the solute atoms in the atmosphere. Serrated flow is due to the dislocations alternately enabled to break away from their atmospheres and being caught again by the diffusing atoms.

2) Based on the fact that the motion of a dislocation is in general a discontinuous process, van den Beukel develops another theory of dynamic strain ageing [28]. He considers a dislocation segment waiting for the time t_w in front of an obstacle. At a certain stress, this obstacle is overcome and the dislocation jumps at a high velocity to the next obstacle. At a temperature high enough, segregation of solute atoms to the dislocation may occur during waiting time t_w. Thus, the dislocation stopped by an obstacle is additionally pinned by the locally higher solute concentration, leading to a moderately higher flow stress. If the dislocation surmounts the obstacle it leaves behind the solute atmosphere. More sophisticated theories, based on the van den Beukel model, explain successfully the beginning and the end of the serrated flow in many alloys [29].

It would be interesting to correlate the Portevin-LeChâtelier effect to the diffusivity of the solute atoms. Taking the van den Beukel model, the waiting time t_w can be imitated by static strain ageing tests with ageing time t_a. A normal tensile or compression test is interrupted and the sample held under stress. Essentially, the dislocations do not move during ageing under stress and the ageing time corresponds reasonably well to the waiting time. For an easy measurement of t_a, the tests have to be done at temperatures below the onset of serrated flow, where diffusion is slow.

A mobile dislocation is stopped temporary for the ageing time t_a. After Friedel [30], the concentration c of impurity atoms around a dislocation follows a power law during ageing:

$$c \sim (Dt_a)^{\beta} \tag{2.1}$$

where D is the diffusivity and $\beta = {}^1/_2$ or $\beta = {}^2/_3$, depending if the matrix impurity interaction is due to modulus or size effects respectively.

Fleischer [31] and Labusch [32] in their theories of solution hardening found a dependence of the critical shear stress τ_c on the solute concentration as follows:

$$\tau_c \sim c^{\beta} \tag{2.2}$$

Again, $\beta = {}^1/_2$ (Fleischer) or $\beta = {}^2/_3$ (Labusch). For polycrystals, the flow stress is proportional to the critical shear stress, such that an increase in stress $\Delta\sigma$ can be expressed as

$$\Delta\sigma \sim (Dt_a)^n \tag{2.3}$$

Where n is a number in the range of ${}^1/_4$ to ${}^4/_9$. With the temperature dependence of D:

$$D \sim \exp\left(\frac{-Q_{SA}}{RT}\right) \tag{2.4}$$

where R is the molar gas constant and Q_{SA} the activation energy of strain ageing, (2.3) becomes

$$\Delta\sigma = A(t_a)^n \exp\left(\frac{-Q_{SA}}{RT}\right)^n$$

or $$\ln(\Delta\sigma) = \ln(A) + n\ln(t_a) - \frac{n Q_{SA}}{RT}$$

where A is a constant. For a given ageing time t_a, the first two terms on the right hand of this equation are constant and the equation reduces to:

$$\ln(\Delta\sigma) = \kappa - \frac{n Q_{SA}}{RT} \tag{2.5}$$

where κ is another constant including t_a. With the well known Arrhenius type plot $\ln(\Delta\sigma)$ vs T^{-1}, Q_{SA} can be calculated as:

$$Q_{SA} = \frac{m_{Arr} R}{n} \tag{2.6}$$

Where m_{Arr} is the slope of the curve in the Arrhenius plot. Using equation (2.3) and taking the natural logarithm, n can be determined as the slope of the line in the plot $\ln(\Delta\sigma)$ vs $\ln(t_a)$:

$$\ln(\Delta\sigma) \sim n\ln(D) + n\ln(t_a)$$

Comprehensively, a $\Delta\sigma$ vs t_a or $\ln(\Delta\sigma)$ vs $\ln(t_a)$ plot is used to determine $\Delta\sigma_f$ at a fixed ageing time. The slope n in the logarithmic $\ln(\Delta\sigma)$ vs $\ln(t_a)$ graph together with the slope of the Arrhenius plot $\ln(\Delta\sigma_f)$ vs T^{-1} enter into eq. 2.6 in order to calculate the activation energy of strain ageing, Q_{SA}.

2.2.3 Antiphase Boundary Relaxation

If a superdislocation, as mentioned in section 2.2, moves, it trails an APB enclosed by the superpartials through the lattice. This fault produced by shear is a sharp discontinuity in the stacking sequence of the ordered crystal. Annealing such a fault will lead to a spread of the discontinuity over several atom layers. This phenomenon is known as APB relaxation. It can be understood in terms of increasing the low configurational entropy corresponding to the sharp, shear-produced discontinuity. In addition, excess atoms in the material, if the composition is not exactly on stoichiometry, will tend to diffuse to the boundary, reducing the overall energy level of the alloy and changing the local composition significantly.

Considering β brass with bcc ordered crystal structure, Brown [33] is the first to establish a relationship between APB relaxation and the yield point of a superlattice. More precisely, he associates the critical shear stress τ_c to the fault energy γ of the APB enclosed by a superdislocation, and finds the dependence

$$\tau_c = \frac{\gamma}{2b} \tag{2.7}$$

where b is the Burgers vector. Brown continues the calculations taking into account only nearest neighbour interactions and neglecting diffusion. Finally, τ_c is related to the long-range order by the relationship

$$\tau_c \sim S^2 \tag{2.8}$$

where S is the degree of long-range order. The assumptions made by Brown [33] restrict the validity of eq. 2.8 to the temperature range of $0.5T_c < T < T_c$, where T_c is the critical temperature of the order-disorder transition. Figure 2.6 shows the long-range order as a function of the distance perpendicular to the plane of the stacking fault.

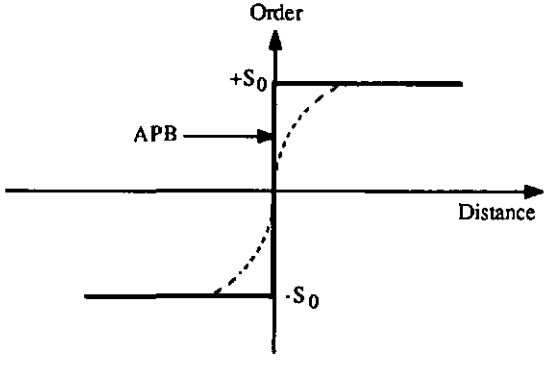

Figure 2.6 Long range order vs distance from the slip interface. The full line is the APB created by slip of a single dislocation. The dotted line shows the APB spread to its thermal equilibrium width $\bar{d}$. (After Brown [33])

β brass undergoes an order-disorder transformation at a critical temperature of about 460°C. Increasing the temperature closer to T_c means that entropy effects reduce both the overall degree of order and, particularly, that at the fault. The width d of disordered material at the fault increases gradually. The reduction of order and stacking fault energy at the APB plane of a superdislocation will lead to pinning of that dislocation. Including APB relaxation, the motion

of a superdislocation involves the leading partial dislocation creating a fresh, high energy APB, whilst the trailing partial will only incompletely reheal the low energy, relaxed APB. From the calculations of Brown, a maximum extent of dislocation pinning is predicted at a temperature of about 0.7 T_c. This is in reasonable agreement with high temperature strength measurements.

One of the shortcomings of Browns theory is that it disregards the segregation of solutes to the stacking fault, known as Suzuki effect in normal fcc solid solutions. The idea of chemical segregation to the APB is followed by Popov and his coworkers [34, 35], who investigate the $L1_2$ crystal structure. Calculations made by this group consider both relaxation of the long-range order and segregation of one of the components to the APB. It is deduced that the combination of both mechanisms leads to a significant reduction in the order parameter S. In the range between 0.5 T_c and T_c, S falls much faster at the APB than in the bulk material. The APB thickness, hence, increases by several atom layers. Segregation occurs at the APB, leading to an enrichment in element A at the fault plane for an exactly stoichiometric A_3B alloy. In case of a composition richer in A or B atoms, a segregation of the excess atoms at the fault is observed. All these changes lead to significant pinning of the superdislocations.

The models presented here can only explain the temperature dependence of the yield stress. But a rapid relaxation at elevated temperature can produce continuous, steady-state relaxation and, hence, maintain superdislocation pinning. Similar to Cottrell locking in annealed materials, APB relaxation can lead to dislocation locking and to the appearance of discontinuous yield points as well as dynamic strain ageing (DSA), if relaxation occurs fast enough. On several occasions, discontinuous yielding or DSA has been observed and related to APB relaxation, e.g. as reported by Morris, Besag and Smallman for Cu_3Au [36, 37]. In this work, Morris shows that APB relaxation can lead to dynamical strengthening throughout plastic deformation, although the model proposed can not explain the phenomenon in all details.

Schoeck and Korner investigate the evolution of the dissociation distance of superdislocations in plastically deformed Ni_3Fe during in situ heating [38]. They observe that the separation d between the superpartials enclosing an APB increases because the geometrical APB formed by slip can lower its energy by reordering of atoms in its neighbourhood. The value of the equilibrium APB energy $\bar{\gamma}$ is reached asymptotically. The increase of d during in situ annealing in the temperature range of 0.89 T_c < T < 0.98 T_c is slow enough to establish evolution kinetics (where T_c is the temperature of the order-disorder transition). Three models are proposed:

Model A: The APB is considered as a thermodynamic system with initial free energy γ_0 of the APB created by slip. With the assumption that the APB energy γ approaches the equilibrium $\bar{\gamma}(T)$ at a rate which is proportional to the deviation from equilibrium (the classical second order relaxation model), it is deduced

$$\frac{d\gamma}{dt} = -\frac{\gamma - \bar{\gamma}}{k_A} \qquad (2.9)$$

where k_A is a constant, the so called relaxation time, determined by the diffusion process.

Model B: The APB is considered as enclosed by two unit dislocations. This system of the two dislocations and the APB ribbon has the free energy E and approaches the equilibrium energy $\bar{E}$ according to the linear rate equation

$$\frac{dE}{dt} = -\frac{E - \bar{E}}{k_B} \qquad (2.10)$$

where k_B is another relaxation time.

Model C: As starting-point, the authors consider a geometrical APB freshly created by slip with an energy γ_0. For beginning the relaxation, it is assumed that the displacement of the partial dislocations in x direction can only take place if the APB energy, starting from γ_0, is simultaneously reduced by atomic rearrangement to a value γ_e. The dislocation will undergo a diffusion-controlled movement and the resulting rate described by an Einstein drift is given by

$$\frac{dx}{dt} = k_C \left(\frac{2E_\tau}{x(t)} - \gamma_e \right) \qquad (2.11)$$

where E_τ is the pre-logarithmic energy factor of the superpartials which determines their mutual repulsion and k_C is a rate constant.

Schoeck and Korner find that model C offers the best description for the observed kinetics of APB relaxation in Ni_3Fe.

2.2.4 Cube Cross-Slip

In a work published 1962, Kear and Wilsdorf [39] investigate the dislocation structure in Cu_3Au, exhibiting the ordered $L1_2$ structure. They find a homogeneous distribution of dislocations, but also unusually long and straight dislocation segments. The later are interpreted in terms of cross-slip of screw dislocations from their octahedral (111) slip planes onto (010) cube planes (see figure 2.7). The driving force for this cross-slip is the reduction of the energy of the superdislocation. The difference in APB energy between an APB on (111) and on (010) is evident when looking at the fault created by a moving $<10\bar{1}>$ superdislocation. On (111), the APB due to the leading partial $^a/_2<10\bar{1}>$ changes NN bonds, contrary to the same partial on (010) which creates an APB with only "wrong" second nearest neighbours.

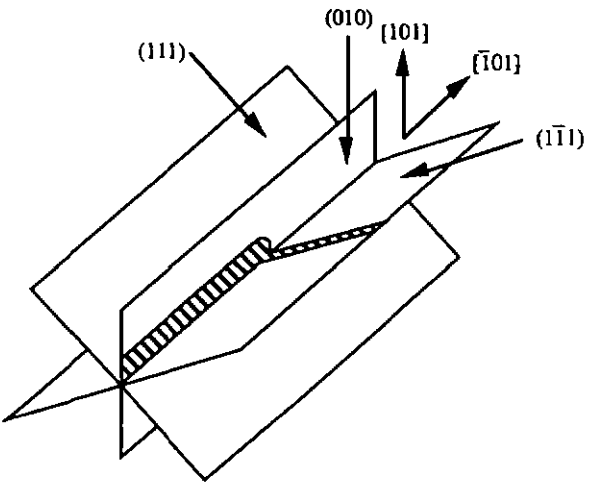

Figure 2.7 Schematic representation of a straight dislocation segment locked by cross-slip of a superdislocation in screw orientation from their usual $(1\bar{1}1)$ slip plane onto a (010) plane. (After Kear and Wilsdorf [39], the actual understanding of the cube cross-slip process is shown in figure 2.10.)

Due to this cross-slip, the superdislocation becomes relatively immobile, in accordance with the experimentally observed straight dislocation segments. Further, certain of these straight segments are connected to one another in a stepwise manner. This observation is consistent with a model of cross-slip occuring at different positions on an expanding dislocation loop. It is proposed that cross-slip plays an important role in work hardening of ordered $L1_2$ alloys. At low strains, accidental cross-slip of dislocations in the screw orientation will tend to control the average slip distance, and therefore the work hardening. At higher strains, where more than one

system becomes active, obstacles to slip may develop as a result of the Lomer dislocation reaction, which provides an additional source of hardening.

Thornton, Davies and Johnston [40] study, in 1970, the ordered phase Ni_3Al deformed in compression as well as in creep. Ni_3Al exhibits the cubic $L1_2$ crystal structure. The authors report among other observations the positive temperature dependence of the microstrain yield stress and the flow stress, the strain rate sensitivity of the flow stress and structural investigations, namely slip trace analysis and TEM observations of the dislocation structure. According to the form of the response of the flow stress to strain rate changes two zones of different modes of response are defined, with a transition occuring at about 400 °C. Below this transition temperature the activation volume is small, 25 to 300 b^3 (where b = 0.508 nm). Appreciable strain rate sensitivity was found only at temperatures above 600 °C. Deformation in zone I ($T \leq 400$°C) is carried by edge dislocations, moving on {111}. Screw dislocation appear to remain in sessile configuration, visible in TEM as long straight segments, as described by Kear and Wilsdorf [39]. In zone II ($T > 400$ °C) plastic deformation involves glide of edge and screw dislocations, mobile both on {111} and {100} planes. Moving dislocations are submitted to an increasing interaction with forest dislocations and dislocation loop debris coming from the additionally activated cube slip planes at higher temperatures. In summary, Thornton and his coworkers attribute the increase in the flow stress with increasing temperature observed in Ni_3Al to a change in the mechanism controlling the flow stress. An exhaustion hardening process at low temperatures is supplanted by a debris hardening process at higher temperatures. This transition arises from an increased propensity for {100} slip.

In 1973, Takeuchi and Kuramoto publish an investigation on another $L1_2$ material showing the anomalous strengthening, namely Ni_3Ga [41]. They report the temperature dependence of the yield stress as well as slip pattern and TEM observations of the dislocation structure. The yield stress-temperature curve is divided into three stages, i.e. the low temperature (-196 °C) stage (I), the intermediate temperature (RT to about 600 °C) stage (II), and the high temperature (above 600 °C) stage (III). The yield stress in stage I is considered to be determined by solid solution hardening due to the deviation from the stoichiometry and to impurities. In stage II, the yield stress is regarded as the superposition of this solution hardening effect and an anomalous temperature effect. The beginning of stage III is related to the onset of the macroscopic slip on {100}. From the character of the dislocations observed in deformed crystals, the flow stress in stage II is determined by the mobility of the screw dislocations. Furthermore, the critical shear stress for {111}<110> slip increases with increasing stress component on the {100} plane. This suggests that cross-slip of screw dislocations onto the cube plane is reasonable for the anomalous temperature effect. Based on this orientation dependence of the critical shear stress and the results of electron microscopy, the positive influence of the temperature on critical shear stress is interpreted in terms of a model in which the marcoscopic yield stress is determined by

the dynamic motion of screw dislocations. Dynamic motion means creating and breaking away sessile dislocation segments. These sessile segments are formed by thermally activated cross-slip of a short portion of the superdislocation onto the {100} plane to reduce the total energy of the dislocation. Nevertheless, the superdislocation will continue to slip on {111} because its mobility on {111} is much higher than on {100}. When the stress is increased to a sufficiently high level, the drift velocity of the dislocation moving through an array of obstacles comes to be substantially the same as the free flight velocity at this stress level. This phenomenon is known as the dynamical break-away process. The dislocation bends locally only around the sessile points and passes through them almost in a straight form. One new sessile portion is formed on the average after the time t, in which the dislocation proceeds to the critical distance. The dynamical motion of a screw dislocation is schematically illustrated in figure 2.8.

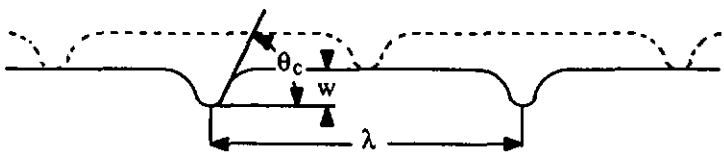

Figure 2.8 Schematic illustration showing the dynamical motion of a dislocation creating and breaking away sessile portions. (After Takeuchi and Kuramoto [41])

In two articles published in 1982, Yamaguchi, Paidar, Pope and Vitek [42], and Paidar, Yamaguchi, Pope and Vitek [43] respectively, report computer simulations of the core structure of a <110> screw dislocation in a general ordered alloy with the $L1_2$ structure. Dislocations lying on both {111} and {100} planes in stress-free crystals, on one hand, and under an applied stress, on the other hand, are studied using different interatomic potentials corresponding to different anti-phase boundary (APB) and complex stacking fault (CSF) energies on {111} planes. The results of the simulations indicate that, if the APB energy is not too high, the dislocations dissociate on the octahedral plane in to two $^1/_2$<110> superpartials separated by an APB (cf. figure 2.9a). The cores of the superpartials are coplanar with the APB and can be considered as two Shockley partials $^1/_6$<112> limiting an CSF on {111} (see figure 2.9b). This configuration is glissile with a low Peierls' stress. If the APB energy is high, the dislocation dissociates on {111} in two $^1/_3$<112> superpartials separated by a superlattice intrinsic stacking fault (SISF), the cores of which are highly non-planar. The Peierls' stress to move this three dimensional, but glissile dislocation configuration is relatively high. On {100} planes the dislocation always dissociates into two $^1/_2$<110> superpartials. The cores of these partials are not coplanar with the APB and spread on (111) or ($1\bar{1}1$) or two types of of these octahedral planes simultaneously. Once in this sessile configuration, further motion on {100} can only take place with the help of thermal activation.

The authors interpret these calculated results by suggesting two classes of $L1_2$ ordered alloys which show different dependences of the flow stress on temperature. Compounds in which dislocations dissociate on {111} planes into $^1/_2$<110> superpartials separated by APB show a weak dependence of the flow stress on temperature at low temperatures, but are likely to exhibit a strong increase of the flow stress at high temperatures (anomalous strengthening). When dissociation on [111] planes into $^1/_3$<112> superpartials separated by SISF occurs, the flow stress will increase rapidly with decreasing temperature, while the increase at high temperatures is likely to be weaker than in the former case. The energies of the APB and SISF can be estimated in terms of the stability of the $L1_2$ structure relative to related crystal structures. If a change in composition tends to make the $L1_2$ alloy unstable relative to DO_{22}, the APB separation is more probable. In the case of instability relative to DO_{19} (a hexagonal-based structure), dislocation splitting with superpartials separated by SISF is more likely. Figure 2.9 depicts schematically the two classes of superdislocations proposed for the $L1_2$ crystal structure.

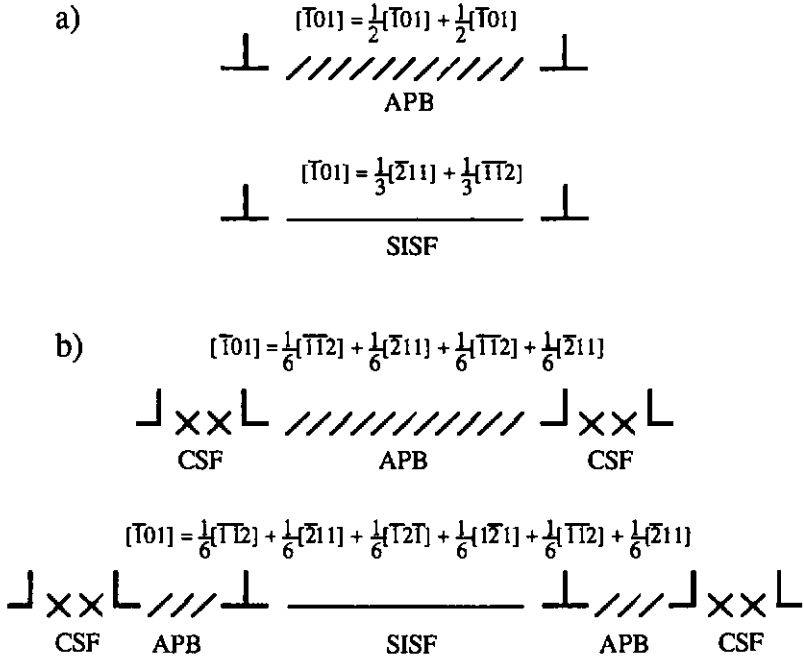

Figure 2.9: Two possible superdislocation configurations for the $L1_2$ crystal structure. The reaction schemes and graphical illustrations are shown. a) without further dissociation of the superpartials, b) superpartials dissociated into Shockley partials.(After Pope and Ezz [44])

In their publication in 1984, Paidar, Pope and Vitek [45] propose a model which predicts the form of the activation enthalpy of cross-slip from (111) to (010). Based on the results of Takeuchi and Kuramoto [20], their model incorporates the constriction theory for cross-slip and the computer simulations of superdislocations in a general $L1_2$ alloy accomplished by Yamaguchi et al. [42] and Paidar et al. [43]. The Paidar-Pope-Vitek (PPV) model successfully predicts the temperature and orientation dependence of the macroscopic yield stress as well as the tension / compression asymmetry of the critical shear stress. The anomaly of the shear stress behaviour as function of temperature is related to the dissociation and the core structure of the superdislocations. The sequence of cross-slip is described as nucleation of a constriction of the two Shockleys on the leading partial, $^1/_2[\bar{1}01]$, of a screw superdislocation on the (111) plane. The cross-slip initiates at this constriction, the dislocation translates a distance w along the (010) plane and the cross-slipped segment immediately dissociates on the $(1\bar{1}1)$ or (111) plane. The driving force of such a process is the difference in APB energy on (111) and (010) respectively. The PPV model requires an APB anisotropy of $\gamma_{111} / \gamma_{010} > \sqrt{3}$ for cross-slip onto (010) where γ_{111} and γ_{010} are the APB energy on (111) and (010), respectively. The atomistic studies by Yamaguchi et al. [42] and Paidar et al. [43] indicate that the core of a $^1/_2[\bar{1}01]$ superpartial is always dissociated on the {111} planes. Hence, the leading superpartial will move on (010) a distance w of $^b/_2$ or b only before redissociating immediately on an octahedral plane. Since w is very small, the authors consider the cross-slip process as a core transformation. In this double kink configuration, the screw superdislocation is dissociated in a non-planar and sessile form. The thermally activated formation of a double kink and the rearrangement of the core of the superpartial are proposed as the dynamic processes of cross-slip. The frequency of these dislocation locking events increases with increasing temperature and explains the anomalous temperature dependence of a $L1_2$ material, the deformation of which is controlled by superdislocations separated by an APB. Figure 2.10 illustrates the cross-slipped configuration of a $(111)[\bar{1}01]$ superdislocation.

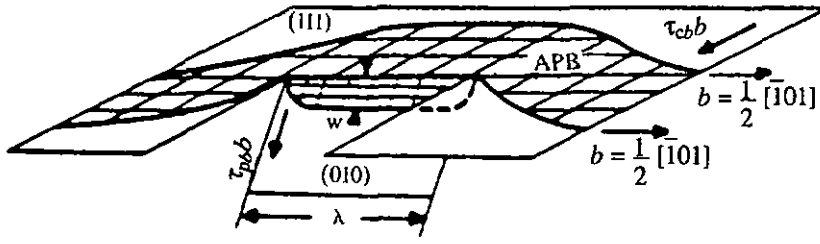

Figure 2.10: A perspective view of the cross-slip of one superpartial from the (111) to the (010) plane. For simplicity, the redissociation of the $^1/_2[\bar{1}01]$ core on {111} is not shown. (After Paidar, Pope and Vitek [45])

2.3 Identification of Deformation Mechanisms

2.3.1 Introduction

Macroscopic deformation experiments are generally insufficient to identify the microscopic deformation mechanisms. Such tests have to be correlated to other experiments (e.g. diffusion measurements) and indirect observations (e.g. slip trace analysis) or direct observations (e.g. TEM analysis) of mobile dislocations. While classical electron microscopy is restricted to the state of the material after deformation, macroscopic deformation experiments give indications of the dynamic dislocation interactions which occur during deformation. In case of thermal activation, the results of macroscopic tests allow to limit the number of possible mechanisms controlling deformation.

It must be kept in mind that the model of the activation volume considers one dislocation and its interaction with a restricted number of obstacles. In real crystals, other mechanisms may play a role. For example, interactions between dislocations, the formation of slip bands, grains boundaries or segregation influence the motion of dislocations. Nevertheless, the experience show that the measurement of the activation volume offers additional information on the deformation of materials. On the base of TEM observations it must be verified that the model of the activation volume applies to the observed dislocations.

2.3.2 Activation Volume

Cagnon [46] considers the geometrical meaning of the activation volume, V, and relates it to the thermodynamic definition. In geometrical terms, the activation volume equals the activation area, A, multiplied by the Burgers vector b, $V = b \cdot A$. The activation area can be considered as the surface a dislocation crosses while it "feels" the interaction with an impediment. As an example, a dislocation meeting localized obstacles on its slip plane is illustrated in figure 2.11. A dislocation moving in the direction of the x-axis is pinned in front of the obstacle row A-B-C and surmounts B in a next step. At x_0 the dislocation is in an equilibrium position, at x_c in an unstable position with an energy equal to the equilibrium value and at x_f in the equilibrium position behind the obstacle. A is the area between the two lines representing the dislocation at x_0 and bowed out at position x_c, respectively.

The thermodynamic definition of the activation volume V is given by the relationship:

$$V = -\left(\frac{\delta \Delta G}{\delta \sigma}\right)_T \qquad (2.12)$$

where ΔG is the Gibbs' free energy. For the situation in figure 2.11, this relationship can be expressed as

$$U = \int_{x_0}^{x_c} \frac{\delta F}{\delta \sigma} dx = \lambda x b \tag{2.13}$$

where F is the force acting on the dislocation, λ the average spacing of the obstacles and x ($= x_c - x_0$) the "active" size of the obstacle. It is seen that the product λx corresponds to the activation area. This simple model does not take into account that under a high shear stress the dislocation bows out between the anchoring points. With increasing τ the curvature increases and the dislocation line touches more obstacles, λ decreases. This problem can be overcome by measuring λ along the dislocation line.

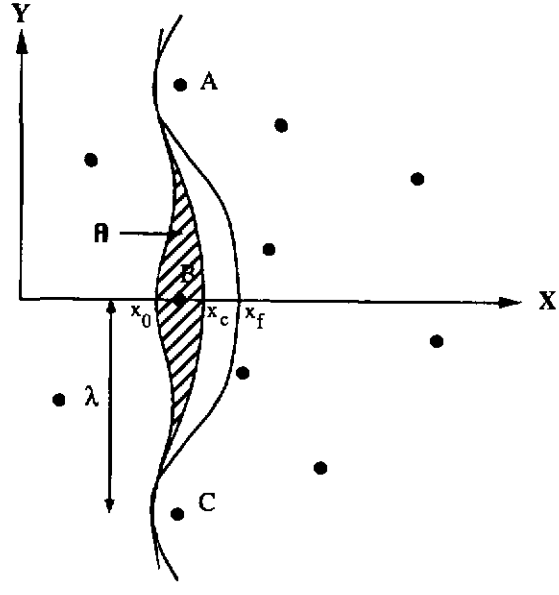

Figure 2.11: Schematic representation of the activation area **A**. A, B and C are localized obstacles lying in the slip plane of a dislocation with a spacing λ each. x_0 and x_f are the equilibrium positions in front and behind obstacle B, respectively. x_c is the unstable position at equilibrium energy directly after surmounting B.

The definition of U can also be used in the context of macroscopic deformation experiments. Considering the general equation for thermally activated deformation

$$\dot{\varepsilon} = \dot{\varepsilon}_0 \exp\left(\frac{-\Delta G}{kT}\right) \tag{2.14}$$

where $\dot{\varepsilon}$ is the strain rate, $\dot{\varepsilon}_0$ is assumed to be constant in the present framework, k is the Boltzmann constant and using eq. 2.12, the following expression is deduced:

$$U = kT\left(\frac{\delta(\ln\dot{\varepsilon})}{\delta\sigma}\right)_T \tag{2.15}$$

Hence, the activation volume is a measure of the strain rate sensitivity and can be determined by recording the flow stress at different strain rates.

Analogous to eq. 2.13 a formula for linear obstacles can be deduced:

$$U = bd\lambda_c \tag{2.16}$$

where d is the (dissociation) width of the dislocation and λ_c the critical length of the pinning segment.

Groh [47] presents a list of possible mechanisms related to dislocation slip, see table 2.1.

	obstacles acting on a dislocation segment	local obstacles in the lattice
thermal activation	• lattice friction (Peierls) • Shockley cross-slip • dissociation/recombination	• dislocation forest • solution hardening
thermal activation or athermal	• Suzuki or Cottrell atmospheres • local changes in order (APB relaxation)	• coherent precipitations • irradiation defects
athermal	• changes in long range order	• incoherent precipitations • trailing kinks • long range residual stresses

Table 2.1: Examples of mechanisms influencing dislocation movement, after Groh [47].

He classifies them, on the one hand, as thermally activated or athermal and, on the other hand, as local obstacles in the lattice or impediments along a dislocation segment *. While for athermal deformation eq. 2.14 is not valid and, consequently, **U** is not defined, the activation volume related to the other dislocation obstacles are discussed in the following:

Peierls' lattice friction: the dislocation moves by forming a kink, one b in width, d, and several b in length λ_c. Thus. eq. 2.16 becomes

$$\mathbf{U}(\text{Peierls}) = b^2\lambda_c \qquad (\text{with } 3b \le \lambda_c \le 10b) \quad (2.17)$$

This mechanism is independent of the specific material but λ_c is temperature dependent. The upper limit mentioned applies only at 0 K. Groh gives an upper limit for λ_c at temperatures in the order of magnitude of 0.1 T_m with $\lambda_c \le 100\, b^3$ [47]. The thermal fluctuations increase the critical lenth of the double kink of width b in the classical Peierls' model.

Shockley cross-slip: the Shockley partials constrict and bow out on the cross-slip plane. The width of the dissociated dislocation is d and the critical length of the constricted segment is $\lambda_c \approx 5d$. Using eq. 2.16 yields

$$\mathbf{U}(\text{Shockley}) = 5d^2b \qquad (2.18)$$

The superdislocation reaction schemes introduced in section 2.3.4, figure 2.8, leave open the possibility of further dissociation of the superpartials into Shockley partials. Assuming that the latter exist, a critical value of **U** can be related to the resolution in TEM. Imaged under g : 4 - 5 g contrast condition in weak beam, a dissociation $d \le 2.5$ nm is not resolved. Taking eq. 2.18 with $d = 2.5$ nm and $b = 0.28$ nm (cf. section 2.1), the activation volume is estimated as $\mathbf{U} \approx 400\, b^3$. In other words, if the Shockley partials are not observed in weak beam examinations and the measured activation volume is $\mathbf{U} \le 400\, b^3$ cross-slip cannot be excluded as deformation controlling mechanism.

Dislocation dissociation and recombination: A dislocation dissociated by the distance d recombines over a critical length λ_c. As a rule of thumb, Groh [47] assumes that an undissociated segment longer than 50 b is sufficiently stable to act as an anchoring point. Eq. 2.16 gives

---

* : The original french publication classifies in "obstacles linéaires" and "obstacles localisés". The interpreting translation takes into account the actual understanding of dislocation slip.

$$U(\text{dissociation}) \geq 50db^2 \qquad (2.19)$$

Similar to the constriction of the Shockley partials for cross-slip, dissociation and recombination of dislocations can happen in a hidden manner, i.e. below the resolution of TEM. Assuming again d = 2.5 nm and b = 0.28 nm, eq. 2.19 yields $U \approx 4000\, b^3$. If dissociatied and undissociated segments on the same dislocation are observed by weak beam technique, the measured activation volume must be $U \geq 4000\, b^3$ to have dissociation and recombination as the mechanism dominating the deformation. Such high activation volumes cannot be determined by changes in strain rate since the response of the flow stress becomes undetectably small.

Dislocation forest: A moving dislocation is pinned by forest dislocations in an average distance of λ. Comparing with eq. 2.13, $x \approx b$ and λ can be expressed in terms of the density of forest dislocations ρ_f, i.e. $\lambda = \rho_f^{-0.5}$, thus follows

$$U(\text{forest}) = b^3\rho_f^{-0.5} \qquad (2.20)$$

Considering eq. 2.20, it is seen that an increase of the density of forest dislocation by a factor of 100 only gives rise to a drop in U by a factor of 10. Only a drastic decrease of U with increasing strain indicates forest dislocation as the controlling deformation mechanism. The increase of the activation area with increasing strain is much smaller (cf. page 23) and masked by the effect of the dependence of U on ε.

Solution hardening: The dislocation is pinned by solute atoms, as illustrated in figure 2.11. The lattice distortion around such an obstacle is assumed to be a few b, i.e. $b \leq x \leq 5b$. For a random solution, the average distance between the solutes is $\lambda = c_s^{-0.5}$, where c_s is the concentration of the solute atoms per surface unit. Taking the surface unit as $b^2\,\lambda = bc^{-0.5}$, where c is the normal molar concentration, eq. 2.13 yields

$$U(\text{solute}) = xb^3c^{-0.5} \qquad (\text{with } b \leq x \leq 5b) \qquad (2.21)$$

The activation volume depends only on the solute concentration and is independent of the specific matrix material. This model applies strictely only in a crystal at absolute zero. Comparison of the analyzed solute concentrations with the activation volume should be done using U at 0 K. For strong interaction of the dislocation with the solutes, there is a mild dependence of the activation volume on stress.

Precipitation hardening: The obstacles in figure 2.10 are considered as particles. Assuming the extreme case of small particles ($x = 5\ b$), with a small spacing ($\lambda = 500\ b$), eq. 2.13 gives rise to

$$\mathbf{U}(\text{particle}) = 2500b^3 \tag{2.22}$$

In usual precipitation hardened alloys, $\mathbf{U}$ is expected to be even higher. Such high activation volumes cannot be determined by changes in strain rate, since the response of the flow stress becomes undetectably small. Again, the dislocation may bow out under a high shear stress and $\mathbf{U}$ depends slightly on τ.

Irradiation faults: Irradiation can lead to different lattice defects, for an overview see e.g. ref. [48]. Vacancies and interstitials can be treated as solution hardening, eq. 2.21, diluted zones and cavities act as obstacles similar to particles, eq. 2.22. However, irradition defects have no importance in the following work.

Suzuki or Cottrell atmospheres and APB relaxation: These faults evolve during the time necessary to overcome the pinning. Strain rate experiments are falsified and the deduced activation volume has poor significance. This important fact must be kept in mind for the analysis which will be presented in section 4.2.5.

At low temperatures, it is often difficult to decide based on the activation volume if lattice friction or solution hardening controls the deformation. Biget and Saada propose a procedure to eliminate the contribution of thermal activation to the activation volume by extrapolating $\mathbf{U}$ at 0 K [49]. The activation volume of lattice friction is expected to be a few b^3 at absolute zero. On investigating the deformation of pure Ti single crystals at temperature between 4 K and 296 K, the authors observe a dependence of the activation volume on stress as

$$\mathbf{U} = B(\tau - \tau_{int})^{-2} \tag{2.23}$$

where B is a constant, τ the applied shear stress and τ_{int} the internal shear stress. This relationship is treated with the framework of the theory of thermally activated glide. By determining graphically the constants B and τ_{int} at 0 K, $\mathbf{U}$ at 0 K is deduced as $\mathbf{U}_0 \approx 8\ b^3$. It is concluded that frictional stress controls the deformation at absolute zero. The authors emphasize that small amounts of substitutional impurities (< 100 ppm) have a large influence on the plastic behaviour at low temperatures.

3. Materials and Experimental

3.1. Preparation of the Materials

3.1.1 Introduction

The materials in the focus of the present work are bulk intermetallic billets, prepared by the Osprey spray deposition technique. Samples of these ternary alloyed compounds will be labelled with their chemical formula, suggesting their stoichiometry: Al_5Ti_2M (where M is Cr, Mn + Cr, Mn, Fe and Cu).

Supplementarily, casting, mechanical alloying (MA) of elemental powders and composites prepared by mixing elemental powders with intermetallic powders are investigated. MA materials will be labelled with their composition in at-%: Al - x%Ti. The composites again will be labelled only with the ingredients, for example Al_5Ti_2Fe + Fe. Figure 3.1 gives an overview of the preparation routes for the three types of materials.

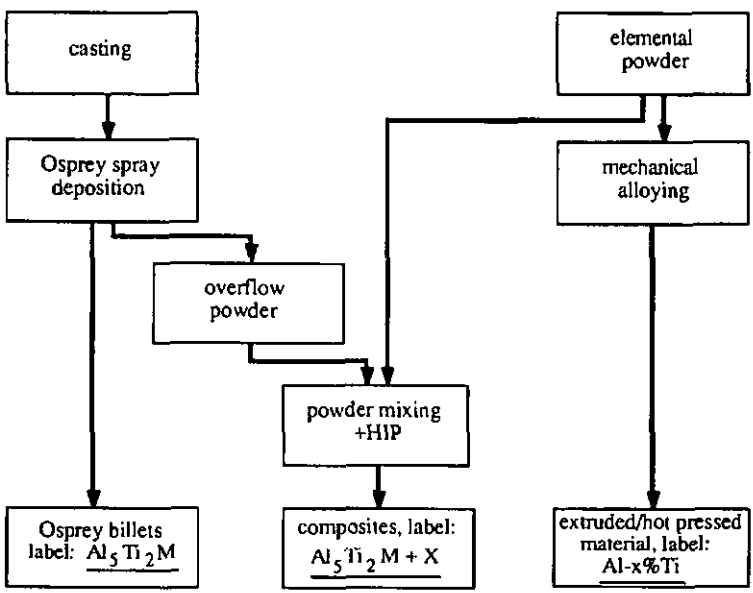

Figure 3.1 The preparation routes for the three types of materials and their labelling in the current work.

3.1.2 Casting

The melting and casting of the intermetallic phases were done at Alusuisse-Lonza Services Ltd at Neuhausen. The cast ingots were very inhomogeneous and porous. Therefore, no mechanical tests were done on samples in this state. Prealloyed ingots were subsequently used as melt stock for the spray deposition, described in 3.1.4 .

3.1.3 Mechanical Alloying

Mechanical alloying is a high energy milling process for the production of composite or alloyed metallic powders. The control of milling speed, milling time, and the use of processing control agents allow a fine microstructure to be obtained. The milling process itself consists of repeated welding and fracturing of powders in a highly activated ball charge. Under this condition of a balance of rates of welding and fracturing, an alloyed powder with fine dispersed initial constituents within the same grain is formed. Figure 3.2 shows schematically the refinement of the structure in the powder grains.

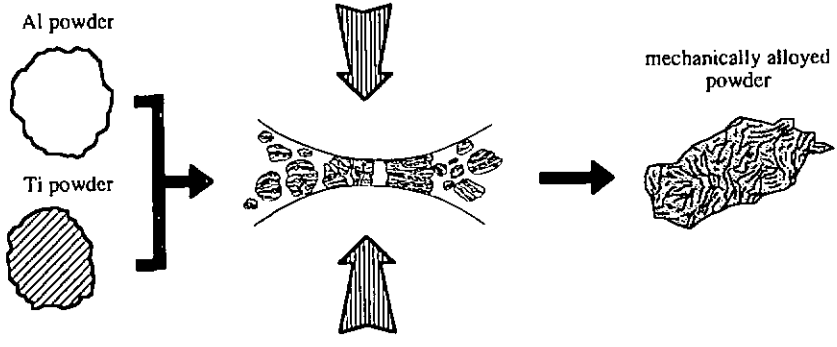

Figure 3.2 Evolution of the microstructure within the powder grains during MA.

A commercial ball mill (Fritsch Pulverisette 7) was used for the mechanical alloying of elemental aluminium and titanium. The powders of size below 150 µm were filled into hardened chrome steel containers together with the balls made of the same steel. The weight ratio of balls to powder was 8 to 1. The powders were stored under vacuum and all powder handling was done in a glove box under Ar atmosphere. During milling, the containers were sealed. An organic lubricant (2-butoxymethanol) was added to the powders as a process control agent preventing premature welding of the powder particles. The milling time was 5 h.

Following milling, the powders were cold compacted, using a pressure of about 500 MPa. The green billets were first homogenized for 1h at temperatures in the range 600 °C - 800 °C. Final consolidation was accomplished by hot pressing or extrusion.

Table 3.1 gives an overview of the chemical composition, the homogenization temperature as well as the method and temperature of consolidation.

Aluminium at-%	Titanium at-%	T(homog.) °C	T(extrusion) °C	T(hot press.) °C
87.5	12.5	600	500	-
		700	500	-
		800	400	-
80	20	800	700	-
		800	800	-
		800	820	-
		800	850	-
		800	-	500
		800	-	700
		800	-	800
		800	-	900
		800	-	1000
76	24	800	-	800
		800	-	900
		800	-	1000
75	25	800	-	700
		800	-	900
		800	-	1000
74	26	800	-	800
		800	-	900
		800	-	1000

Table 3.1: Chemical composition, homogenization and consolidation temperature

3.1.4 Osprey Spray Deposition

The Osprey spray deposition technique combines powder atomization and powder consolidation in one step. A stream of molten metal is disintegrated into a fine dispersion of droplets using high energy gas (N_2 in the current work). The resultant distribution of droplets is directed towards a substrate, where it impacts and builds up into a deposit of a shape given by the spray equipment and the process parameters. Figure 3.3 shows a schematic section of a simple plant for the production of billets by spray deposition. As indicated in this figure, the stream of droplets is not focused to the center of the substrate. The rotation of the latter ensures a regular shape of the deposit. The material is added in a spiral way, giving rise to an approximately cylindrical billet. Unfortunately, this preparation technique can enhance spray layers perpendicular to the rotational axis.

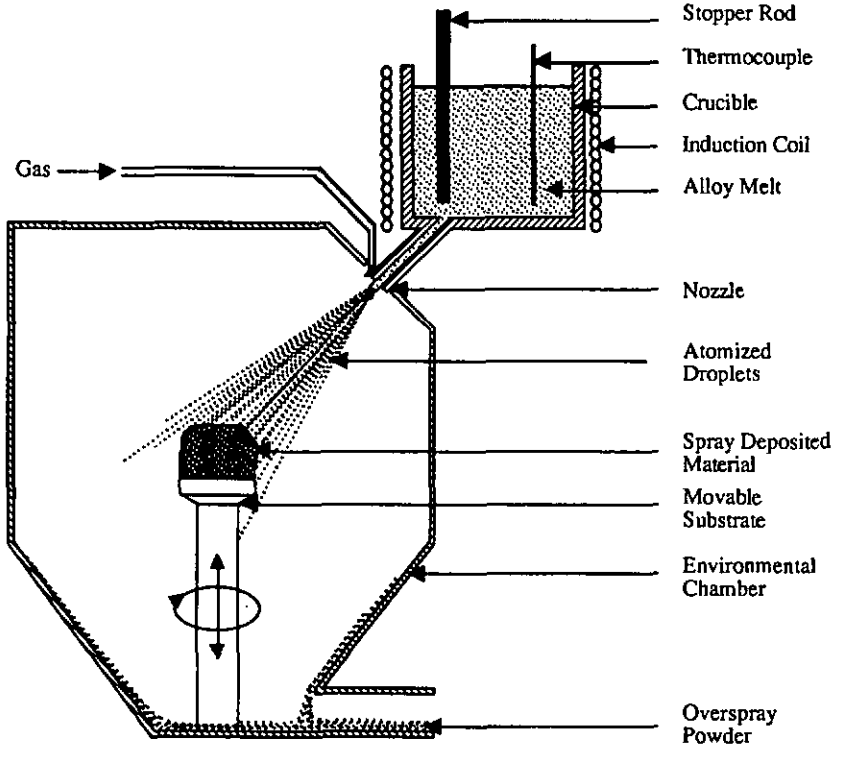

Figure 3.3 Osprey spray deposition: schematic section through a deposition chamber.

The master alloys were prepared by casting as described in 3.1.1. These ingots were remelted for spray deposition at Osprey Metals Ltd. in Neath, UK. The deposits had sizes of several kilos each. The overspray powders were collected for subsequent consolidation as described in detail in 3.1.5. While the spraying process offers a rapid solidification (several 10^3 °C/sec cooling rate), the deposited billets had to be cooled slowly and uniformly. The materials prepared in this way showed minor segregation and traces of porosity (about 1%). A subsequent HIP treatment at 1140 °C for 3 h at 100 MPa produced a fully dense material, with a fine-scale microstructure, free of segregation. In Table 3.2, the chemical compositions and the crystal structures of the alloys studied in this work are listed.

Alloy	Aluminum at-%	Titanium at-%	Ternary : at-%	Structure
$Al_3(V,Ti)$	75	1.3	V: 23.7	DO_{22}
Al_5Ti_2Cr	67	25	Cr: 8	$L1_2$
$Al_5Ti_2(Mn,Cr)$	67	25	Mn: 4 / Cr: 4	$L1_2$
Al_5Ti_2Mn	67	25	Mn: 8	$L1_2$
$Al_5Ti_2Fe(1^{st})$	64	28	Fe: 8	$L1_2$
$Al_5Ti_2Fe(2^{nd})$	63	29	Fe: 8	$L1_2$
Al_5Ti_2Cu	62	27	Cu: 11	$L1_2$

Table 3.2: Chemical composition and crystal structures of the compounds prepared by Osprey spray deposition.

3.1.5 Powder Consolidation by HIP

The overspray powders from the Osprey deposition were used for further investigations. The mean size of these powders was roughly 50 µm and they were mechanically sieved to hold back pieces larger than 112 µm, namely, fragments chipped off from the billet or agglomerates from the chamber wall.

Mixing these powders with other metallic powders offers an easy way to prepare composites with an intermetallic matrix reinforced with a ductile second phase. In a first attempt, Al_5Ti_2Fe was used as the matrix material and different amounts of iron powder (size d: 100µm ≤ d ≤ 44 µm, 99.9 % pure). A second series based on Al_5Ti_2Mn powder as matrix and either Nb (100 µm ≤ d ≤ 44 µm, 99.8 % pure), V (74 µm ≤ d ≤ 37 µm, 99.7 % pure) or W

(100 μm ≤ d ≤ 44 μm, 99.9 % pure) additions. Table 3.3 gives more details to the composition of the composites.

Powder mixing was accomplished in the same Fritsch mill as for MA but without the balls. The mixing time was 15 min. To avoid oxidation, the same care was taken as for mechanical alloying, that means degassing the powders under vacuum and handling under argon. Cylindrical steel cans (about 40 mm long and about 12 mm in diameter) for HIP were welded under vacuum. The HIP treatment was done at 1140 °C under 100 MPa for 3 h. By this means, a fully dense material was obtained but there was also a considerable reaction zone between the metal powder reinforcements and the intermetallic matrix. Further details of the microstructure of the composites are discussed in section 6.

intermetallic matrix	second phase		
	element	vol-% powder	at-% powder
Al_5Ti_2Fe	Fe	1.37	1.88
Al_5Ti_2Fe	Fe	2.74	3.76
Al_5Ti_2Fe	Fe	5.48	7.52
Al_5Ti_2Mn	Nb	3.84	3.45
Al_5Ti_2Mn	V	3.98	4.73
Al_5Ti_2Mn	W	3.18	3.32

Table 3.3: Composition of the HIPped composites

3.2 Analytical Techniques

3.2.1 Electron Microscopy

A Cambridge Stereoscan 360 scanning electron microscope (SEM) was used for surface investigations. In the image mode of backscattered electrons (chemical contrast), the evolution in microstructure of the grains during MA and after homogenization was observed. The image mode of secondary electrons gives good topographical contrast. By this method the fracture surfaces and the beginning of cracking on compression samples were investigated.

Thin foils for transmission electron microscopy (TEM) examination were prepared by first cutting slices of 250 µm to 500 µm from a rod of 3 mm in diameter on a low speed saw (Buehler Isomet or Struers Accutom), polishing mechanically to a maximum thickness of 250 µm, if necessary, then thinning electrochemically in a Tenupol twin jet system. The thinning solution was 12 % perchloric acid and 35 % butoxyethanol in methanol. For the mechanically alloyed two phase material the foils were electropolished at - 20 °C and about 20 V. For the spray deposited Al_5Ti_2M intermetallics (where M is Cr, Mn, and Fe) the conditions were -18 °C and 25 V for 75 sec and finishing the thinning at 10 V. The TEM examinations were accomplished with a Philips CM12 instrument operating at 120 kV.

For the examination of dislocations the Burgers vectors were found using the $g \cdot b = 0$ criterion and taking micrographs of the same spot on different orientations near low indexed zone axes. Habit or glide planes of the dislocations were determined from the real directions of curved dislocations or, for superdislocations, from the projected separation of the two superpartials.

3.2.2 X-ray Diffraction

X-ray diffraction was used to confirm the crystalline structure of the Osprey billets. The examinations were carried out on a flat polished surface of bulk samples using a Philips diffractometer with Cu Kα monochromatised radiation. The lattice parameters were calculated directly from the 2Θ values without further corrections.

3.3 Mechanical Testing

3.3.1 Samples

Tensile tests were limited to mechanically alloyed Al-12.5%Ti material extruded to bars. The samples were machined from these rods to a shape fitting into the special grips for hot testing. The dimensions of the tensile samples are shown in figure 3.4.

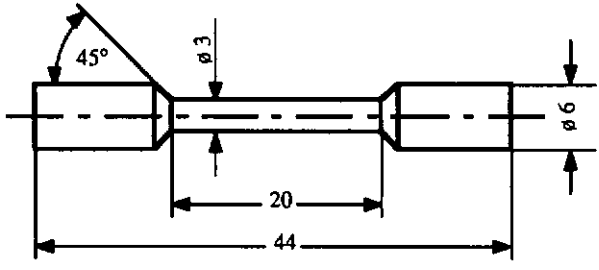

Figure 3.4 Tensile sample for high temperature testing. (Dimensions in mm)

Three-point bend tests were carried out on the ternary alloyed, spray deposited compounds. Rectangular bars 3.5 x 3 mm^2 in section were cut by spark erosion from the Osprey billets. These samples were lapped to obtain smooth, microcrack free surfaces. Hence, the final dimensions were about 3.4 x 2.9 x 20 mm^3. For testing the bending force was applied to the broader side.

The majority of the mechanical tests undertaken was in compression. The hot pressed billets prepared from mechanically alloyed powders were cut with a low speed saw. Small rods were cut out and carefully polished to a cuboidal form of about 3 x 3 x 5 mm^3. For spray deposited materials only spark erosion was successful in machining pieces of a precise shape. Rods of 3 mm in diameter and 6 mm long were electrodischarge machined and electropolished. The ends were hand lapped to ensure parallelism and smoothness.

3.3.2 Testing Machines

For compression and bend tests at RT and below, a Schenck RSA 100 universal testing machine was used. The hard platens on this machine (maximum load: 100 kN) allowed tests to be conducted till sample failure. The three-point bend tests were carried out using a support with a span length of 16 mm and a radius of 1.5 mm of the support edges and the applicator

edge. The cross head displacement was taken as a measure of deflection. For compression, the cross head displacement or a gauge fixed directly at the grips could be used alternatively for determination of the strain. The force-displacement curves were plotted on a X-Y-recorder. They were converted into real stress-real strain for calculation of the work hardening rate, activation volume and influence of the strain ageing on the flow stress.

Tests at elevated temperatures were carried out under argon atmosphere using a testing system comprising a high power image furnace, a Polanyi cage compression grips arrangement, and extensometers connected via alumina rods to the compression platens. This system was made of Nimonic 90 and installed on a Schenck RSA 10 testing machine. The temperature range for testing was limited from RT up to 700 °C. Heating and cooling up to this temperature and down RT took about 40 min each. The maximum applied stress could not exceed 1200 MPa on this system. For this reason, several tests had to be interrupted before failure. Generally, the compression samples were deformed at a cross head speed of 0.1 $^{mm}/_{min}$, corresponding to a strain rate of about $2 \cdot 10^{-4}$ sec^{-1}. The surface of the compression platens was polished to reduce the amount of friction. The identical geometrical dimensions of the samples guaranteed constant friction from test to test.

By changing the grips, the testing system allowed also tensile tests. Here the applied strain rate was about $8 \cdot 10^{-5}$ sec^{-1}. Figure 3.5 shows schematically the high temperature testing system (following page).

3.3.3 Testing Procedures

The tests for determination of the activation volume of the deformation mechanism and of the activation energy of the dynamic strain ageing (DSA) merit further discussion.

As stated in section 2.4.2, the activation volume is a measure of strain rate sensivity. The basis for the determination of U is changes in strain rate during compression testing. From the initial cross head speed of 0.1 $^{mm}/_{min}$ the strain rate was switched to 0.3 $^{mm}/_{min}$ and back to 0.1 $^{mm}/_{min}$ or up to 1.0 $^{mm}/_{min}$ and back to 0.1 $^{mm}/_{min}$ alternatively. On a fine scale force vs displacement plot the load was recorded with an accuracy better than 2 N and the displacement with an accuracy of about 1 µm. Due to this uncertainty in the load displacement plot, an upper and lower limit with the corresponding average of the values of ΔF were taken. The changes in load, ΔF, on increasing and decreasing the cross head speed were converted into real stress $\Delta\sigma$.

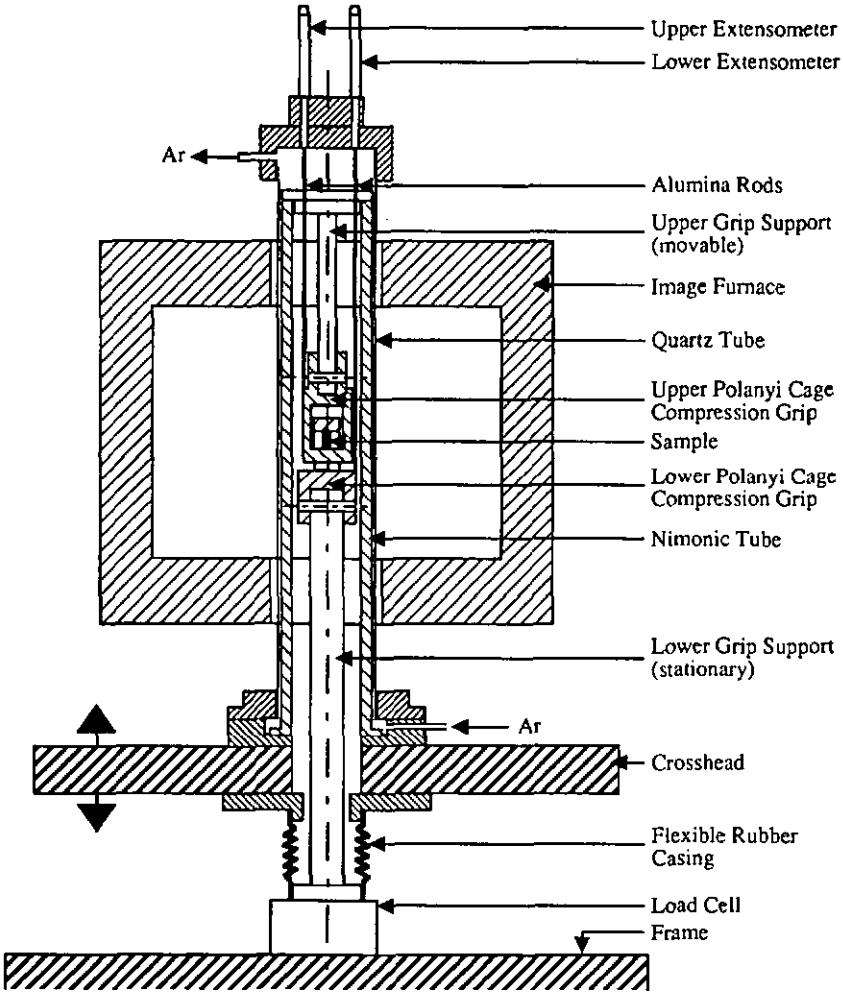

Figure 3.5 Schematical section through the high temperature testing system installed on a Schenck RSA 10 universal testing machine.

Strain ageing is related with the phenomeneon of jerky flow, the so called Portevin-LeChâtelier effect. A dislocation pinned by an atmosphere of solutes frees itself under a certain stress and is caught again if its velocity slows again. Imitating the waiting time of the pinned dislocation, an ageing procedure under load at different temperatures is used to determine the activation energy

for strain ageing, Q_{SA}. A compression sample is deformed more than 2%. At this amount of strain the "shoulder", i.e. a zone of low strain hardening on the stress-strain curve after yielding is overcome (see figure 3.6). Then the cross head is stopped and the stress lowered to 400 MPa for a given ageing time t_1. This stress can be held in a range of -10 MPa to + 5 MPa. After this ageing the compression test is restarted. The new yield point is higher than the stress reached before ageing. This increase is labelled $\Delta\sigma_a$. The strengthening is not permanent, but the stress drops back to a value which can be extrapolated from the curve before ageing. In other words, the $\Delta\sigma_a$ can be viewed as a hump in the stress strain curve. With further strain the stress drops back to the value expected without the interruption. The procedure is then started for another ageing time t_2. Over the whole ageing procedure the sample is deformed from about 2 % to about 5.5 %. Figure 3.6 shows schematically the influence of an ageing period on a stress vs strain curve. The ageing times were in the range of 15 sec up to 1 h and the ageing temperatures comprised the range of 100 °C to 300 °C.

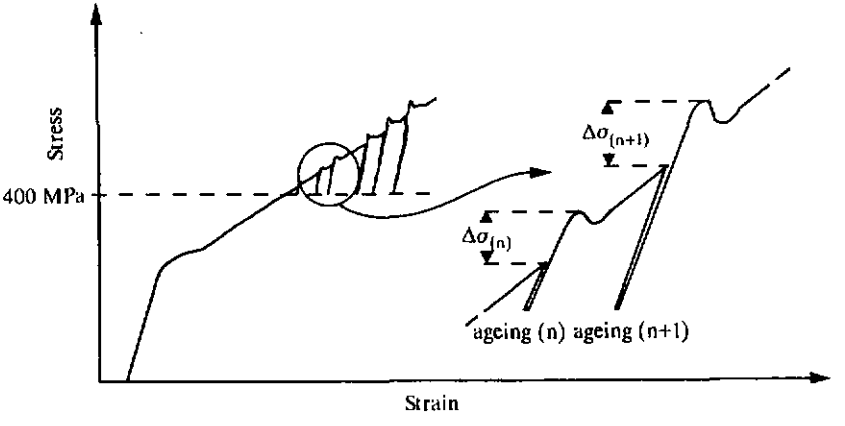

Figure 3.6 Schematic stress strain curve during the ageing procedure.

4. Results

4.1 Materials and Microstructures

The initial step of the preparation of the Osprey deposits is the casting of alloyed ingots with the desired chemical composition. Figure 4.1a shows the $Al_3(V,Ti)$ alloy in the cast and remelted state. At least three different phases may be detected in this sample. Particles darker than the matrix, needle-shaped and others, rather arbitrary in shape, indicate severe segregation through the formation of a primary V-rich phase. Solidification finishes by a peritectic reaction. Another phase, lighter than the matrix, is an analog primary Ti-rich compound. Some pores, often in the vicinity of the particles, are also seen. Considering this inhomogeneity, no further investigations on trialuminides in the cast state will be reported.

Figure 4.1b shows the $Al_3(V,Ti)$ compound after spray deposition and a HIP treatment at 1130 °C for 3 h. The microstructure is uniform and fine scaled with equiaxed grains of about 30 µm and shows only minor traces of impurity or second phases, particularly at grain boundaries and triple points. No porosity is visible.

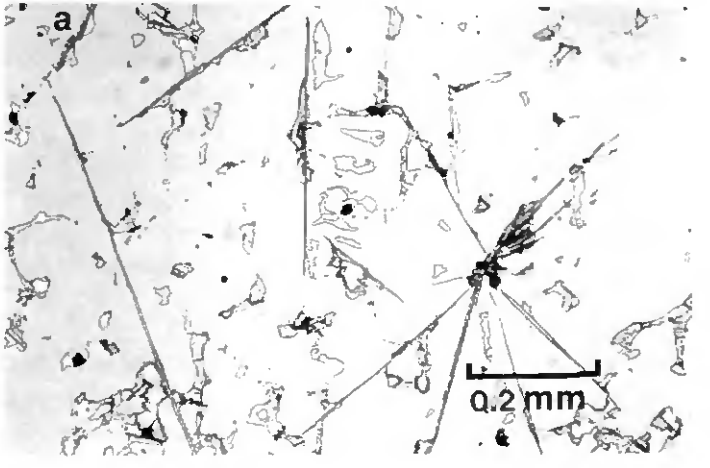

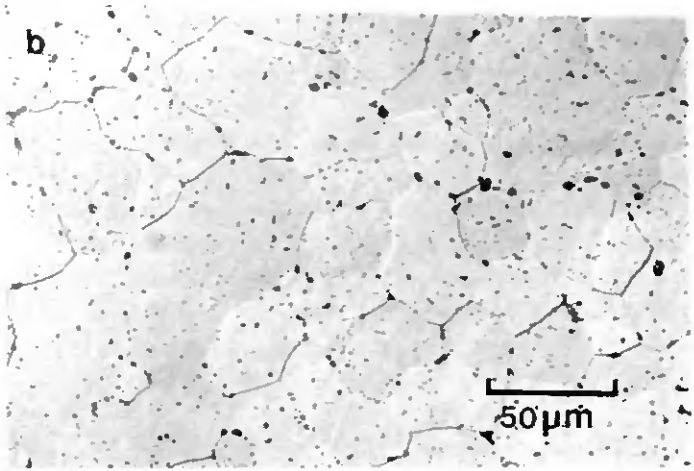

Figure 4.1: a) Microstructure of the cast and remelted $Al_3(V,Ti)$ alloy. Optical micrograph. b) $Al_3(V,Ti)$ after spray deposition and HIP treatment. Optical micrograph using Nomarski interference contrast.

A characteristic of almost all of the spray deposited intermetallics investigated are rows of inclusions perpendicular to the spray direction. The impurities, most likely oxides, mark the border between two spray layers, deposited one on the other. These layers are due to the deposition technique described in section 3.1.4. As an example, the microstructure of the $Al_5Ti_2(Mn,Cr)$ alloy is depicted in figure 4.2. In this photograph, the spray direction is horizontal. The inclusion rows are separated by about 200 µm. Sometimes they form a fine continuous line along grain boundaries. Otherwise, they are spread over several adjacent grain boundaries.

Two Al_5Ti_2Fe trialuminides with the same nominal composition were prepared. Due to technical problems, the first run of spray deposition had to be interrupted. Hence, only a small and relatively impure billet of about 15 mm in height could be obtained. A second, successful run starting with another melt stock gave a bulk composition of the Osprey billet slightly richer in Ti (cf. table 3.2). This small shift in stoichiometry gives rise to two different microstructures as illustrated in figure 4.3. The material of the first run is presented in figure 4.3a. Second phase particles (marked by small arrows) of a size up to 10 µm and smaller dark precipitations or impurities, often seen in agglomerates, are visible. Nevertheless, the matrix grains are uniform, with a grain size of about 20 µm. No concentration of small particles at the grain boundaries is observed. In the Al_5Ti_2Fe alloy of the second run, figure 4.3b, the grains are larger, i.e. about

35 µm and dark impurities are concentrated mostly on the grain boundaries. But the main difference to the microstructure of the first deposition attempt are the "basket weave" like precipitations within the grains. Carried out in a parallel work, TEM analysis shows that these lamellar precipitations are of the composition Al_2Ti. In addition, the matrix contains many shear faults. Long period superlattice structures are seen intermediate between $L1_2$, DO_{22} and the Al_2Ti-type phase. These investigations are not subject of the current thesis and are reported elsewhere [50].

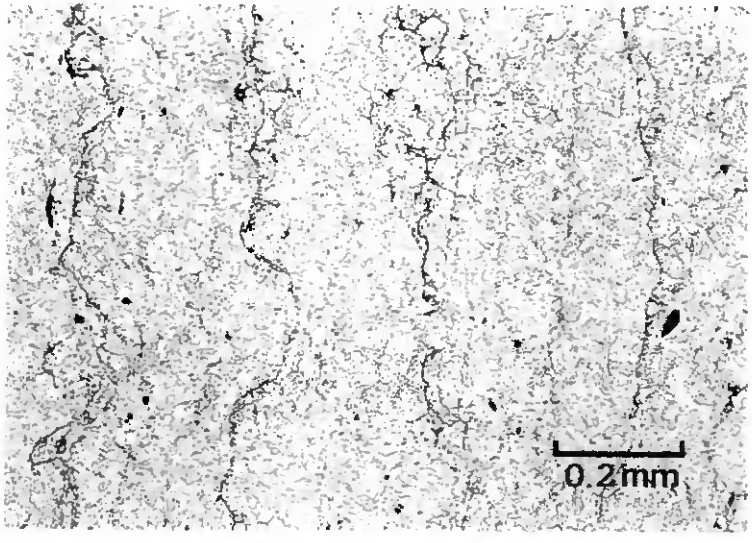

Figure 4.2: Spray layers due to the preparation by Osprey spray deposition. The spray direction is horizontal. Optical micrograph of the Al_5Ti_2(Mn,Cr) alloy.

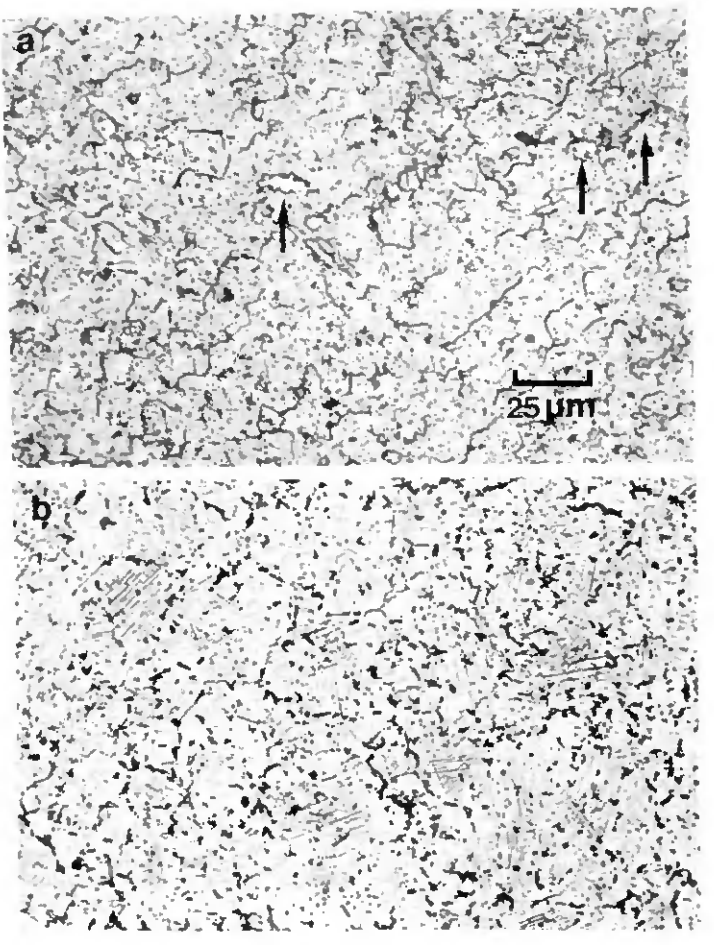

Figure 4.3: Optical micrographs of the Al_5Ti_2Fe alloys, using Nomarski interference contrast. a) First Osprey run, small arrows point to coarse second phase particles. b) Second run, having "basket weave" precipitations within the grains.

While no chemical analysis of the effective bulk composition was accomplished, some particles in Al_5Ti_2Fe (1^{st}) have been analysed using EDS and electron diffraction. Figure 4.4 shows a TEM micrograph with several particles of different shape and size (cf. ref. [51]):

1) Plates, they are analysed by EDS as about 60 at-% Al, 35 at-% Ti and 5 at-% Fe. Diffraction shows a large lattice parameter in one direction (≈1.2 nm). This phase is identified as Al_2Ti.

2) Dark, blocky particles, they are analysed by EDS as 50-60 at-% Ti, 30-40 at% Si and small amounts of Al and Fe. Diffraction shows a hexagonal structure. This phase is identified as Ti_5Si_3.

3) Irregular particle masses. Some of this material is amorphous and Al-rich, while particles contained within these masses are identified as Ti_3Al and Al_2Ti.

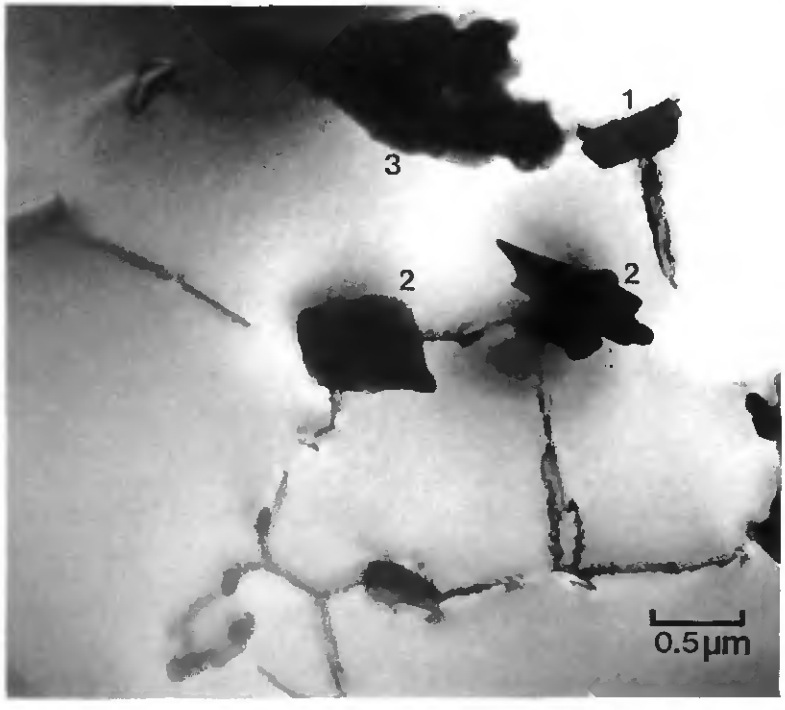

Figure 4.4: TEM micrograph showing impurity phases in Al_5Ti_2Fe (1^{st}). 1) Al_2Ti plates, 2) Ti_5Si_3 and 3) irregular agglomerates.

In summary, the trialuminides prepared by spray deposition combined with a HIP treatment exhibit a fine scale, equiaxed microstructure with no detectable porosity or macrosegregation

and, with exception of Al_5Ti_2Fe (1^{st}), small amounts of impurities. The grain size comprises the range of 20 µm to 35 µm. Considering the microstructures presented above, the Osprey alloys can be classified as follows:

A group comprising $Al_3(V,Ti)$, Al_5Ti_2Cr, Al_5Ti_2Mn and $Al_5Ti_2(Mn,Cr)$ contains second phase particles on the level of impurities. The microstructure of these four compounds are very similar to that of $Al_3(V,Ti)$ shown in figure 4.1b. In spite of the considerable amount of relatively coarse second phase particles the first run Al_5Ti_2Fe is also part of this group (cf. figure 4.3a).

The two alloys Al_5Ti_2Fe (2^{nd} run) and Al_5Ti_2Cu exhibit both the "basket weave" precipitations illustrated in the micrograph of Al_5Ti_2Fe (2^{nd} run) in figure 4.3b.

X-ray diffraction confirms the DO_{22} crystal structure of $Al_3(V,Ti)$ and the $L1_2$ structure for all the other alloys, namely Al_5Ti_2Cr, Al_5Ti_2Mn, $Al_5Ti_2(Mn,Cr)$, Al_5Ti_2Fe (1^{st} and 2^{nd} run) and Al_5Ti_2Cu. The X-ray patterns indicate single phase or nearly single phase materials with occasionally a few additional minor peaks. Unfortunately second phases cannot be identified from these results. The lattice parameters are summarized in table 4.1.

alloy	crystal structure (Strukturbericht)	lattice parameters		
		a [nm]	c [nm]	c/a
$Al_3(V,Ti)$	DO_{22}	0.3784	0.8336	2.203
Al_5Ti_2Cr	$L1_2$	0.3958	-	-
$Al_5Ti_2(Mn,Cr)$	$L1_2$	0.3954	-	-
Al_5Ti_2Mn	$L1_2$	0.3958	-	-
$Al_5Ti_2Fe(1^{st})$	$L1_2$	0.3949	-	-
$Al_5Ti_2Fe(2^{nd})$	$L1_2$	0.3942	-	-
Al_5Ti_2Cu	$L1_2$	0.3935	-	-

Table 4.1: Crystal structure and lattice parameters of the alloys prepared by spray deposition. In the cubic $L1_2$ structure $a = c$.

The a and c values of $Al_3(V,Ti)$ (with only 1.3 at-% Ti) are very close to the lattice constants reported for Al_3V in ref. [11], i.e. $a = 0.3780$ nm, $c = 0.8321$ and hence $c/a = 2.201$. The lattice parameters of the cubic $L1_2$ phase are almost identical to those reported in the literature. For an overview see ref. [7]. The lattice parameters of the $L1_2$ compounds are larger than the a value ($a = 0.3848$ nm [11]) and smaller than half of the c value ($c = 0.8596$ nm [11]) of the tetragonal Al_3Ti phase and increase with decreasing atomic number of the ternary element. For

example consider a Cr atom occupying the $0,0,^1/_2$ Al site in a DO_{22} cell (cf. figure 2.1). Ignoring the destabilisation of the structure with respect to the $L1_2$ structure, a decrease in the *c* parameter is observed which arises from two factors. First, the Cr atom (as well as Mn, Fe and Cu) is smaller than the Al it replaces. Second, because the directionality of the Al*p* - Ti*d* interaction is replaced by the more isotropic Cr*d* - Ti*d* bonds, the new configuration permits contraction in the *c* direction. Changes in bonding in the *a* direction will be smaller since the effect of the four new Cr - Ti bonds is reduced by the four (less affected) new Cr -Al bonds. As discussed in section 2.1, the replacement of Al with Cr yields more *d*-*d* bonding between Ti and Cr. As elements other than Cr, with greater numbers of d electrons, are alloyed, the *d*-*d* bonding becomes stronger, leading to cubic phases with smaller lattice parameters. Hence, the decrease of the parameter *a* with increasing atomic number of the alloying element, i.e. filling the *d* shell of fourth row transition metals, can be understood.

4.2 Mechanical Testing

4.2.I Introduction

Compression tests have been performed on all materials. The emphasis of the research was focused on the Al_5Ti_2Cr, Al_5Ti_2Mn, and Al_5Ti_2Fe (first run) compounds because these three materials exhibit good ductility in compression. The $Al_5Ti_2(Mn,Cr)$ was not considered because its properties are very close to those of Al_5Ti_2Mn as well as Al_5Ti_2Cr.

4.2.2 Hardness Tests

Hardness testing gives an initial estimate of the strength of the alloys but can also help to quantify toughness. At a certain load, the indentation of a Vickers diamond pyramid in brittle materials causes cracking. There are standardized equations to deduce K_{Ic} values from the crack length, as well as defined strict limits of applicability (for an overview see e.g. ref. [52]). Unfortunately, the current trialuminides do not fulfill these conditions. Instead of observing the required four cracks starting at each corner of the indentation, only two cracks or a extensively deformed region full of small flaws around the mark of the diamond pyramid are seen. Hence, the resistance against cracking is reported only by a qualitative measure, i.e. the maximum load under which a Vickers hardness test leaves no cracks. Table 4.2 shows hardness values and the maximum load applied without crack formation at the surface outside of the indentation.

alloy	hardness [HV_{30}]	crack-free load [kgf]	remarks
Al_5Ti_2Cr	231 ± 5	31.25	extensive plastic deformation around indentation
$Al_5Ti_2(Mn,Cr)$	177 ± 10	30	
Al_5Ti_2Mn	183 ± 3	31.25	
Al_5Ti_2Fe (1^{st})	280 ± 10	30	
Al_5Ti_2Fe (2^{nd})	445 ± 33	7.81	irregular cracks
Al_5Ti_2Cu	396 ± 15	3.9	
$Al_3(V,Ti)$	300 ± 4	5.85	

Table 4.2: The results of the hardness tests. "Crack-free load" refers to the maximum load applied on the diamond pyramid without visible cracks starting from the indentation.

4.2.3 Compression Tests

The results of the compression tests are summarized in table 4.3. If a scatter is listed, at least three tests are averaged at the corresponding temperature. The sign ">" means that the test had to be interrupted because of the load limit. For illustration, the yield stress as a function of temperature is represented graphically in figure 4.4. The mechanical data will be listed in the order of strength.

1) The highest strength, i.e. more than 1000 MPa at RT is exhibited by the Al_5Ti_2Cu alloy. But this material has almost no ductility at RT.

2) Al_5Ti_2Fe of the second series is characterized by its high strength, also more than 1000 MPa at RT, and by a ductility in compression of about 10 % at 23 °C as well as at 700 °C.

3) Al_5Ti_2Fe of the first series shows an anomalous strengthening at temperatures above 500 °C. The stress decreases somewhat from 500 MPa to about 430 MPa between cryogenic temperatures and 400 °C and, thereafter, shows a continuous increase up to 490 MPa at 700 °C. The material exhibit a ductility of about 20 % over the whole temperature range.

4) An extreme brittleness at low and intermediate temperatures is seen with the tetragonal $Al_3(V,Ti)$ compound, combined with a strength of about 350 MPa at temperatures between RT and 700 °C.

5) The trialuminide alloyed with Cr is the next lower in strength. From 410 MPa at RT and below, the yield point falls to 315 MPa at 300 °C. At higher temperatures, the yield stress is rather constant, perhaps with a small peak in strength at 400 °C. But there is no clear anomalous strengthening in this material. The ductility rises from 23 % at RT to 37 % at 700 °C.

6) Concerning strength, $Al_5Ti_2(Mn,Cr)$ lies between Al_5Ti_2Cr and Al_5Ti_2Mn. A yield stress of about 340 MPa at RT and about 280 MPa at 700 °C is observed. This material shows good ductility in compression, 26 % at RT and 42 % at 700 °C.

7) Al_5Ti_2Mn is the alloy with the lowest strength. From the value of 340 MPa at the temperature of liquid nitrogen, the yield stress decreases slightly to 270 MPa with increasing temperature up to 300 °C, remains constant up to 500 °C and decreases again towards 240 MPa at 700 °C. The data of ductility are about 25 % at 23 °C as well as at 500 °C and 44 % at 700 °C.

alloy	test temperature [°C]	0.2 % yield stress [MPa]	maximum stress [MPa]	strain at failure [%]
Al_5Ti_2Cr	-196	408 ± 8	> 710	> 5.0
	23	413 ± 49	1763 ± 281	23.2 ± 4.7
	200	354 ± 56	> 1146	> 18.8
	300	314 ± 22	>1197	> 15.1
	400	340 ± 46	> 1183	> 15.9
	500	326 ± 16	> 1118	> 20.1
	600	305	> 883	> 16.4
	700	321 ± 28	1173	36.9
$Al_5Ti_2(Mn,Cr)$	23	342 ± 12	1717 ± 58	26.1 ± 1.8
	500	326 ± 19	> 1163	> 22.2
	700	282 ± 5	1006 ± 124	42.2 ± 6.8
Al_5Ti_2Mn	-196	340 ± 40	> 1064	> 14.9
	-60	368	>1241	> 17.0
	23	311 ± 30	1517 ± 19	24.0 ± 0.9
	100	291	> 1102	> 15.4
	200	293 ± 40	> 1154	> 15.7
	300	275 ± 18	> 1133	> 17.1
	400	276 ± 8	> 1205	> 20.3
	500	274 ± 12	1142 ± 9	26.5 ± 1.5
	600	260 ± 12	> 846	> 20.6
	700	241 ± 14	903 ± 99	43.8 ± 6.1
$Al_5Ti_2Fe(1^{st})$	-196	506 ± 17	> 1103	> 6.9
	-60	524	> 1376	> 11.2
	23	459 ± 23	1748 ± 110	19.2 ± 1.5
	100	460	> 1107	> 9.8
	200	446	> 1113	> 8.4
	300	432 ± 4	> 1128	> 9.2
	400	441 ± 25	> 1152	> 10.2
	500	437 ± 22	> 1168	> 10.5
	600	449 ± 22	1194 ± 48	20.6 ± 2.2
	700	488 ± 17	1028 ± 22	21.1 ± 2.0
$Al_5Ti_2Fe(2^{nd})$	23	1037 ± 12	1546 ± 68	10.3 ± 1.9
	500	891 ± 73	> 1151	> 2.8
	700	886 ± 4	1181 ± 6	9.7 ± 0.7
Al_5Ti_2Cu	23	1041 ± 76	1075 ± 85	0.0 ... 6.5
	600	980	> 1050	> 0.5
	700	927 ± 15	> 1075	> 0.9
$Al_3(V,Ti)$	23	338 ± 14	478 ± 102	0.0 ... 3.2
	500	384 ± 51	460 ± 101	0.0 ... 5.2
	600	317 ± 1	583 ± 84	6.0 ± 2.8
	700	389 ± 52	706 ± 104	14.4 ± 4.0

Table 4.3: (preceding page) Results of the compression tests at different temperatures.

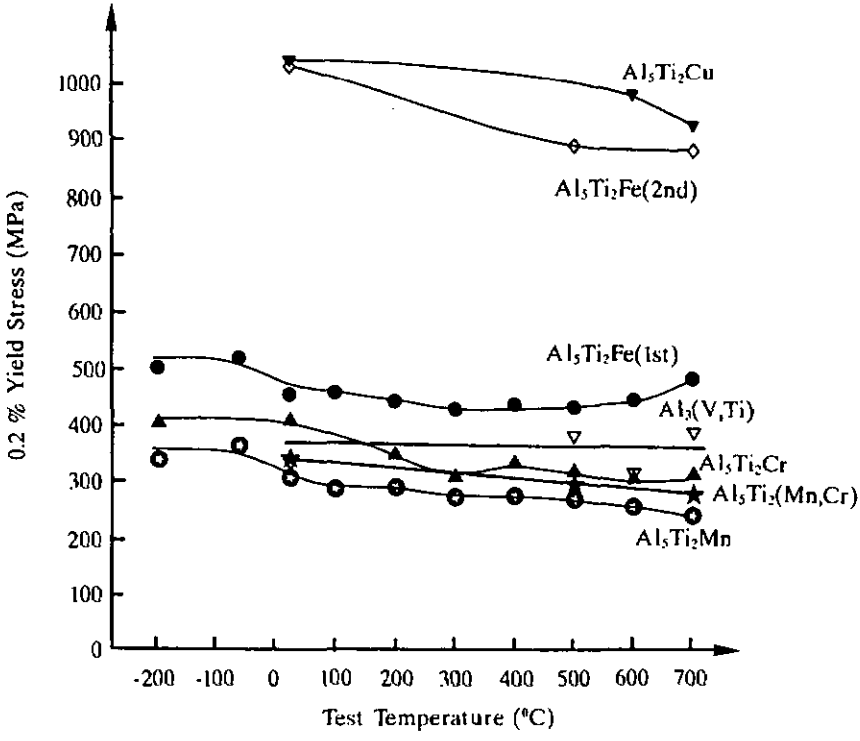

Figure 4.5: Yield stress, $R_{p0.2}$, as a function of temperature T.

For those materials exhibiting a reasonable ductility, the maximum stress is much higher than the yield stress at room temperature because of the large extent of work hardening. As mentioned earlier (section 3.3.2), tests are carried out to failure at RT, but at higher temperature, the stress limit imposed by the plattens of the high temperature testing system requires to interrupt many tests before failure occured. Only in the range of 500 °C to 700 °C, most of the samples can be deformed till failure. Hence, in this temperature range, the maximum stress falls compared to the values measured at RT.

The work hardening rate of all the ductile samples, i.e. Al_5Ti_2Cr, Al_5Ti_2Mn, $Al_5Ti_2(Mn,Cr)$ and Al_5Ti_2Fe (1^{st} and 2^{nd}) are very high, between 5 and 8 GPa at RT, and still 4 GPa in the

first few % of plastic deformation at 700 °C. Figure 4.6 presents the work hardening rate, ϑ, as a function of the flow stress, σ, for three different temperatures, namely 23 °C, 500 °C and 700 °C. A general aspect of these graphs is the slope of the curves for the different alloys. While at RT, ϑ decreases only slightly with increasing flow stress, even stabilizes towards high stresses, at 500 °C and 700 °C, ϑ decreases considerably faster with increasing flow stress. Looking at individual materials, the two trialuminides alloyed with Fe behave both differently from the Al_5Ti_2Cr, Al_5Ti_2Mn and $Al_5Ti_2(Mn,Cr)$ alloys. Al_5Ti_2Fe (1^{st}) has the highest work hardening rate, at least at RT and 500 °C as well as a somewhat steeper slope than the non iron intermetallics. Al_5Ti_2Fe (2^{nd}) is distinguished by the steepest slope at each temperature.

It is well known that strength and ductility are contrary properties, i. e. an increase in one property is usually offset by a decrease in the other property. A stress vs strain at failure diagram is shown in figure 4.7. The yield stress, $R_{p0.2}$, and the maximum stress, R_m, are plotted as a function of the corresponding maximum deformation. The data for room temperature and 700 °C are shown. $R_{p0.2}$ for all alloys and both temperatures can be approximated by a single hyperbolic line, as would be expected from one hardening alloy. R_m does not differ significantly from one material to another at the same temperature. While the stress as a function of strain at failure, ε_{max}, increases somewhat for the more ductile materials at RT, the data points at 700 °C lie in a scatterband between 900 MPa and 1200 MPa. The tetragonal $Al_3(V,Ti)$ phase does not behave like the $L1_2$ trialuminides. The DO_{22} compound is less ductile coupled with lower strength. For comparison, the properties of $Al_3(V,Ti)$ are represented by squares in figure 4.7.

There is no clear dependence between the maximum stress and the ductility neither at RT nor at 700 °C. The best description are two horizontal scatter bands comprising the data points at RT and 700 °C, respectively. In other words, within a certain range, the maximum stress is constant for the present trialuminides with $L1_2$ structure. The reason for this will be discussed in section 5.2. In this view-point, the ductility in compression can be understood as related to the difference between the yield point and the maximum stress. Due to the much lower work hardening rate at 700 °C (cf. figure 4.5), the materials exhibit better ductility at 700 °C in spite of the lower R_m. In other words, the ductility of the five different compounds alloyed with four different elements is determined by a yield stress and a work hardening rate as low as possible. The factors influencing the work hardening will be discussed in section 4.3.

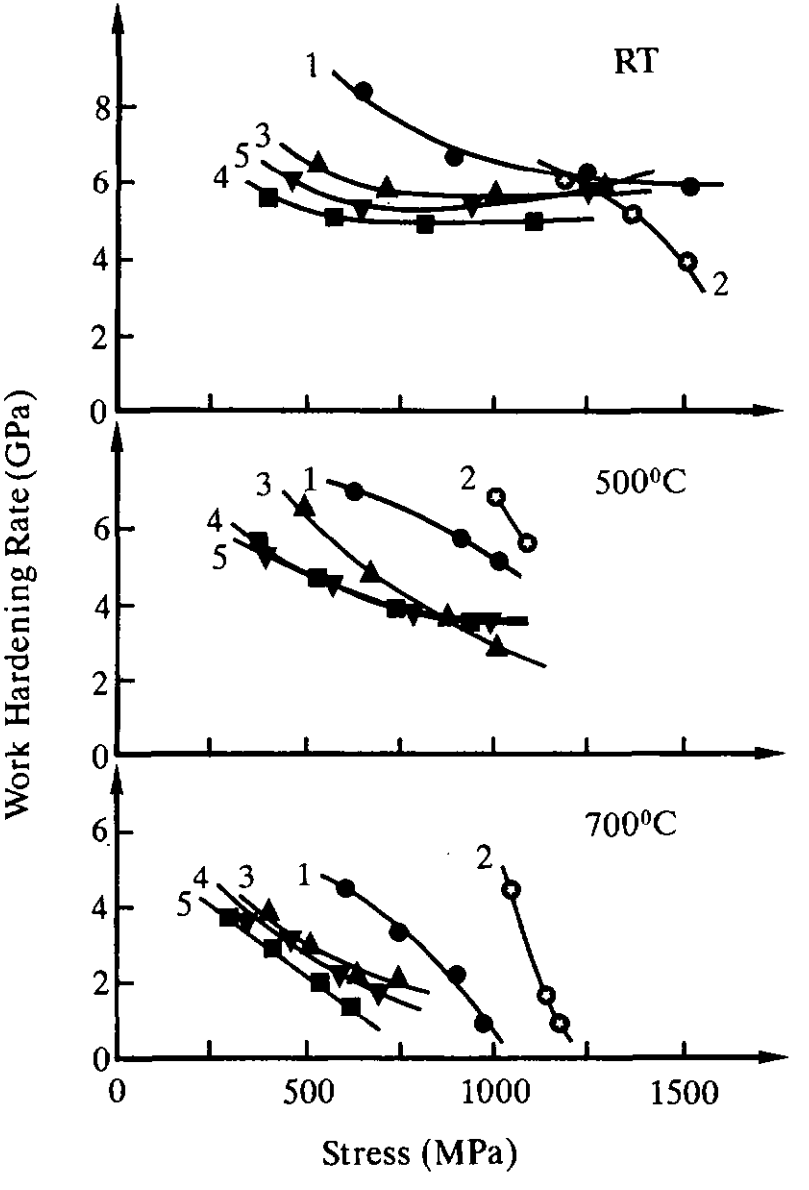

Figure 4.6: Work hardening rate as a function of the flow stress for three different temperatures. 1: Al_5Ti_2Fe (1^{st}), 2: Al_5Ti_2Fe (2^{nd}), 3: Al_5Ti_2Cr, 4: Al_5Ti_2Mn and 5: $Al_5Ti_2(Mn,Cr)$

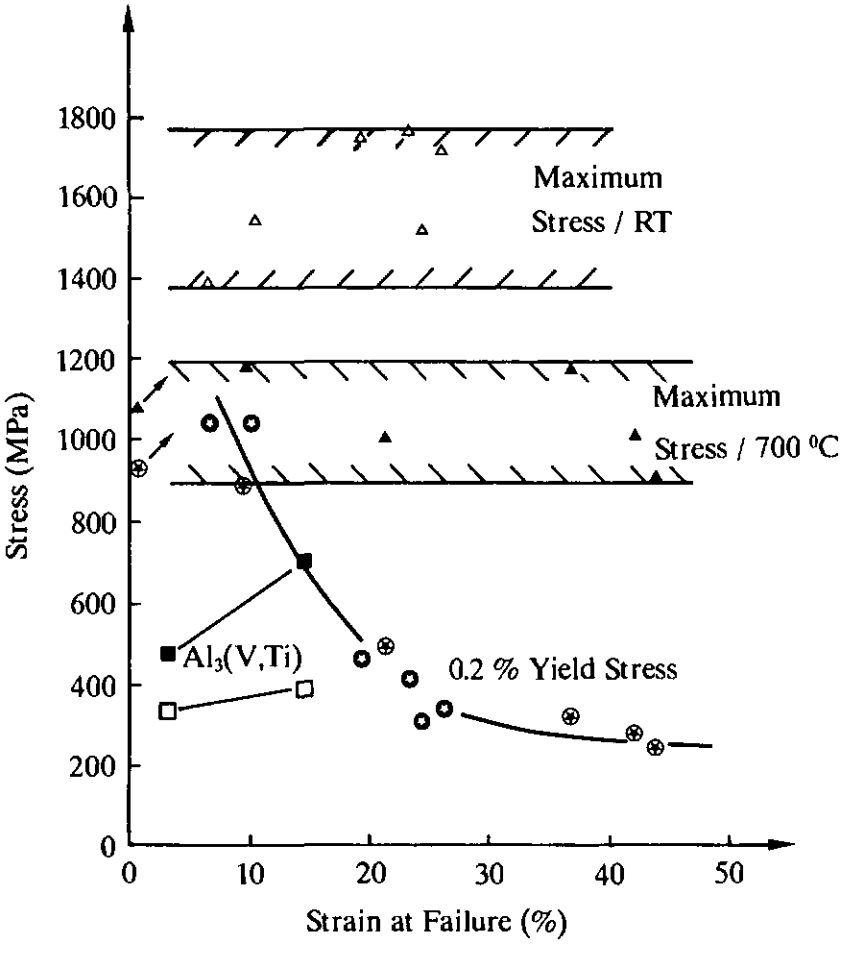

Figure 4.7: Yield stress and maximum stress as a function of the strain at failure. The data for the $L1_2$ compounds, Al_5Ti_2Cr, Al_5Ti_2Mn, $Al_5Ti_2(Mn,Cr)$, Al_5Ti_2Fe (1^{st}), Al_5Ti_2Fe (2^{nd}) and Al_5Ti_2Cu at RT and 700 °C are shown. RT is represented by open signs, 700 °C by full signs. For comparison, the data of $Al_3(V,Ti)$ are represented by squares.

Failure occurred at RT in a sudden way. For the brittle alloys, i.e. $Al_3(V,Ti)$ and Al_5Ti_2Cu, the samples disintegrated in many small pieces. The other, tougher materials (Cr, Mn and Fe

alloyed) broke in two larger, conical and some small fragments. The base of these cones were the polished ends of the cylindrical samples. This geometry suggests that the conical pieces correspond to the dead zone of the samples deformed under compression. At high temperatures, the two brittle compounds still failed by disintegration. Both Al_5Ti_2Fe showed still the failure characterized by the conical fragments. But at temperatures of 600 °C and above, Al_5Ti_2Cr, Al_5Ti_2Mn and $Al_5Ti_2(Mn,Cr)$ failed in a unspectacular way. Two diametrically opposed longitudinal cracks opened more and more. This behaviour lead to a continous change in the force-displacement plot and impeded the exact determination of the beginning of cracking.

The fracture surfaces show brittle cleavage failure over the whole temperature range. There are little differences in character between the failure surfaces of the different alloys as well as between the different temperatures. The cleavage facets are generally irregular because of the interaction with particles inside the grains and breakage at the grain boundaries.

Even for the samples exhibiting a good ductility in compression, the first cracks can be detected long before failure, at strains as low as 2 % to 3 %. Cracking starts at the surface in the middle of the sample. The first detectable cracks are longitudinal and about 10 µm in length. With increasing strain, more cracks nucleate farther away from the middle, existing cracks grow and join forming still longer flaws as well as branching out of the direction parallel to the deformation axis. A preferred site for crack nucleation are scratches originating from machining or handling. Figure 4.8a shows such a scratch perpendicular to the compression axis on a Al_5Ti_2Cr sample deformed 5 %. Sometimes cracks nucleate on inclusions or grain boundaries attacked by the electropolishing and sometimes there seems to be no "weak point" in the vicinity of the 10 µm cracks. Figure 4.8b illustrates that grain boundaries can stop cracks (marked by arrows) as well as the grain boundaries can separate and form cracks (marked by a circle). The small pieces after failure, described above, are thought to be separated by such breaks starting at the surface.

As will be discussed in the following section, $L1_2$ trialuminides seem to be unable to deform plastically under tension. The beginning of a measurable barreling of the cylindrical samples falls together with the first cracking, i. e. at a strain of about 2 %. The barreling is due to the friction between the polished end of the sample and the compression platens. Measurements of the maximum diameter after 5 %, 10 % and 15 % strain show that different samples behave similary under defomation in compression. Hence, the friction must be about the same in all cases. Barreling leads to a triaxial stress state inside the sample and a tensile circumferential stress. Hence, as soon as the hoop stress at the surface exceeds the end of the elastic range of deformation, the materials respond by separating the atomic planes, i.e. cracking. Residual

tensile stress, induced by the scratch deformation, enhances the triaxial stress state at the surface.

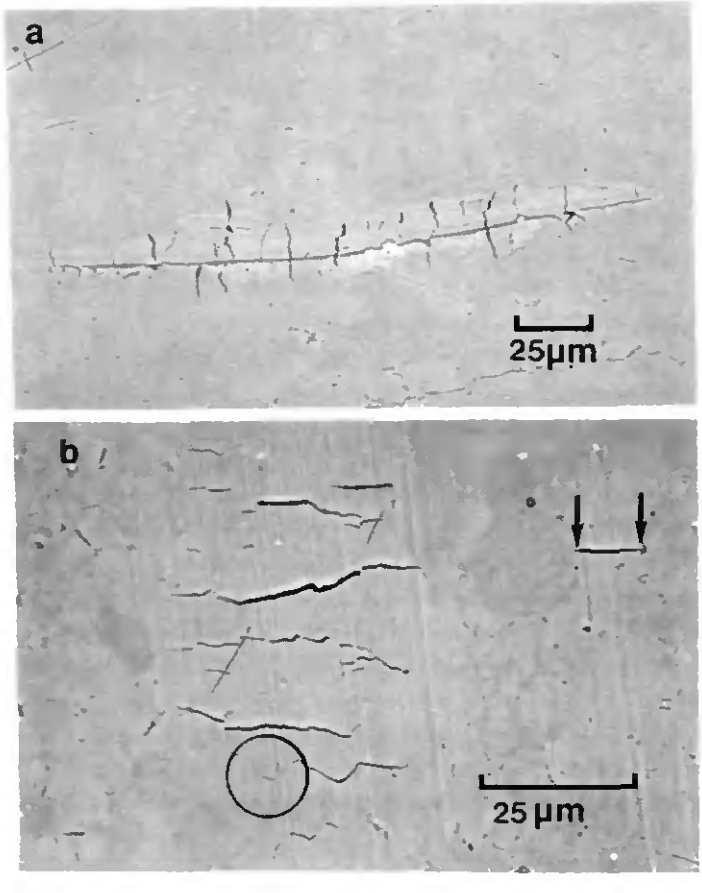

Figure 4.8: SEM micrograph of a Al_5Ti_2Cr compression sample after 5% strain. a) Crack nucleating on a scratch, compression axis vertical, b) crack nucelation (circle) and crack stop (arrows) at grain boundaries, compression axis horizontal.

At many of the temperatures used for testing, the load-displacement curves showed rapid load serrations. The jerky flow begins at about 200 °C and at a strain $\varepsilon > 12$ % and continues until about 600 °C where only a few irregular oscillations directly after yielding are observed. This inhomogeneous flow has all the characteristics of the Portevin-LeChâtelier effect including a

negative strain rate sensitivity, as will be discussed in the section 4.2.5. The form of the serrations as well as the temperature and strain at their beginning and their end are very similar for all $L1_2$ compounds, namely Al_5Ti_2Cr, $Al_5Ti_2(Mn,Cr)$, Al_5Ti_2Mn and Al_5Ti_2Fe (1^{st} and 2^{nd}). The amplitude of the serrations seems to be proportional to the strength of the material. The ratio maximum amplitude to yield stress is $\Delta\sigma/R_{p0.2} \approx 0.15$ for Al_5Ti_2Cr, Al_5Ti_2Mn and Al_5Ti_2Fe (1^{st}) at 300 °C and 400 °C. The tetragonal $Al_3(V,Ti)$ material exhibits no consecutive serrations. As an example, figure 4.9 shows the stress-strain curves of Al_5Ti_2Fe (1^{st}) at 300 °C, 400 °C and 600 °C. At 300 °C the flow is inhomogeneous all along the deformation till the test is interrupted because of the load limit. At low strains the oscillations are small in amplitude, $\Delta\sigma$. $\Delta\sigma$ increases with increasing strain and at the same time the frequency of the serrations decrease slightly. Nevertheless, the oscillations are relatively regular. At 400 °C, the serrations start with higher amplitude after yielding than at 300 °C. With increasing strain they become more irregular, both in $\Delta\sigma$ as well as in frequency. Before the test is interrupted, there is a zone of a few % strain of homogeneous flow. At 600 °C, some irregular serrations are observed after yielding. However, the jerky flow stops after 1 % to 2% strain. At temperatures below 200 °C, diffusion is too slow to affect dislocation movement and above 600 °C, diffusion is rapid enough to follow quasi instantenously the dislocation. The materials deform homogeneously.

In the Portevin-LeChâtelier effect, a serration is interpreted as a cascade of unpinning dislocations. It is proposed that these dislocations are trapped by a diffusional mechanism. Interstitial or substitutional atoms diffuse to the dislocation and pin it due to the locally higher solution hardening (cf. section 2.3.2) or the relaxation of the dislocation changes the chemical and/or ordering state around the dislocation core (cf. section 2.3.3). At a certain stress level, the dislocations can escape from their pinning points, giving rise to an abrupt decrease of the flow stress. If the temperature or the strain is too low that the dislocation can overcome the trapping a normal strengthening of the material is observed. This phenomenon is known as dynamic strain ageing (DSA).

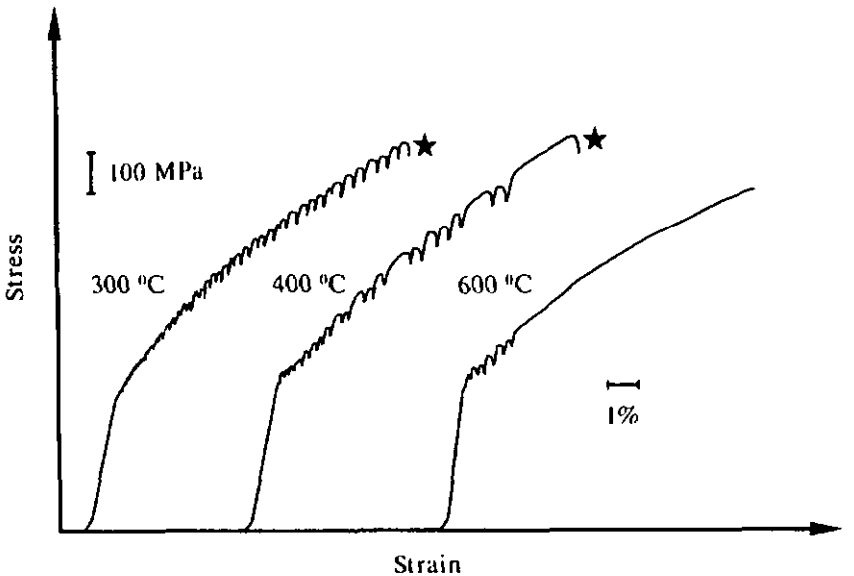

Figure 4.9: Stress-strain curves for Al_5Ti_2Fe (1^{st}). The jerky flow (Portevin-LeChâtelier effect) is depicted for 300 °C, 400 °C and 600 °C. The star refers to an interruption of the test.

4.2.4 Bend Testing

The bend tests focused on the Al_5Ti_2Cr and Al_5Ti_2Mn materials. Al_5Ti_2Fe (1^{st}) would have been an interesting candidate, but the billet was too small to machine bend samples out of it. To investigate the influence of the spray layers described in section 4.1, samples of both compounds were tested in three different orientations. In the first orientation (TP), the layers lie transverse in the sample and parallel to the applied force, in the second orientation (LP), longitudinal and parallel to the force and in the third (PP) perpendicular to the force. Figure 4.10 illustrates the spray layers in relationship to the samples. The TP orientation represents the worst case because the layers are parallel to the expected crack path and could induce cracking. But within the scatter, there are no differences between these orientations, neither in strength nor in ductility. The best plastic deformation for Al_5Ti_2Cr is observed in the PP orientation, for Al_5Ti_2Mn in the TP orientation.

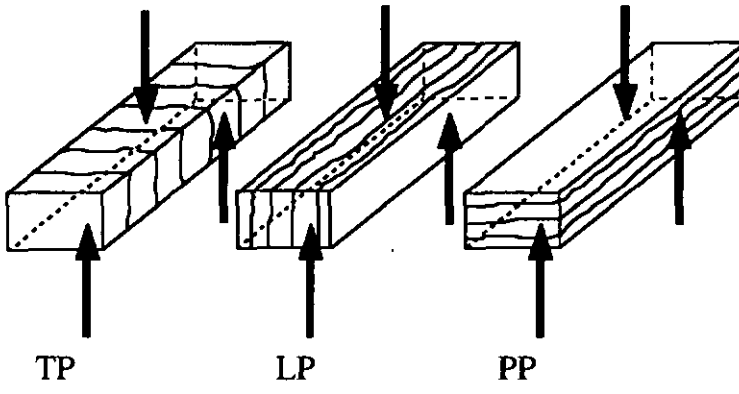

Figure 4.10: The orientation of the spray layers within the bend samples. The direction of the applied force is indicated by arrows.

Figure 4.11 shows the force displacement curves of some bend tests. It is clearly seen that these materials exhibit only poor ductility in bending. Failure occurs abruptly as seen in the graphs.

The plastic deformation, ε_{pl}, is calculated using the equation proposed by Dadras [53]:

$$\varepsilon_{pl} = -\frac{F_e\, l\, \sqrt{3}}{E\, b\, 4}\left(\frac{b\, h^2 (F_e + F_m)}{F_e}\right)^{-0.5} \qquad (4.1)$$

Where b is the width, h the height, l the loaded length of the sample, E the elastic modulus, F_e the yield force and F_m the maximum force. This formula assumes elastic-perfect plastic behaviour of the material and is restricted to small plastic deformations. Table 4.4 summarizes the results of the bend tests. All three orientations are averaged together.

alloy	yield stress [MPa]	maximum stress [MPa]	plastic deformation [%]
Al_5Ti_2Cr	329 ± 35	349 ± 47	0 ... 0.03
Al_5Ti_2Mn	306 ± 12	328 ± 10	0 ... 0.34

Table 4.4: The results of the bend tests. The plastic deformation is calculated using eq. 4.1.

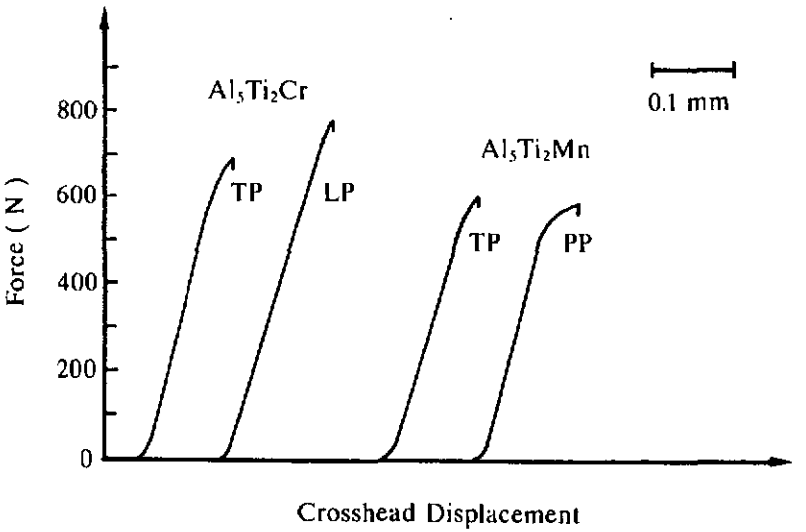

Figure 4.11: Force-displacement curves of two Al_5Ti_2Cr and Al_5Ti_2Mn samples each. TP, LP and PP indicate the orientation of the spray layers within the samples (cf. figure 4.10).

The yield stress of the Al_5Ti_2Mn alloy corresponds well to that measured in compression ($R_{p0.2}$ = 311 MPa). The strength of the Al_5Ti_2Cr compound is considerably lower in bending than in compression ($R_{p0.2}$ = 413 MPa). Bending is very sensitive to flaws in the small, highly deformed zone under the applied force. Imperfections in the microstructure cause stress concentrations and reduce the load bearing section of the samples. Hence, the finally determined strength is smaller than that expected from the outer geometry. However, there is no evident difference in microstructure between the Cr and the Mn alloyed compound.

The fracture surfaces show brittle cleavage failure, similar to those observed on samples failed in compression. Even at the edge to the inferior side of the sample, no signs of plastic deformation are detected. A first small crack, similar to those reported in the preceding section for compression is probably catastrophic in bending. Considering the inexistence of characteristics of plastic deformation on the fracture surfaces, such cracks open under tensile load at very low strains, directly after the purely elastic elongation. The purity may have an influence on the toughness of these trialuminides. A pure material without internal or external notches will

exhibit a larger tensile deformation. But failure will still occur by cleavage and the absolute value of ductility will remain poor.

4.2.5 Activation Volume

Table 4.5 summarizes the results of the tests using strain rate changes.

A remark to the $\mathbf{U}$ values at 400 °C: A negative volume makes physically no sense. In this special case, it means nothing more than the response of the material to a sudden increase in strain rate, $\Delta\dot{\varepsilon}$, is an abrupt decrease in the flow stress. The negative $\Delta\sigma$ gives rise to a negative $\mathbf{U}$. The extremely small negative $\mathbf{U}$ values indicate a high negative $\Delta\sigma$, about 5 % of the applied stress. At 400 °C, both changes in strain rate, by a factor of three or ten, induce the same drop in flow stress. At 500 °C, the small $\Delta\dot{\varepsilon}$ leads to the normal increase in σ and the large $\Delta\dot{\varepsilon}$ is followed by a negative response of the stress. Hence, for 450 °C and 500 °C all $\mathbf{U}$ values in table 4.5 are determined using strain rate changes by a factor of three. The representation of $\mathbf{U}$ as mean values with a standard deviation is not a complete description of the test data at each temperature. At low temperatures (-196 °C to RT), there is a dependence of $\mathbf{U}$ on the strain. The activation volumes determined by a series of strain rate changes on one sample of Al_5Ti_2Cr and Al_5Ti_2Mn, each at room temperature, as well as one Al_5Ti_2Fe (1^{St}) sample tested at 700 °C are shown in figure 4.12. According to section 3.3.3, $\mathbf{U}$ is plotted as a maximum and a minimum value and the corresponding average. In both tests carried out at RT, a decrease of $\mathbf{U}$ with increasing strain and stress is observed. For Al_5Ti_2Cr (figure 4.12a) the activation volume decrases from $\mathbf{U} \approx 270\ b^3$ to $\mathbf{U} \approx 150\ b^3$ and for Al_5Ti_2Mn (figure 4.12b) from $\mathbf{U} \approx 320\ b^3$ to $\mathbf{U} \approx 220\ b^3$. At this temperature, a first jump in strain rate directly after yielding leads to small $\mathbf{U}$ values. This is due to the region of low work hardening rate, ϑ, at the beginning of plastic deformation in the Cr and Mn modified trialuminides. The deformation mechanisms seem to be different from those at higher ε, where ϑ is almost constant. At high temperatures, $\mathbf{U}$ becomes essentially independent of σ and ε. As an example, the $\mathbf{U}$ data of Al_5Ti_2Fe (1^{St}) at 700 °C is presented in figure 4.12c. Over the whole range of strain (or stress), the data points scatter around $300\ b^3$.

	Temp [°C]	ε [%]	Activation Volume $[10^{-27}m^3]$	$[b^3]$
Al_5Ti_2Cr	23	0.8...9.3	4.1 ± 0.9	185.8 ± 41.1
	400	12.2	-0.824	-37.6
	450	6.7...13.0	13.8 ± 2.23	629.1 ± 101.5
	500	2.5...14.8	11.0 ± 1.71	500.8 ± 77.9
	550	2.5...16.5	12.0 ± 1.77	545.5 ± 80.8
	600	1.4...15.4	13.0 ± 1.44	593.5 ± 65.8
	650	1.2...17.0	10.4 ± 1.62	474.0 ± 73.9
	700	0.7...14.4	7.2 ± 0.84	327.9 ± 38.2
Al_5Ti_2Mn	-196	1.7...13.3	1.12 ± 0.29	51.1 ± 13.2
	-60	2.6...12.2	2.66 ± 0.48	121.4 ± 22.0
	23	1.7...14.0	5.1 ± 1.3	232.7 ± 59.0
	102	1.2...13.6	8.6 ± 3.52	392.1 ± 160.5
	200	2.0...14.1	13.8 ± 3.8	627.2 ± 173.5
	250	1.5...6.3	13.7 ± 1.7	624.9 ± 77.6
	400	9.9...14.0	-0.83 ± 0.06	-37.8 ± 2.6
	450	9.3...16.9	11.5 ± 2.6	524.1 ± 117.2
	500	3.5...13.4	11.3 ± 2.1	516.9 ± 97.0
	550	2.1...13.0	13.4 ± 2.0	612.1 ± 93.1
	600	1.3...13.7	10.5 ± 1.4	479.7 ± 63.1
	650	1.4...15.7	8.2 ± 0.9	374.5 ± 42.9
	700	1.6...17.3	7.9 ± 1.1	361.0 ± 48.5
Al_5Ti_2Fe (1st series)	-196	1.2...4.8	0.96 ± 0.17	43.7 ± 7.5
	-60	1.5...10.3	2.25 ± 0.34	102.7 ± 15.7
	23	0.8...7.4	3.9 ± 0.9	180.8 ± 41.7
	101	0.7...7.5	6.0 ± 1.2	273.9 ± 52.7
	200	0.8...5.0	9.6 ± 2.8	437.1 ± 125.9
	400	7.6...9.0	-0.67 ± 0.03	-30.6 ± 1.3
	450	5.6...8.3	7.0 ± 0.57	318.8 ± 26.0
	500	5.1...9.7	5.4 ± 0.5	246.4 ± 21.4
	550	2.1...8.4	6.1 ± 0.44	276.2 ± 20.2
	600	2.6...12.5	6.8 ± 0.8	300.5 ± 34.3
	650	1.9...13.2	6.3 ± 1.1	287.6 ± 50.8
	700	1.1...16.3	6.5 ± 0.7	297.5 ± 31.7

Table 4.5: Activation volume at different test temperatures. b is the Burgers vector of a $^1/_2$<110> partial (b = 0.28 nm). The column ε indicates the range of plastic deformation over which U is averaged.

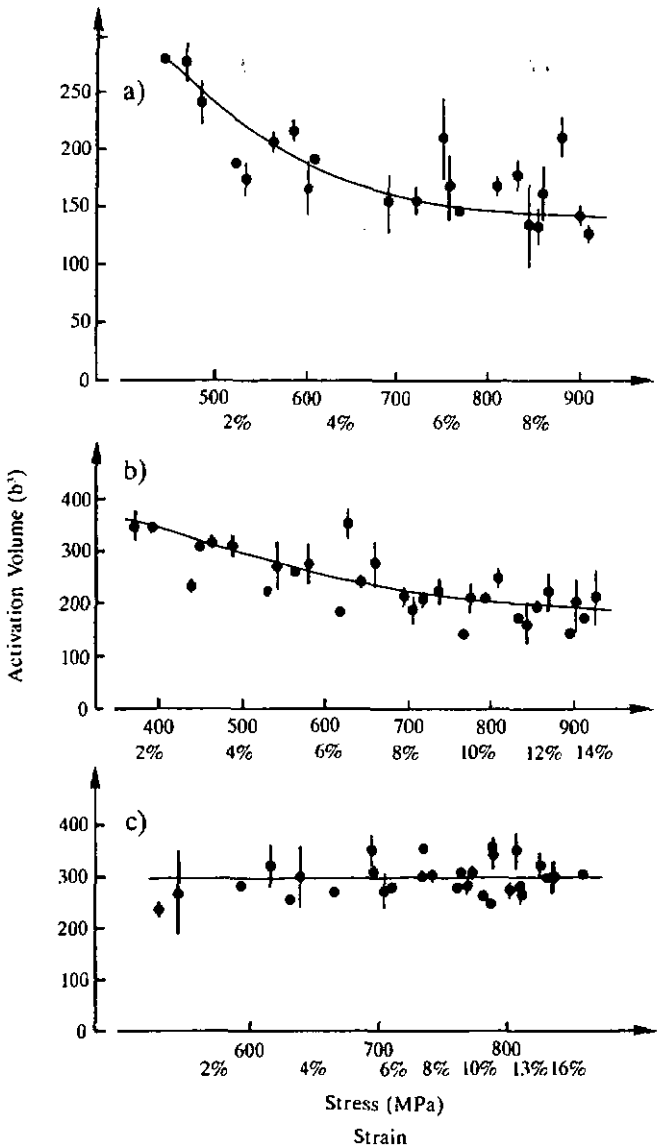

Figure 4.12: The activation volume as a function of the applied stress or actual strain ε (ε are approximate values). The scatter band represents the maximum and minimum U with the corresponding average of each change in strain rate (cf. section 3.3.3). a) Al_5Ti_2Cr at RT, b) Al_5Ti_2Mn at RT and c) Al_5Ti_2Fe (1^{st}) at 700 °C.

Figure 4.13 represents the influence of temperature on the activation volume of the three intermetallic phases.

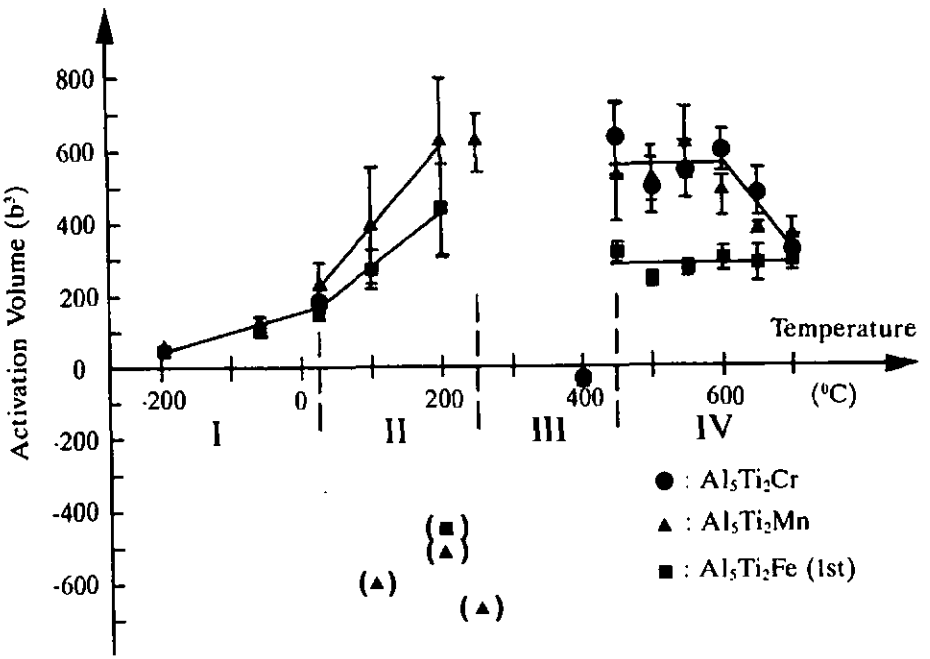

Figure 4.13: The activation volume as a function of temperature. The temperature axis is divided in four zones, I to IV, corresponding to different mechanisms controlling the deformation. The data points in brackets represent the negative activation volumes at high strains.

In zone I, between absolute zero and room temperature, U decreases continuously with decreasing temperature. This can be interpreted as the diminution of the thermal contribution to the flow stress. Considering the steadiness of this decrease, it is likely that at 0 K U will be smaller than 51 b^3 for Al_5Ti_2Mn and 44 b^3 for Al_5Ti_2Fe (1^{st}), respectively. Unfortunately, the data base is too uncertain and the scatter too important to establish a reliable extrapolation of U at 0 K. Dislocation dissociation and recombination can be excluded as deformation mechanism, because the activation volume for this mechanism is expected to be much greater than the values observed here (cf. section 2.3.2). For Shockley cross-slip the thermal activation is insufficient at the temperatures of zone I. The question if a Peierls' mechanism or solution hardening controls deformation at very low temperatures cannot be answered conclusively only on the

base of the activation volume, since the steady decrease of $\mathbf{U}$ with decreasing temperature and a value of $\mathbf{U} \approx 50\ b^3$ at -196 °C (> 0 K) fit the model of lattice friction as well as solution hardening. In the case of solution hardening, the concentration c is estimated as $4 \cdot 10^{-4} \leq c \leq 10^{-2}$, depending on x in eq. 2.13. This concentration range is expected to be shifted towards higher solute contents at 0 K, because at the same time $\mathbf{U}$ decreases.

Zone II, in the range of RT to about 250 °C, is characterized by a sharp increase of $\mathbf{U}$ with increasing temperature. Simultaneously, the first negative activation volumes are observed, at high strains and starting at 100 °C for Al_5Ti_2Mn and at 200 °C for Al_5Ti_2Fe (1^{st}). In this temperature range, the dynamic strain ageing (DSA) and the Portevin-LeChâtelier effect start, as described in section 4.2.2. The dislocations are locked by one of the mechanisms presented earlier. After a jump in the crosshead speed to a higher strain rate, the stress in the sample reaches rapidly the level at which the dislocations break away from their pinning points. This stress level is lower than the expected flow stress at the higher strain rate without DSA. The smaller $\Delta\sigma$ recorded alters the activation volume to larger values. If the softening of the material due to the unpinning of the dislocations is higher than the increase in stress up to the break away point, the resulting $\Delta\sigma$ is negative. Comprehensively, in zone II the flow stress is controlled by the onset of dislocation locking by the dynamic strain ageing mechanism.

In zone III, i.e. the approximate temperature range between 250 °C and 450 °C, the flow is characterized by the Portevin-LeChâtelier effect. Even in regions of homogeneous flow, before or after the serrations, each attempt to increase the strain rate initializes a new drop in stress. This negative strain rate sensitivity gives rise to a negative activation volume.

In zone IV, at temperatures higher than 450 °C, Al_5Ti_2Fe (1^{st}) behaves differently than the two others, Cr and Mn alloyed compounds. The latter exhibit a $\mathbf{U}$ in the range of 500 b^3 to 630 b^3 between 450 °C and 600 °C. At 700 °C, $\mathbf{U}$ drops to about 350 b^3. The Al_5Ti_2Fe (1^{st}) exhibits a rather constant activation volume of about 300 b^3 between 450 °C and 700 °C. A different behaviour of Al_5Ti_2Fe (1^{st}), on the one hand, and Al_5Ti_2Cr and Al_5Ti_2Mn on the other hand, is observed in the yield stress in the same temperature range (cf. figure 4.4). While the iron alloyed trialuminide shows anomalous strengthening above 500 °C, the two other materials have a rather constant yield stress at the temperatures of zone IV. At the same time an increase in the ductility in compression is observed at the same temperature as the drop of $\mathbf{U}$ for Al_5Ti_2Cr and Al_5Ti_2Mn occurs. A discussion of the relationships between the results of compression testing and the measured activation volume is presented in section 5.3.

4.2.6 Static Strain Ageing

For further investigation of the dynamic strain ageing and the Portevin-LeChâtelier effect, static strain ageing tests have been undertaken. For a given temperature T, the complete ageing time t_a (the time the cross head is stopped plus the time for reloading until yielding), the activation energy of strain ageing, Q_{SA}, may be determined as follows. The Q_{SA} are the apparent activation energies for the strain ageing process. They are related to diffusion but also to the mechanical loading. There is a dependence of the strengthening, $\Delta\sigma$, on the strain, ε, at which the ageing is accomplished (figure 4.14a) as well as on the stress applied during ageing, σ_a (figure 4.14b). Figure 4.14c, which illustrates the strengthening as a function of the ageing stress at two different strains, summarizes both dependences. The relationship between ε and $\Delta\sigma$ is almost linear. The data of one experiment, carrying out alternately ageings of 1 min and 20 min, is shown in figure 4.14a. Figure 4.14b depicts the data collected on several strain ageing tests at 250 °C during which ageing procedures of 30 min are performed. The stress during the strain ageing experiments was varied. Although the scatter due to the influence of strain is considerable, there is a tendency of higher $\Delta\sigma$ at higher ageing stress, σ_a.The steady increase of $\Delta\sigma$ with the ageing stress makes sense only if the internal stress σ_{int} corresponds almost to the flow stress. Under a shear stress $\tau = \tau_{int}$, dislocations do not move. Without an externally imposed deformation, dislocations creep likewise to the stress, if $\tau > \tau_{int}$, and opposed to the shear stress, if $\tau < \tau_{int}$. A stationary dislocation is trapped best by diffusing atoms. An internal stress close to the flow stress is not common but it can be verified by two different experiments.

First, assuming power law creep with an exponent of 4 and considering an internal stress, σ_{int}, such that the effective stress is $(\sigma - \sigma_{int})$. After Burt, Dennison and Wilshire [54] the strain rate $\dot{\varepsilon}$ can be expressed as

$$\dot{\varepsilon} = B(\sigma - \sigma_{int})^4 \tag{4.2}$$

where B is constant at a given temperature. Taking the two strain rates used to determine the activation volume, $\dot{\varepsilon}$ and $\eta\dot{\varepsilon}$, the internal stress σ_{int} is given by

$$\sigma_{int} = \frac{\sigma_1\sqrt[4]{\eta} - \sigma_2}{\sqrt[4]{\eta} - 1} \tag{4.3}$$

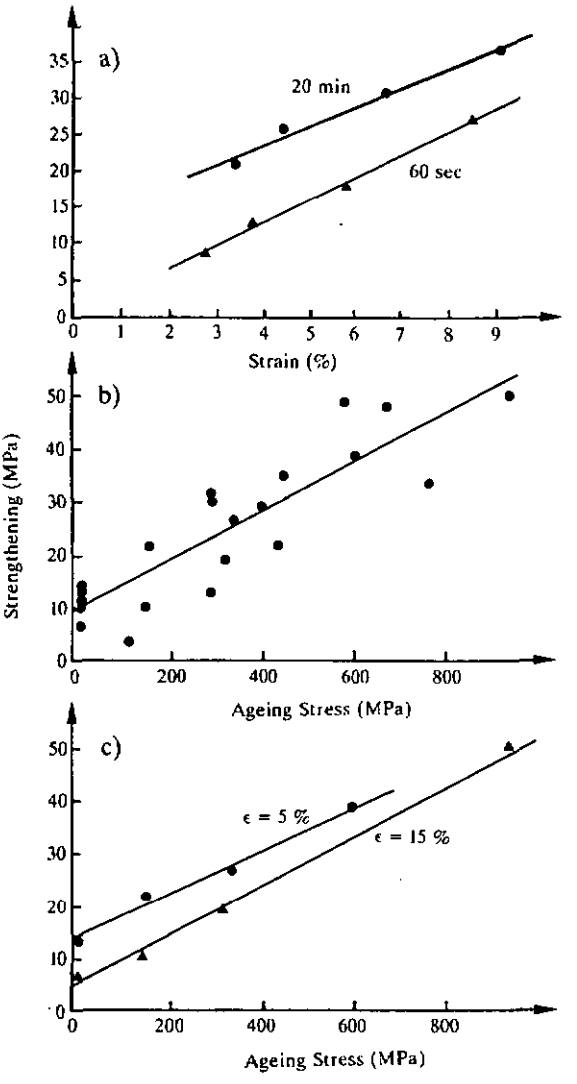

Figure 4.14: Results of strain ageing tests on Al_5Ti_2Mn at 250 °C. a) The influence of strain on the strengthening. Data of one test with ageing procedures at 400 MPa for 1 min and 20 min alternately. b) The influence of ageing stress on the strengthening. Data of several tests with ageing procedures of 30 min at different stress levels. c) Strengthening as a function of the applied ageing stress. Two ageing series of 30 minutes on the same sample at about 5 % and about 15 % strain are shown.

η is a positive number, σ_1 and σ_2 the flow stress at the lower and the higher strain rate, respectively. For Al_5Ti_2Mn at 250 °C, σ_{int} is calculated as $\sigma_{int} \approx 0.98 \cdot \sigma_2$ independent if $\eta = 3$ or $\eta = 10$ and constant with strain in the range of $1.5\ \% < \varepsilon < 5.8\ \%$.

Second, a stress relaxation test at 250 °C for the same material confirms the high value of σ_{int}. The test was accomplished by the incremental unloading method [55]. During this test the deformation is stopped and the sample unloaded by three to four steps. The response of the material directly after holding the cross head is recorded on every unloading increment. Afterwards the sample is reloaded, slightly deformed plastically and the unloading procedure is repeated aiming other stress steps for the relaxation. In total three unloading series are performed. A further decrease in load is defined as a negative relaxation velocity, v_{relax}. Analogously, an increase in load after stopping the machine corresponds to a positive v_{relax}. Figure 4.15 shows a plot of the relaxation velocity vs the stress at which the relaxation is carried out. The data points are interpolated by linear regression and σ_{int} determined as the intersection with the x axis, i.e. the stress at which the load remains constant during relaxation. With this method, the internal stress is determined as $\sigma_{int} = 0.92 \cdot \sigma$, where σ is the maximum flow stress reached before relaxation.

Figure 4.16 shows the evolution of the strengthening $\Delta\sigma$ with ageing time at three different temperatures.

It is seen that the saturation value of the strengthening, $\Delta\sigma_{sat}$, increases with increasing temperature. This is in agreement with the model of Friedel which predicts a finite time to saturate the dislocation with solute atoms [30]. He assumes that after a short time, all impurities at a distance r_0 have been drawn towards the dislocation. This radius of the depleted region is a function of the diffusion coefficient of the solutes. Therefore, the final solute concentration at the dislocation increases with increasing temperature [30], giving rise to a higher solute hardening effect and, at the same time, a higher saturation strengthening at higher temperature. As seen in figure 4.16, the effect of ageing on $\Delta\sigma$ is not the same for the three alloys. The smallest strengthening is observed in Al_5Ti_2Mn, figure 4.16b. $\Delta\sigma_{sat}$ in Al_5Ti_2Cr (figure 4.16a) and Al_5Ti_2Fe (1^{St}) (figure 4.16c) are similar but the latter reaches the same $\Delta\sigma_{sat}$ at a lower temperature. Figure 4.16c shows that at 225 °C, the saturation becomes unstable in Al_5Ti_2Fe (1^{St}), i.e. after a rapid increase of $\Delta\sigma$ with ageing time, $\Delta\sigma$ scatters around a maximum value. This maximum strengthening is lower than that reached at 200 °C. The same phenomenon, namely a decrease of the maximum strengthening together with an unstable saturation, is seen in the two other compounds, but at higher temperatures. This indicates that another process interacts at sufficiently high temperatures and sufficiently long ageing times. However, the

influence of this second process, possibly dislocation recovery, on $\Delta\sigma$ for ageing times in the range of waiting times during dynamic strain ageing, i.e. a few seconds, is negligible.

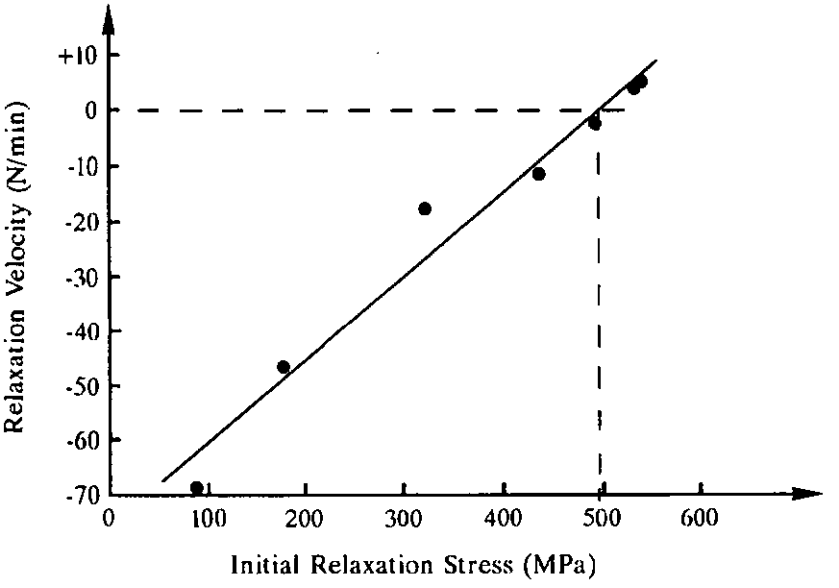

Figure 4.15: The results of a relaxations test for Al_5Ti_2Mn at 250 °C using the incremental unloading method [55]. Representation of the data as plot relaxation velocity vs stress at the beginning of the relaxation step.

The saturation value of strengthening for the three alloy under investigation are summarized in table 4.6. It is clearly seen that the maximum of strengthening varies from material to material and is observed at different temperatures in each material.

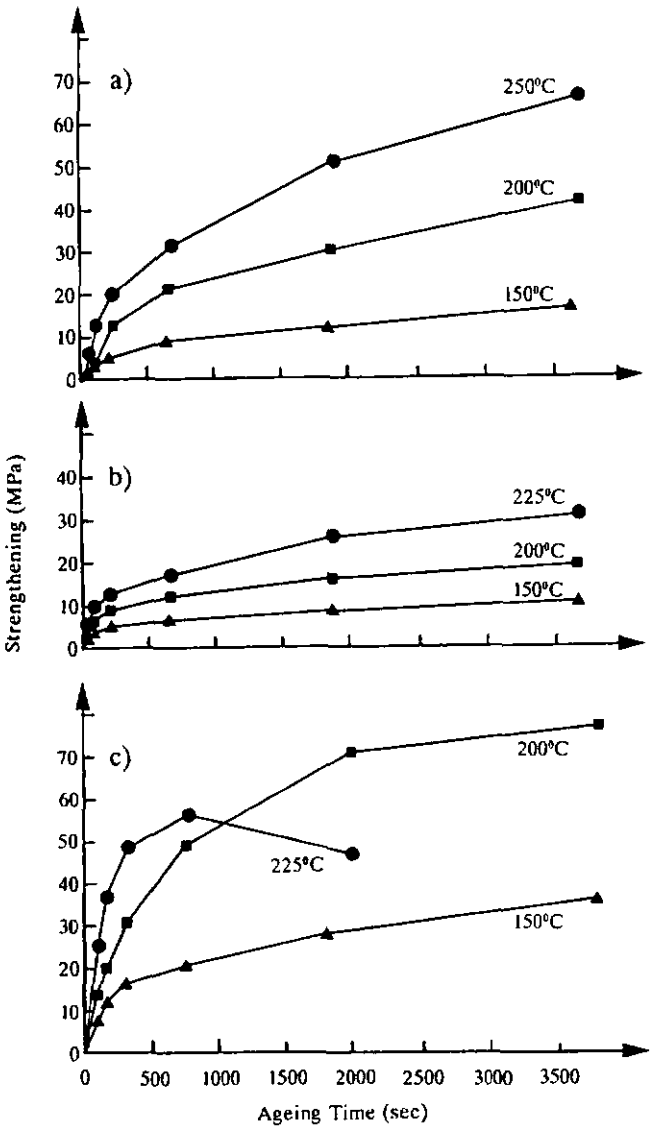

Figure 4.16: Strengthening $\Delta\sigma$ as a function of ageing time, t_a.

a) Al_5Ti_2Cr at 150 °C, 200 °C and 250 °C

b) Al_5Ti_2Mn at 150 °C, 200 °C and 225 °C

c) Al_5Ti_2Fe (1^{st}) at 150 °C, 200 °C and 225 °C (unstable saturation)

temperature [°C]	saturation strengthening [MPa]		
	Al_5Ti_2Cr	Al_5Ti_2Mn	Al_5Ti_2Fe
100	-	-	21.5
150	20.7	11.3	35.7
175	-	-	63.7
200	50.0	22.0	80.0
225	-	33.7	63.9
250	65.7	43.1	-
275	64.0	49.7	-
300	47.5	-	-

Table 4.6: Extrapolated saturation values of the strengthening measured during static strain ageing tests.

Figure 4.17 shows an example of the three graphs used to determine Q_{SA}. As discussed in section 2.3.2, the strengthening at a fixed time, $\Delta\sigma_f$, and the slopes of the plots $\ln(\Delta\sigma)$ vs $\ln(t_a)$ and $\ln(\Delta\sigma_f)$ vs T^{-1} are necessary to deduce the activation energy of strain ageing, Q_{SA}. Three different times are chosen to determine the corresponding $\Delta\sigma$ at each temperature, namely 125 sec ($\Delta\sigma_{125}$), 1000 sec ($\Delta\sigma_{1000}$) and the saturation strengthening ($\Delta\sigma_{sat}$). The latter is extrapolated by hand using the plot $\Delta\sigma$ vs t_a, figure 4.17a. Only if the saturation value remains stable, i.e. the model of the depleted cylinder around the dislocation presented above applies, $\Delta\sigma_{sat}$ is considered as valid for further calculations. The logarithmic plot $\ln(\Delta\sigma)$ vs $\ln(t_a)$, figure 4.17b, is used to determine $\Delta\sigma_{125}$ and $\Delta\sigma_{1000}$, as well as the slope n. The value of n used in eq 2.6 is the average of the slopes at all ageing temperatures. The other term required in eq 2.6, m_{Arr}, is the slope of the Arrhenius plot $\ln(\Delta\sigma_{sat})$ vs T^{-1}, figure 4.17 c to e. Figures 4.17 a to c show characteristic plots for the Al_5Ti_2Mn alloy. Figures 4.17d and 4.17e illustrate Arrhenius plots for the two other materials under investigation, namely $\ln(\Delta\sigma_{125})$ vs T^{-1} for Al_5Ti_2Cr and $\ln(\Delta\sigma_{1000})$ vs T^{-1} for Al_5Ti_2Fe (1^{st}).

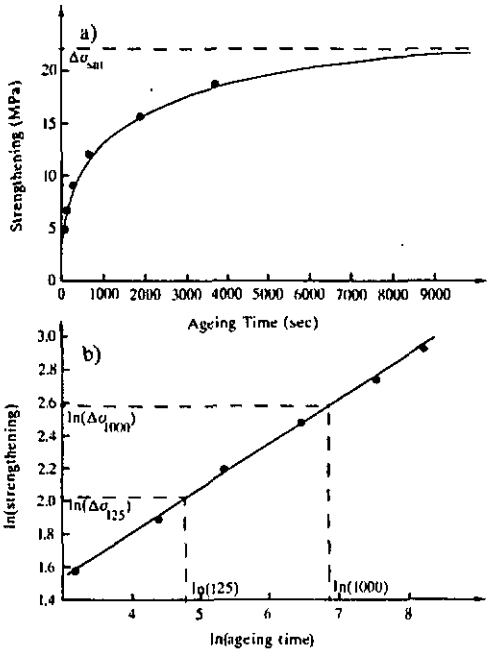
a)
$\Delta\sigma_{sat}$
Strengthening (MPa)
Ageing Time (sec)
b)
ln(strengthening)
$\ln(\Delta\sigma_{1000})$
$\ln(\Delta\sigma_{125})$
ln(125)
ln(1000)
ln(ageing time)

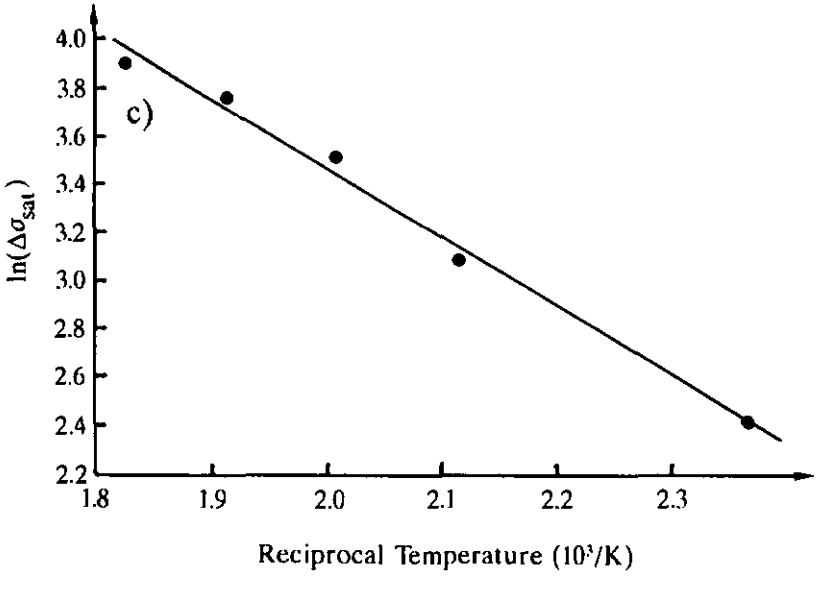
c)
$\ln(\Delta\sigma_{sat})$
Reciprocal Temperature (10^3/K)

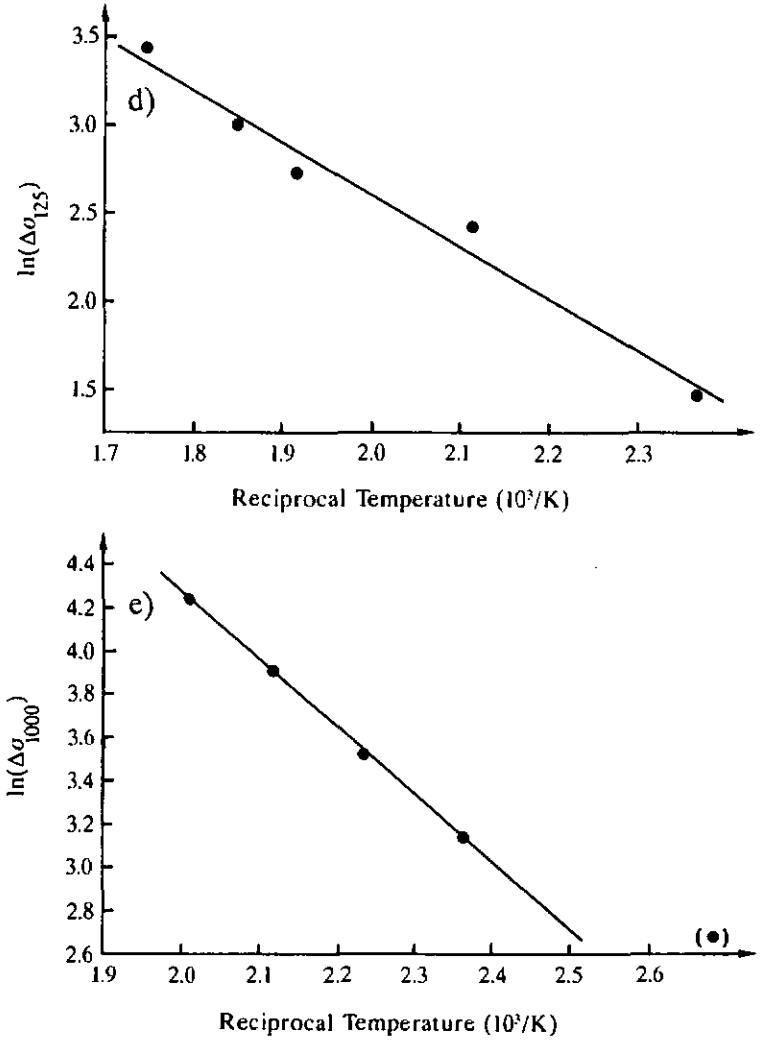

Figure 4.17: Examples of the three plots and the specific values for determination of the activation energy for strain ageing.

a) $\Delta\sigma$ vs t_a to determine $\Delta\sigma_{sat}$ by extrapolation for $t \rightarrow \infty$, Al_5Ti_2Mn, 200 °C.

b) $\ln(\Delta\sigma)$ vs $\ln(t_a)$ to determine the slope n as well as $\Delta\sigma_{125}$ and $\Delta\sigma_{1000}$, Al_5Ti_2Mn, 200 °C.

c) Arrhenius plot $\ln(\Delta\sigma_{sat})$ vs T^{-1} to determine the slope, m_{Arr}, Al_5Ti_2Mn.

d) Arhenius plot $\ln(\Delta\sigma_{125})$ vs T^{-1}, Al_5Ti_2Cr.

e) Arrhenius plot $\ln(\Delta\sigma_{1000})$ vs T^{-1}, Al_5Ti_2Fe (1^{st}).

Table 4.7 gives an overview of the activation energies for strain ageing. As seen in the second column, the slope, n, is not constant neither for the three alloys nor for the same alloy at the different ageing temperatures. A slight increase of n with increasing temperature is observed. Disregarding the influence of n, the activation energies are more similar (cf. section 5.4).

alloy	n	$Q_{SA}(\Delta\sigma_{125})$ [kJ/mol]	$Q_{SA}(\Delta\sigma_{1000})$ [kJ/mol]	$Q_{SA}(\Delta\sigma_{sat})$ [kJ/mol]
Al_5Ti_2Cr	0.390 ± 0.035	63	62	55
Al_5Ti_2Mn	0.308 ± 0.039	78	83	77
Al_5Ti_2Fe (1^{st})	0.403 ± 0.058	62	64	49

Table 4.7: The activation energies for strain ageing. n is the slope in the $\ln(\Delta\sigma)$ vs $\ln(t_a)$ plot. The symbols in brackets, $(\Delta\sigma_{125})$ $(\Delta\sigma_{1000})$ and $(\Delta\sigma_{sat})$ indicate how $\Delta\sigma$ was fixed to determine the values on the y-axis of the Arrhenius plot. The indices "125" and "1000" refer to time fixed at 125 seconds and 1000 seconds and "sat" means the saturation value of $\Delta\sigma$ for $t \rightarrow \infty$.

As stated at the beginning of this section, the strengthening due to strain ageing is a function of time, temperature, stress and strain. The first three parameters can be held constant while the latter varies in the range from about 2 % to about 6 %. This is a direct consequence of the test procedure using only one specimen per temperature to avoid scatter due to different samples. The influence of strain on the strengthening is documented in figure 4.14a for Al_5Ti_2Mn at 250 °C. Using the almost linear relationship between $\Delta\sigma$ and ε, the strengthening can be corrected to a value as if all strain ageing steps were done at the strain of the first 15 seconds ageing. These hypothetical, corrected values are compared to the measured strengthening in figure 4.18. As expected, increases the amount of correction towards longer ageing times, because these ageing steps are carried out at higher strains. This influence of strain has two consequences on the further calculations. First, $\Delta\sigma_f$ for the Arrhenius plot is altered to smaller values. This correction is more important for $\Delta\sigma$ fixed at long ageing times, especially for $\Delta\sigma_{sat}$. The second consequence is the reduction of n in the logarithmic plot $\Delta\sigma$ vs t. For Al_5Ti_2Mn at 250 °C (figure 4.18), the slope in this plot changes from n = 0.366 for $\Delta\sigma$ as measured to n = 0.302 for the corrected $\Delta\sigma$ values. This variation is not greater than the scatter of n over the temperature range investigated. A smaller n gives rise to higher activation energies while it is not sure if and at which amount the variation of $\Delta\sigma_f$ alters the slope of the Arrhenius plot. All in all, it seems likely that there is a mild dependence of Q_{SA} on ε. Hence the activation energies presented in table 4.7 are average values of the range of approximately 2 % to 6 % strain. Another analysis of the data of the strain ageing tests, which is independent of n, will be presented in section 4.3.3.

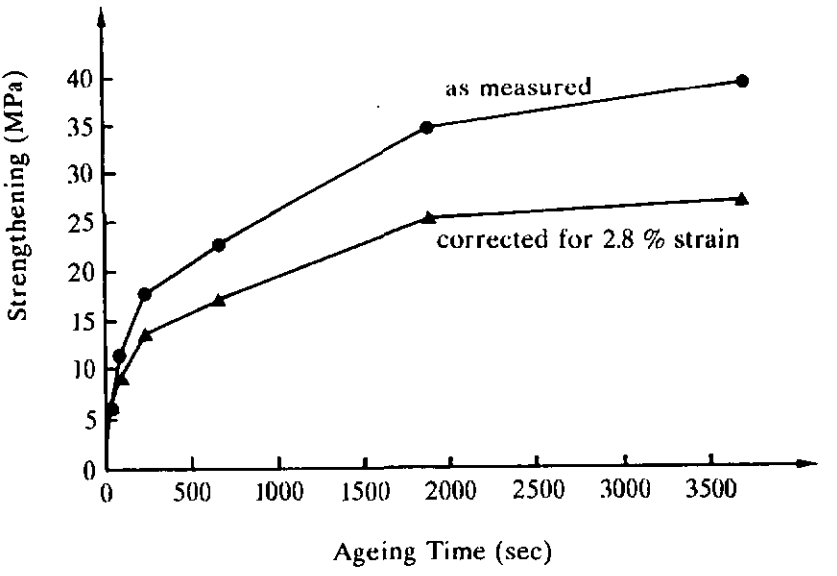

Figure 4.18: Strengthening as a function of ageing time for Al_5Ti_2Mn at 250 °C. The directly measured values of $\Delta\sigma$ are compared to $\Delta\sigma$ corrected for initial strain $\varepsilon = 2.8$ % using the linear relationship between $\Delta\sigma$ and ε in figure 4.14a.

The activation energies are low for an ordered alloy, compared for example to the self-diffusion of Ni in Ni_3Al with $Q = 270\ ^{kJ}/_{mol}$ [56] or of Ni in Ni_3Fe with $Q = 203\ ^{kJ}/_{mol}$ [38]. The small Q_{SA} indicates high diffusivity, as generally observed for the lattice diffusion of interstitial atoms. The amount of interstitials, like O, N and C, is not known. Considering the high Ti content and the gas atomization during preparation, O and N contamination cannot be completely avoided. As reported in [51], many small oxides and nitrides of aluminium are observed in Al_5Ti_2Fe (1^{st}). This indicates that the limit of solubility of these two interstitials is reached and that the lattice may be saturated with oxygen and/or nitrogen. No quantitative data on the solubility of O in Al_3Ti based intermetallics are available. Potez, Lapasset and Kubin presume that it is smaller than 210 ppm in Al_5Ti_2Cu [57]. On the other hand, titanium is known to solve about 33 at.% of O at temperatures $T \geq 600$ °C [10], while the solubility of O in Al is about $3 \cdot 10^{-8}$ at the melting point [10]. For TiAl, Kawabata, Abumiya and Izumi report a solubility of oxygen higher than 0.89 at.% at exact stoichiometry and "nearly zero" for a

compound with 56 at.% Al [58]. This suggests that the solubility limit of oxygen in Al_3Ti based alloys may be high compared to Al but still orders of magnitude smaller than in Ti rich Ti-Al alloys.

The occurrence of DSA in Ti in the same temperature range is usually attributed to the presence of interstitial oxygen. For the pinning and break away of the dislocations in the present materials, segregation of O seems less likely because of the completely different solublility of this interstitital. Other possible reasons, namely the relaxation of the antiphase boundary (APB) spread between the superpartials must be kept in mind. Such a mechanism is also governed by diffusion and there is at least one known model to describe the time dependence of the strengthening due to APB relaxation. This time law is different from that proposed here for the strain ageing by a "Cottrell atmosphere". A detailed discussion of APB relaxation will be presented together with the TEM observations in section 4.3.3.

4.3 Transmission Electron Microscopy

4.3.1 Dislocation Analysis

A detailed dislocation analysis of the Al_5Ti_2Fe (1^{st}) material is reported in [51].

First, the dislocation configuration in the as-received state, i.e. spray deposited and HIPped, is considered. There is a difference between Al_5Ti_2Fe (1^{st}) and the two Cr and Mn alloyed compounds concerning their dislocation densities. While in the latter, dislocations are observed only occasionally and usually bound to particles, the dislocation density in Al_5Ti_2Fe (1^{st}) is much higher. There are dislocations, often connecting the particles, cf. figure 4.4. When imaged under certain diffraction conditions the dislocations show fringe contrast. The Burgers vectors are <100> for the most part of the dislocations. They are in edge orientation and lie along <011> directions. There is no evidence of dissociation. The fringe contrast can be characterized by a fault vector parallel to <001> in such a way that the faults can be rendered invisible by the suitable choice of the diffraction vector g. These faults appear to lie on {011} planes, similar to disk-like Al_2Ti particles, seen attached to some of the dislocations. As such, the likely interpretation of these fringes seems to be solute segregation or incipient precipitation on the <100> dislocations during HIP.

Summarizing the dislocation configuration after deformation of about 1 % at three different temperatures, it is seen that the dislocations created by deformation are uniformly distributed. After deformation of Al_5Ti_2Fe (1^{st}) at RT, they are mostly undissociated at the resolution of weak beam electron microscopy and have Burgers vectors of b = <110> [51]. Although, dislocations very close to each other are observed, imaging with $+g$ and $-g$ reveals them as dislocation dipoles. For both, the dipoles and the single dislocations, straight as well as smoothly curved segments are seen. Depending on the foil orientation, a dislocation may appear alternately straight or slightly curved. These dislocations lie on {111} planes and are mobile on those octahedral planes. They are generally of the edge type, lying in 60° - 90° directions.

After straining Al_5Ti_2Fe (1^{st}) 1 % at 500 °C, the dislocations exhibit no clear alignment in any particular direction. Dipoles are still present but less than in the sample deformed at RT. Examination under weak beam conditions show that the majority of the dislocations are dissociated as a pair of $^1/_2$<110> dislocations, with an APB in between. The spacing of the partial dislocations is measured to be d ≈ 7 nm [51]. Analyzing the glide planes showed that they are of the {111} type as at RT. There seems to be no cross-slip of superdislocations onto {010} planes, at least no dislocations on cube planes are observed.

The most important change in dislocation configuration is observed after deformation at 700 °C. Essentially all the dislocations are now dissociated as a pair of $^1/_2$<110> superdislocations. A large number of them lies on {111} and at the same time on the corresponding {010} cross-slip plane. The smooth curvature of the superdislocations on both planes indicate good mobility on octahedral as well as cube planes. The spacing of the superdislocations on {010} is about d ≈ 22 nm, the separation of the superpartials of dislocations on {111} is d ≈ 16 nm.

In summary in Al_5Ti_2Fe (1^{st}), the dislocation configurations are characterized by first the spacing of the superdislocations, which increases with increasing temperature, and second the cross-slip of superdislocations from their {111} low temperature glide plane to their {010} high temperature glide plane. At RT, the superdislocations are occasionally dissociated at a degree just resolved under weak beam conditions, i.e. d ≈ 2.7 nm. As reported by Morris, samples deformed in liquid nitrogen exhibit dislocation configurations similar to those deformed at RT, namely dissociated (2 nm ≤ d ≤ 3 nm) as well as undissociated dislocations are seen [59]. On the same occasion, he observes that the dissociation distance increases slightly with increasing deformation. This suggests that mobile dislocations are dissociated, even at very low temperatures. Hence, it is justified to take the small Burgers vector, $^a/_2$<110>, to determine the activation volume at the temperatures of zone I (cf. figure 4.13).

After deformation at 500 °C, the majority of the dislocations are dissociated into two $^1/_2$<110> partials mobile on octahedral planes. The undissociated segments show a strong intensity contrast, stronger than that observed in samples deformed at RT [51]. This intense contrast indicates a locally high distortion of the lattice around the dislocation core. Further discussion of this subject will be presented in section 4.3.3. Classical Kear-Wilsdorf locks, manifested by long straight screw dislocations are not observed. While no dislocation on {010} plane is seen, there is evidence of cross-slip of superdislocations between octahedral planes. The precise temperature of the onset of {111} to {010} cross-slip remains unclear. There is no sign of it at 500 °C, and at 700 °C, almost half of the superdislocations lie on the cube cross-slip planes. Independent of the cross-slip plane, if the partials of the superdislocations are further dissociated into Shockley partials the latter have to constrict for cross-slip. In section 4.2.4, Shockley cross-slip is postulated as the mechanism controlling the flow stress. The actual TEM observations confirm this idea although there is neither direct evidence of the Shockley partials nor of their constriction.

After deformation at 700 °C the dislocations are separated but the spacing of their superpartials depend upon the plane on which they lie. Assuming isotropic elasticity, the APB energy γ can be calculated for screw dislocations as

$$\gamma = \frac{\mu b^2}{2\pi d} \tag{4.4}$$

where μ is the shear modulus (μ = 84 GPa [60]), b the Burgers vector and d the spacing of the superdislocations. The APB energy on {111} is deduced as γ_{111} = 72 mJ/m^2 and on {010} as γ_{010} = 45 mJ/m^2, giving rise to the ratio $\gamma_{111}/\gamma_{010}$ = 1.6. This anisotropy of the APB energy can be seen as a driving force for cross-slip of the superdislocations onto the cube planes. The ratio $\gamma_{111}/\gamma_{010}$ = 1.6 is somewhat smaller than the value of $\sqrt{3}$ postulated by the Paidar, Pope and Vitek (PPV) model [45] but it is also possible that elastic anisotropy plays a role in assisting the cross-slip process. Yoo completes the PPV equation by an anisotropy term [61]

$$(1 + f_1\sqrt{2})\frac{\gamma_{111}}{\gamma_{010}} > \sqrt{3} \tag{4.5}$$

where f_1 is an anisotropic factor due to the tangential component of the elastic interaction between two superpartials along scew orientation. f_1 is of comparable magnitude to the radial component, considered by the PPV model, e.g. f_1 = 0.62 for Ni_3Al [61]. It is seen that for Al_5Ti_2Fe even a small anisotropic contribution is sufficient to fulfill the Paidar-Pope-Vitek criterion modified by Yoo. Consistent with the present TEM observations, the increasing yield stress in Al_5Ti_2Fe (1st) at test temperatures of 500 °C and above can be interpreted by pinning effects caused by the cross-slip of superdislocations onto {010} planes.

The dislocations configuration observed in Al_5Ti_2Cr and Al_5Ti_2Mn are very similar and not really different from that in Al_5Ti_2Fe (1st). The TEM investigations on Al_5Ti_2Mn reported in the following will be given as an example. Essentially, the observations on Al_5Ti_2Mn are also valid for Al_5Ti_2Cr.

After 2 % deformation at room temperature the dislocations in Al_5Ti_2Mn have a slight tendency of arranging around particles. As shown in figure 4.19, several straight screw dislocations, parallel to each other, are observed. They lie along the <011> direction and they are marked with small arrows. Such screw segments may play an important role, as will be discussed in section 4.3.3. A few dipoles are seen in figure 4.19, marked with the letter "D". Compared to Al_5Ti_2Fe (1st), the dipole density is relatively low. Examined at higher magnification, some dislocations seem to be dissociated. Weak beam investigations confirm that essentially all dislocations are separated by an APB [59]. Dissociation takes place to a pair of $^1/_2$<110> dislocation partials lying on the {111} plane. The spacing of the two superpartials is about d ≈ 5 nm. The curvature of the dislocations other than those in screw orientation indicate their mobility on octahedral planes.

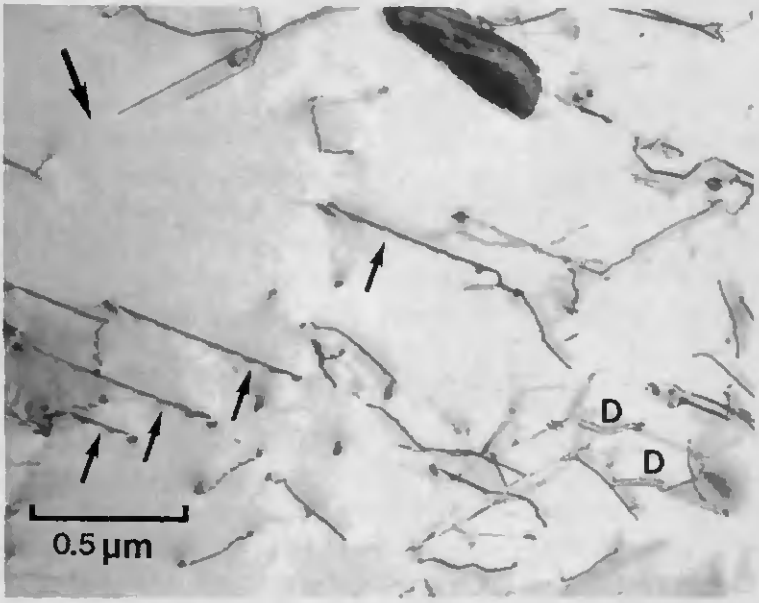

Figure 4.19: TEM micrograph of Al_5Ti_2Mn after 2 % deformation at RT. Foil orientation (001), diffracting vector $0\bar{2}0$. Small arrows indicate straight segments of screw <110> superdislocation, the letter "D" marks dipoles.

Figure 4.20 depicts some dislocations in Al_5Ti_2Mn after 2 % deformation at 500 °C. No long straight dislocation segments are seen any more. They are rather smoothly curved. The dissociation of many superdislocations into two $^1/_2$<110> partials is clearly seen. The separation distance of the pair of superpartials is determined as d ≈ 20 nm.

In Al_5Ti_2Cr, Al_5Ti_2Mn and Al_5Ti_2Fe (1^{st}) and at all deformation temperatures investigated, the two superpartials are separated by an APB. On the one hand, this is shown by contrast analysis of weak beam micrographs performed by Morris [59] on the other hand, the absence of an unusual increase of the yield strength at cryogenic temperatures of these compounds supports the hypothesis of dislocation dissociation creating an APB.

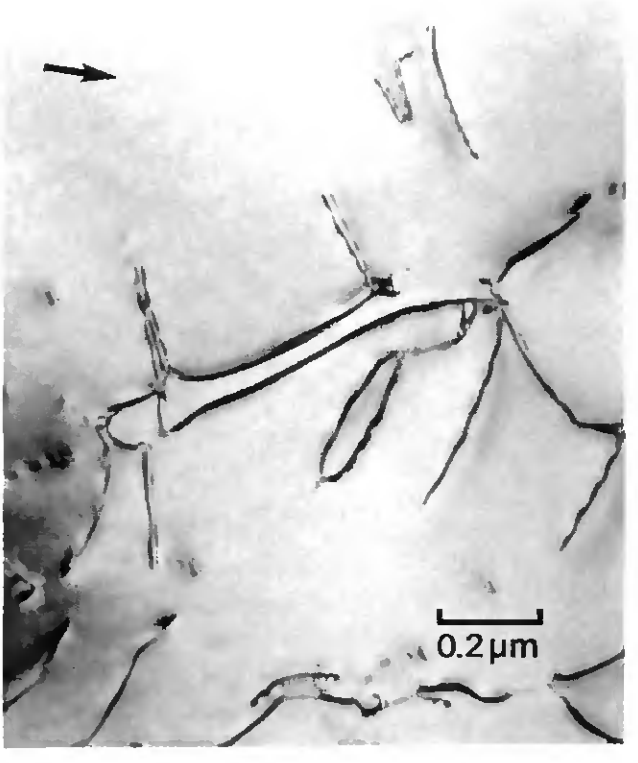

Figure 4.20: TEM micrograph of Al_5Ti_2Mn deformed 2 % at 500 °C. Foil orientation (112), diffracting vector $\overline{1}11$. Many superdislocations are clearly dissociated.

The present dislocation analysis reveal the following common features of the Cr, Mn and Fe (1^{st} series) alloyed trialuminides:

1) Mobile dislocations are mostly dissociated into a pair of $^1/_2$<110> superpartials.

2) The superpartials are separated by an APB.

3) At room temperature the superdislocations glide on {111} planes. At 700 °C, cross-slip from {111} to {010} becomes possible.

The differences between Al_5Ti_2Fe (1^{st}) on the one hand and Al_5Ti_2Cr and Al_5Ti_2Mn on the other hand are:

1) In Al_5Ti_2Fe, the separation distance is smaller and it is more difficult to achieve dissociation. A higher strain is necessary for dissociation to take place [59].

2) In Al_5Ti_2Fe, the density of dipoles is considerably higher.

3) In Al_5Ti_2Fe, no groups of straight, parallel screw segments are observed.

The most important difference is the dissociation distance. It can be concluded that Al_5Ti_2Cr and Al_5Ti_2Mn lattices are more suitable for dislocation dissociation. This is responsible for an easier onset of the dislocation movement and for a better ability of the dislocation to remain mobile, which can be explained by macroscopic observations, i.e. a lower yield stress and, together with the smaller amount of dipoles, a lower hardening rate. Considering the conclusions of section 4.2.2, the consequence is an enhanced ductility of the material.

4.3.2 Dislocation Density

The evolution of the dislocation density is treated qualitatively by means of the alloy Al_5Ti_2Mn. Figure 4.21 depicts dislocations in samples deformed to different strains at room temperature, namely a) 0.7 %, b) 2 % and c) 5 %. The undeformed state is not shown because in such foils dislocations are found only occasionally. In figure 4.21a, dislocations in the vicinity of a second phase particle are seen. At this strain, the concentration of dislocations is generally higher at particles than in the same grain far away from second phases. Considering the effectively modest number of dislocations, this collection of dislocations at particles at such low strains has no significance on the dislocation arrangement after severe plastic deformation. Since three different <110> Burgers vectors are observed in this micrograph (dislocations with one of these *b* are invisible actually), there seems to be a preference of only a few slip systems at low strains. Long straight screw segments are not seen yet. It should be kept in mind that at 0.7 % deformation, Al_5Ti_2Mn is in a zone of low work hardening rate, the already mentioned shoulder after yielding.

Figure 4.21b shows that at 2 % strain the dislocation density within one grain at a particle and away from it is almost equalized. A tendency for concentration of dislocations at grain boundaries is sometimes observed. Not all dislocations are analyzed concerning their Burgers vectors but there are considerably more than three different orientations, indicating an increasing number of dislocation sources and slip systems with increasing strain. Long straight screw segments are present. Analogous to such dislocations observed in Cu_3Al [39] and Ni_3Al [40], these segments are thought to be relatively immobile. They give rise to a large amount of work hardening. Interaction of these screw segments with other mobile dislocations is not seen.

Figure 4.21c illustrates the dislocation arrangement after 5 % straining. The dislocations are grouped in agglomerates, presumably pre-states of cell walls, seen at grain boundaries (upper left corner) and particles as well as in the "free" space within the grains. These dislocation agglomerates are not linear pile-ups but rather arbitrary collections of dislocations. The dislocation density in these agglomerates is so high that it renders difficult the separation of one single dislocation or one dislocation interaction. Hence, no Burgers vectors are determined. Occasionally, long straight segments in distinct directions are observed. But the amount of these dislocation locks does not increase at the same level as the other dislocations do.

No groups of screw segments are observed at low strains. This suggests that the yield stress is not affected by the formation of such dislocation pinning but the flow stress after the shoulder in the stress-strain curve is influenced. The observation that there is neither exclusive nor extensive pile up of dislocations at grain boundaries or particles is consistent with the findings of the fracture surface investigations. Particles and grain boundaries are present on fracture surfaces but the main fracture mechanism is transgranular cleavage. It is likely that the "weakest point" in this compound is the low cleavage strength. Hence, a sufficient pile-up of dislocations separates atomic planes, independent of the exact microstructural site of this stress concentration.

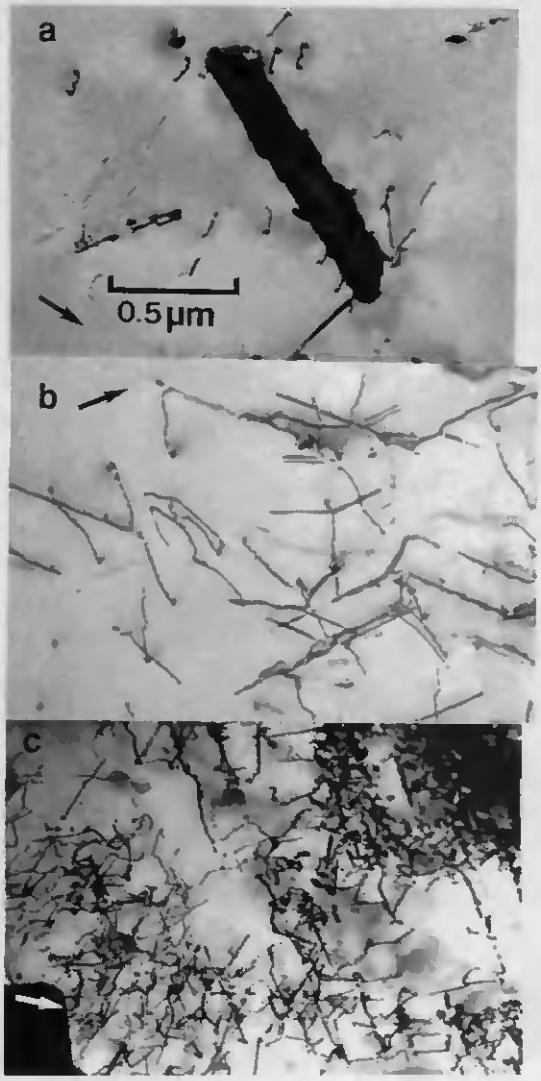

Figure 4.21: TEM micrographs of Al_5Ti_2Mn deformed to different strains at RT: a) 0.7 %, collection of dislocations at a particle, foil orientation (001), diffracting vector $\bar{2}00$. b) 2 %, no pronounced dislocation concentration, but straight screw segments, foil orientation (001), diffracting vector $\bar{2}00$. c) 5 %, agglomerates of dislocations at grain boundaries (upper right corner) and within the grain, foil orientation (011), diffracting vector $\overline{1}11$

4.3.3 Antiphase Boundary Relaxation

An important observation concerning the dissociation width of the superdislocations is reported in detail by Morris [62, 63]. In situ TEM examinations are used to investigate the influence of annealing on dislocations in deformed Al_5Ti_2Fe (1^{st}). The separation of the partials constituting the superdislocation increases rapidly in a non-recoverable manner during annealing. After straining 4 % at RT some dislocations are just detectably dissociated by weak beam microscopy. After annealing 5 min at 500 °C, most dislocations exhibit a distinct dissociation of about $d \approx 7$ nm. After annealing at 700 °C, all dislocations are dissociated.

The changes described above take place very rapidly. At 200 °C, an apparent increase of d is noted after about 5 min, at 400 °C, an equilibrium dissociation is reached after about 3 min only. The effect is not reversible. On cooling, the separation width remains at the dimension obtained during annealing. Table 4.8 summarizes the dissociation distances at equilibrium.

	Al_5Ti_2Mn	Al_5Ti_2Fe (1^{st})	Al_5Ti_2Fe (1^{st}) annealed	
temperature [°C]	deformed d [nm]	deformed d [nm]	screw d [nm]	edge d [nm]
23	5.0	2.7	-	-
200	-	-	3.0	3.5
300	-	-	4.0	4.3
400	-	-	4.0	5.3
500	20	7.0	5.0	6.9
700 {111}	-	16	25	25
{010}	-	22	-	-

Table 4.8: Dissociation distance of superdislocations after deformation at different temperatures ("deformed") or deformed at RT and annealed afterwards at different temperatures ("annealed"). Later values are taken from ref. [63].

The experimental evidence of the increasing separation width of stationary superdislocations at intermediate and high temperatures is in good agreement with the previously reported increasing saturation strengthening, $\Delta\sigma_{sat}$, in strain ageing tests. Over a certain temperature range, $\Delta\sigma_{sat}$ depends directly on the diffusion coefficient of the solutes (section 4.2.6). In the present chapter, it is assumed first of all that the strengthening observed in the static strain ageing experiments is due to APB relaxation. The increasing equilibrium dissociation width of the superpartials with increasing temperature is taken as a measure for the pinning effect. The following

analysis is based on the fact that the equilibrium energy of the APB ribbon enclosed by the superdislocations depends on temperature.

A model for dislocation pinning by APB relaxation is proposed. Like in the work of van den Beukel [28], dislocation movement is considered as characterized by alternately waiting in front of an obstacle and running through the lattice until the dislocation meets the next impediment. The obstacle can be surmounted with the help of thermal and/or mechanical activation. In a superlattice, the dissociation distance of the superdislocation may increase during this waiting time, t_w, at obstacles. The change in separation width reported before is rapid enough to affect dislocations in the temperature range of the Portevin-LeChâtelier effect, i.e. from about 200 °C to 600 °C. While direct in-situ TEM measurements of the evolution of the separation width d are not available, the effect of the APB relaxation can be related to the flow stress. According to Brown [33], there is a linear relationship between the increase in flow stress, $\Delta\sigma$, and the decrease in APB energy, $\Delta\gamma$

$$\Delta\sigma \sim \Delta\gamma \tag{2.7}$$

Using this linear dependence, the classical relaxation kinetic, model A after Schoeck and Korner [38], is adapted to the present case (cf. section 2.3.3). The rate at which the APB energy, γ, changes is assumed to be proportional to the deviation from its equilibrium energy $\bar{\gamma}$

$$\frac{d\gamma}{dt} = - k_r(\gamma - \bar{\gamma}) \tag{2.8}$$

where k_r is the rate constant and $\bar{\gamma}$ is constant at a given temperature. Integration gives

$$\gamma - \bar{\gamma} = (\gamma_0 - \bar{\gamma}) \exp(-k_r t) \tag{4.6}$$

where γ_0 is the APB energy at the time t = 0, i.e. the energy of the APB ribbon produced by shear. Defining $\Delta\gamma$ as $\Delta\gamma := (\gamma_0 - \gamma)$ and $\Delta\gamma_{sat} := (\gamma_0 - \bar{\gamma})$ and using the linear relationship between $\Delta\sigma$ and $\Delta\gamma$ eq. 4.6 yields

$$\Delta\sigma_{sat} - \Delta\sigma = \Delta\sigma_{sat} \exp(-k_r t)$$

or, by taking the natural logarithm

$$\ln\left(1 - \frac{\Delta\sigma}{\Delta\sigma_{sat}}\right) = - k_r t \tag{4.7}$$

The rate constant k_r can be determined by a plot of the left hand side of eq. 4.7 vs t. k_r represents the slope of the straight line fitting the data points using linear regression. By plotting $\ln(k_r)$ vs T^{-1}, a so called Arrhenius diagram, the activation energy of APB relaxation Q_{APB} can be deduced as

$$Q_{APB} = m_{Arr}R \qquad (4.8)$$

where m_{Arr} is the slope in of the line through the data points in the Arrhenius plot.

The term on the left hand side of eq. 4.7 varies sensitively for values of $\Delta\sigma/\Delta\sigma_{sat}$ close to 1. While $\Delta\sigma$ can be measured precisely, $\Delta\sigma_{sat}$ is an extrapolated value. To avoid significant deviations because of the uncertainty of $\Delta\sigma_{sat}$, the strain ageing tests with the longest ageing time, where $\Delta\sigma$ approaches $\Delta\sigma_{sat}$, are not taken into consideration for the determination of k_r.

As shown in figure 4.22, the graphical representation of eq. 4.7, the data for Al_5Ti_2Cr (figure 4.22a), Al_5Ti_2Mn (figure 4.22b) and Al_5Ti_2Fe (1^{st}) (figure 4.22c) can be fitted reasonably well by a straight line, perhaps with exception of the data points at lowest temperatures and shortest ageing times. Plotting the natural logarithm of the slope of the lines in figure 4.22 against T^{-1}, it is seen in figure 4.23 that for all three alloys (figure 4.23a: Al_5Ti_2Cr, 4.23b: Al_5Ti_2Mn and 4.23c: Al_5Ti_2Fe (1^{st})) only the data points at the three highest temperatures can be approached relatively well by a straight line. This indicates that this classical relaxation model is too simple to apply to all temperatures where strain ageing occurs. The kinetic model discussed in section 4.2.6 (solute segregation) seems to be the better approach for the present phenomenon. Nevertheless, activation energies of APB relaxation, Q_{APB}, are deduced using only the data points at the three highest temperatures in figure 4.23. Table 4.9 summarizes the activation energies, determined using figures 4.22 and 4.23 and compares them to the average values of the activation energies of strain ageing, cf. section 4.2.6.

activation energy	Al_5Ti_2Cr	Al_5Ti_2Mn	Al_5Ti_2Fe (1^{st})
Q_{APB} [kJmol^{-1}]	62	29	56
Q_{SA} [kJmol^{-1}]	60	79	58

Table 4.9: The activation energies for APB relaxation, Q_{APB}, compared to the average values of activation energies for strain ageing, Q_{SA}.

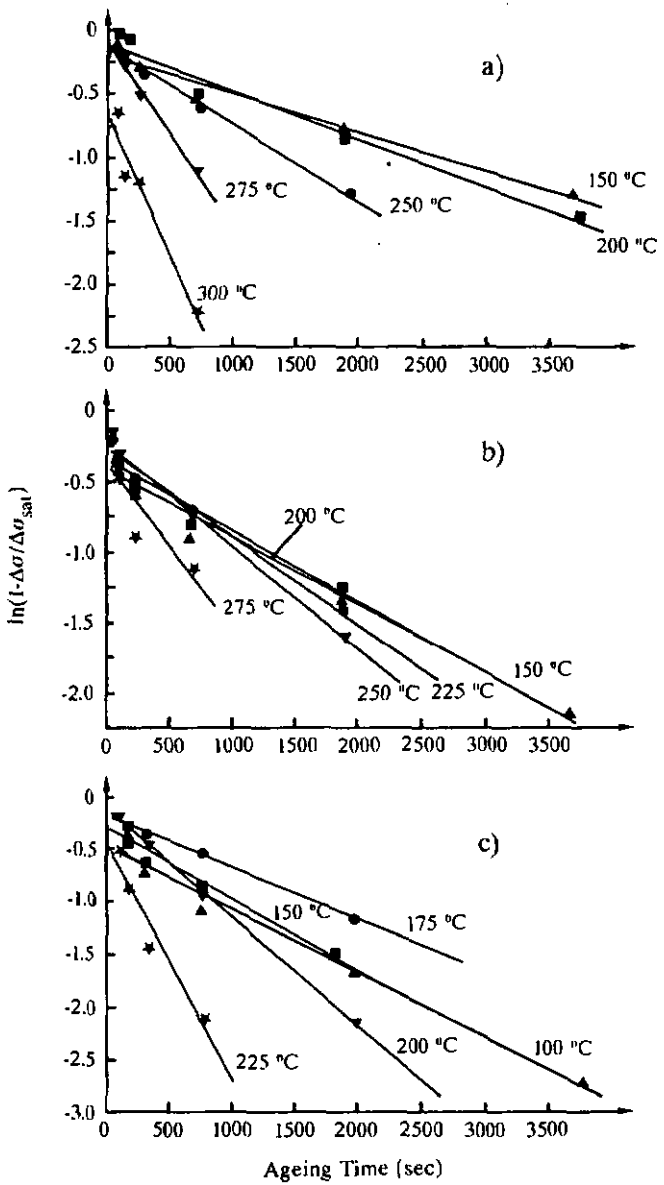

Figure 4.22: $\ln\left(1 - \frac{\Delta\sigma}{\Delta\sigma_{sat}}\right)$ as a function of ageing time. a) Al_5Ti_2Cr, b) Al_5Ti_2Mn and c) Al_5Ti_2Fe (1^{St}).

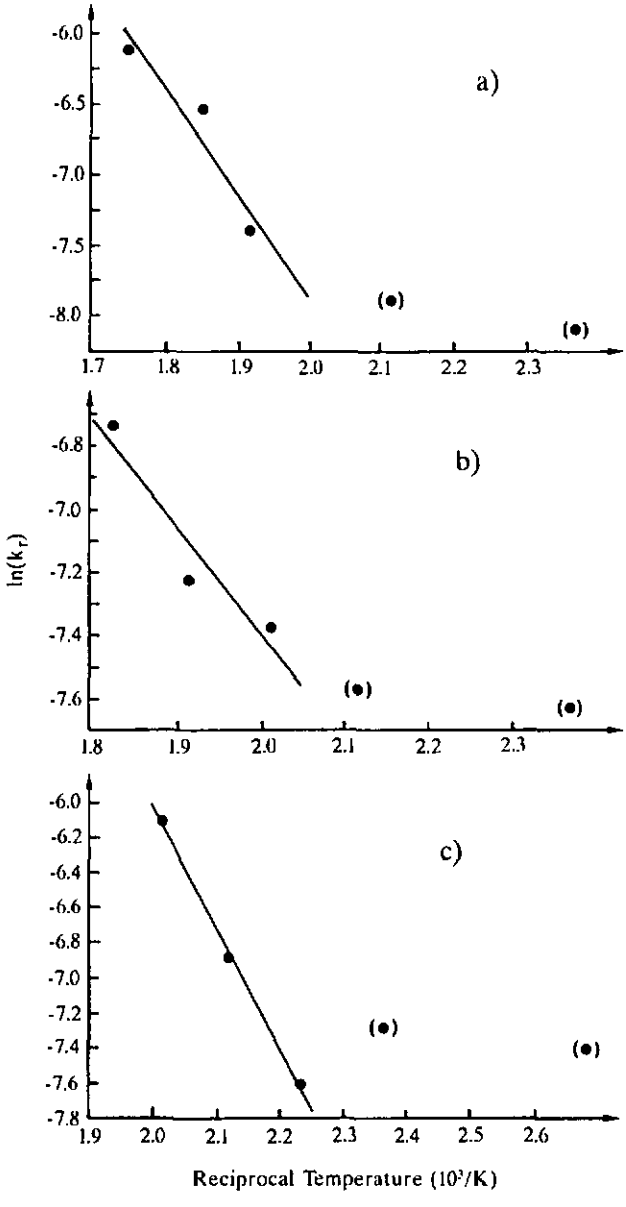

Figure 4.23: Arrhenius plot showing k_r as a function of T^{-1}. k_r is the slope of the curves in figure 4.22. a) Al_5Ti_2Cr, b) Al_5Ti_2Mn and c) Al_5Ti_2Fe (1^{st}).

For Al_5Ti_2Cr and Al_5Ti_2Fe (1^{st}) the agreement of Q_{APB} and Q_{SA} is good, but for Al_5Ti_2Mn Q_{APB} is much lower than Q_{SA}. Bearing in mind that the data points in figure 4.24 represent rather a hyperbolic curve than a straight line, it seems that APB relaxation is the dominant strengthening mechanism only in a small temperature range. While Al_5Ti_2Cr and Al_5Ti_2Fe (1^{st}) exhibit unstable saturation at the highest temperature used for strain ageing tests (i.e. 300 °C and 225 °C, respectively), Al_5Ti_2Mn does not at 275 °C, the highest temperature investigated in this compound. Hence, the temperature range examined for Al_5Ti_2Mn is lower relative to Al_5Ti_2Cr and Al_5Ti_2Fe (1^{st}). Taking only the data points at the two highest temperatures for Al_5Ti_2Mn, the actviation energy is determined as $Q_{APB} \approx 50$ kJmol^{-1}. It is seen that the value of the activation energy depends on the temperatures range where it is determined. The upper limit of this temperature range should be the temperature where the saturation becomes unstable. This prerequisite is not fulfilled in the case of Al_5Ti_2Mn. However, this stray value of Q_{APB} for this material is believed to have no relevance on the general interpretation of Q_{APB} as well as Q_{SA}.

Although only three temperatures are taken into consideration and the simplest model for APB relaxation is chosen, this analysis confirms the low values of the activation energies. In the case of segregation of solute atoms to the dislocation, Q_{SA}, the driving force is the difference in interaction energy of the solute in the lattice to the solute near the dislocation core. This variation is minimal if the dislocation is "saturated" with solute atoms and the rate of segregation is proportional to the gradient of concentration. In the case of APB relaxation, Q_{APB}, the driving force is the tendency of the atoms at the APB interface to minimize their average energy by rearrangement. The rate of relaxation is proportional to the deviation from the equilibrium energy of the rearranged APB. With both an apparent activation energy for diffusion in the vicinity of a dislocation core is determined and, both times, the effect of the same process and the same species of atoms is measured. Only the interpretation is different. Considering the fit of the experimental data to the theories, the segregation model agrees better with the results of the strain ageing test at low temperatures, where apparently the same strengthening mechanism is observed. Therefore, the static strain ageing experiments support the segregation hypothesis. The varying APB energy would represent the effects of composition changes at the fault plane rather than a simple reshuffling of the atoms at the APB ribbon.

5. Discussion

5.1 Synopsis

It is useful to give a condensed overview of the results presented in chapter 4. Table 5.1 summarizes the most important properties of the seven different alloys under investigation (following page).

5.2 Strength, Ductility and Failure

The two main hardening mechanisms in the present trialuminides are precipitation hardening and a type of solid solution hardening. The first is observed in the Al_5Ti_2Cu alloy and the Al_5Ti_2Fe alloy of the second series. The precipitation of Al_2Ti particles is due to a minor excess of Ti in these materials. While for Al_5Ti_2Fe a restriction and a shift of the $L1_2$ field towards the Fe corner in the Al-Ti-Fe equilibrium diagram with decreasing temperature is reported [4, 44], the extent of the Al_5Ti_2Cu phase field in the corresponding equilibrium diagram is controversial (for an overview see ref. [19]). At the same time, the $L1_2$ - Al_2Ti field seems to broaden in both systems. Although the $L1_2$ field in Al_5Ti_2Cu is richer in Cu than the Al_5Ti_2Fe field is in iron, it is likely that there is a similar constriction towards lower temperatures. The nominal composition of the Al_5Ti_2Fe (2^{nd}) billet is close to the border of the the single phase field presented in section 2.2.4. Hence, a slight difference in the effective chemical composition as well as a minor error in the diagram or a further constriction of the single phase field at lower (not reported) temperatures explain precipitation. The formation of the Al_2Ti plates is an effective hardening mechanism, the slight difference in the composition between the Al_5Ti_2Fe alloys of the two series gives rise to a yield point differing by a factor of two.

The other hardening mechanism consists of electronic effects of the different elements replacing Al. The simulations by Morinaga et al. show that the M*d* - Ti*d* interactions increase and the M*d* - Al*p* interactions decrease in the order Fe - Mn - Cr in TiAlM alloys [3]. The addition of the next element in this sequence of decreasing atomic numbers, V, replaces Ti and conserves the DO_{22} structure of Al_3Ti. In Al_5Ti_2Cr, it is obvious that Cr replaces at least partially Ti and is no longer available on the Al site to weaken the *p-d* bonds, as confirmed by Nic et al. [7]. Hence, the order of alloy strength, Al_5Ti_2Fe - Al_5Ti_2Cr - Al_5Ti_2Mn, is plausible in terms of *p-d* interaction in $L1_2$ trialuminides and, corresponding to the lowering directionality of these bonds, the shear strength decreases in the same sequence.

alloy	crystal structure	hardness [HV_{30}]	0.2 % yield stress [MPa]			activation volume [b^3]			Q_{APB} [$kJmol^{-1}$]	Q_{SA} [$kJmol^{-1}$]	dissociation distance [nm]		
			23 °C	500 °C	700 °C	23 °C	500 °C	700 °C			23 °C	500 °C	700 °C
Al_5Ti_2Cr	$L1_2$	231	413	326	321	186	501	328	62	60	4.8	-	-
$Al_5Ti_2(Mn,Cr)$	$L1_2$	177	342	326	282	-	-	-	-	-	-	-	-
Al_5Ti_2Mn	$L1_2$	183	311	274	241	233	517	361	29	79	5.0	20	-
Al_5Ti_2Fe (1^{st})	$L1_2$	280	459	437	488	181	246	297	56	58	2.7	7.0	16 / 22
Al_5Ti_2Fe (2^{nd})	$L1_2$	445	1037	891	886	-	-	-	-	-	-	-	-
Al_5Ti_2Cu	$L1_2$	396	1041	980	927	-	-	-	-	-	-	-	-
$Al_3(V,Ti)$	DO_{22}	300	338	384	389	-	-	-	-	-	-	-	-

Table 5.1: Overview of the properties of the current alloys. "-" refers to a value not analyzed.

This order of strength of the ternary additions in $L1_2$ trialuminides is confirmed by the work of another research group. Nic et al. report the results of hardness tests on a series of Al_3Ti based compounds alloyed with transition metals of the fourth row of the periodic table, comprising the six elements between Cr and Cu. These hardness data are presented in figure 5.1 and are compared to the hardness and the compression tests of the current work .

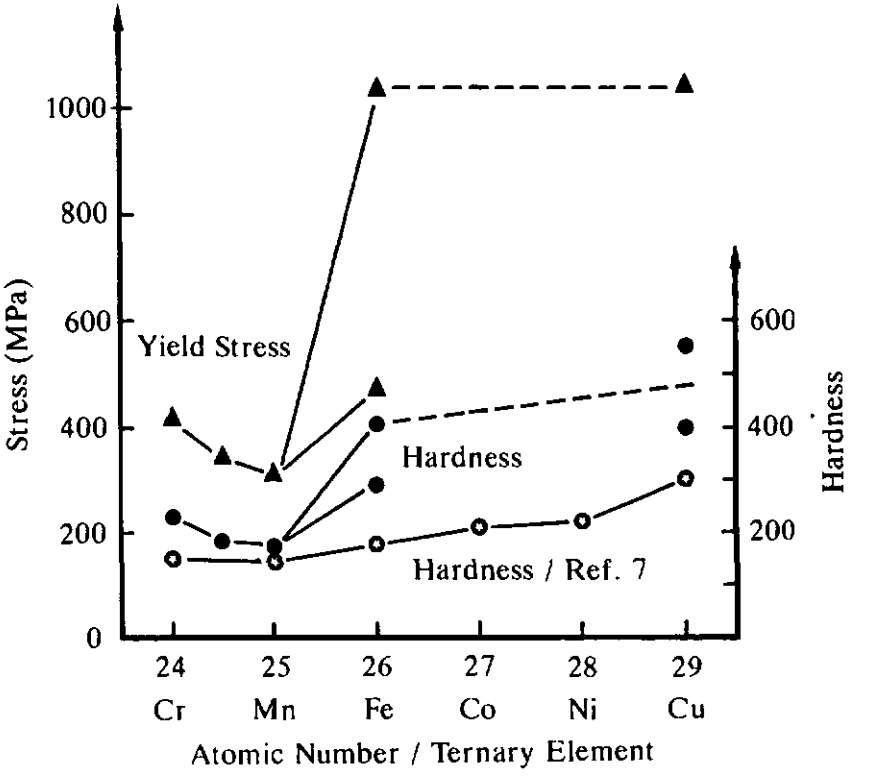

Figure 5.1: Yield stress and hardness of ternary compounds as a function of the atomic number of ternary alloying element. The hardness data labelled by an open star are taken from ref. [7].

The results of Nic and his co-workers show the same tendency as the hardness or the yield stress reported in sections 4.2.2 and 4.2.3, respectively. Beginning with the highest atomic number, the element Cu, the strength decreases continuously towards Mn and increases slightly at the lowest atomic number shown, the element Cr. The difference in the absolute value of

hardness between ref. [7] and the present measurements can be explained in terms of the grain size, which lies between 100 µm and 500 µm in [7] and 20 µm and 35 µm the the own compounds. All in all, there is an agreement between the tendency of the theoretical relative shear strength computed by simulation methods and the experimental findings for $L1_2$ trialuminides.

Very high work hardening rates ϑ are observed in all alloys and over the whole temperature range investigated: 5 GPa, even 8 GPa for Al_5Ti_2Fe (1^{st}), are measured at RT and still 4 GPa for all alloys at 700 °C. In fact, these values are much higher than those found in other intermetallics with the $L1_2$ structure. For instance, the work hardening rate in Ni_3Al alloyed with 1 % Ta is reported as $\vartheta \approx 1$ GPa at RT and $\vartheta \approx 2$ GPa at 500 °C and 700 °C [64]. A high work hardening rate is related to a large density of obstacles formed during straining. The following obstacles created by deformation are observed by TEM investigations:

Dipoles: The density of dipoles in plastically deformed Al_5Ti_2Fe (1^{st}) is high. A smaller, but considerable amount of dipoles is also seen in Al_5Ti_2Cr and Al_5Ti_2Mn. These dipoles can form by the intersection of a mobile dislocation with another dislocation leading to the creation of a jog. If the dislocations are apparently undissociated, this jog will be large and strong. Such undissociated dislocation segments are present in all alloys at lower temperatures, in Al_5Ti_2Fe (1^{st}) up to 500 °C [63]. While further dislocation dissociation is hindered, stable dipoles can be formed.

Straight screw segments: Segments of dislocations in screw orientation are found in all materials investigated in TEM and in Al_5Ti_2Mn these are sometimes seen as groups of straight parallel dislocations. Screw segments are less dissociated than edge segments [59] and lie often along specific crystallographic directions. These segments lie probably in deep Peierls' valley and need a high shear stress to glide through the crystal. On one hand, these straight screw segments can act directly as obstacles to the motion of other dislocations and, on the other hand, they can promote the formation of dipoles as mentioned in the preceding paragraph.

Dislocation agglomerates: Arbitrary collections of dislocations within a grain are observed at higher strains. Such large, three dimensional agglomerates, probably pre-stages of cell walls, are effective obstacles to the movement of dislocations arriving from the free zones inside the grain. These dislocation agglomerates grow with every caught dislocation, i.e. with increasing strain.

The ensemble of these barriers, and, indirectly, with the presumably high Peierls' stress is responsible for the high work hardening rate in the present trialuminides and the preponderance of one of these three obstacles gives rise to the differences between the different alloys at RT and 500 °C. As seen in figure 4.6, at 700 °C the behaviour is similar for all materials, ϑ is

lower and decreases with increasing stress and strain. At this temperature, neither dipoles and nor straight screw dislocations are observed. However, there is extensive cross-slip, both between octahedral planes and between octahedral and cube planes. Cross-slip serves to relax local stress concentrations (the dislocation agglomerates) and to overcome barriers as well as to create more obstacles by the {111}-{010} cross-slip. All in all, the result is the decrease in work hardening rate.

It is interesting to compare the yield stress of the current materials to those of $L1_2$ trialuminides investigated by other groups of researchers. As an example, figure 5.2 shows the yield stress as a function of test temperature for the compound Al_5Ti_2Cr. The results published by Brown, Kumar and Whittenberger [65], by Mabuchi, Hirukawa, Tsuda and Nakayama [66] and by Zhang, Nic, Milligan and Mikkola [67] are presented together with the findings of the present work. There is no uniform behaviour of these four materials, even disregarding the different stress levels. Mabuchi et al. are the only group to find a clear anomalous strengthening with a peak at 600 °C. In the three other compounds, a zone of rather constant yield stress beginning at 300 °C is seen. In the material of Brown et al. this zone ends at 900 °C, Zhang et al. report the end at 600 °C and in the current Al_5Ti_2Cr alloy this zone is not overcome at 700 °C. Brown et al. find a marked increase of the yield point at cryogenic temperatures while in the present investigation no such increase is observed. All four intermetallics have the target composition $Al_{67}Ti_{25}Cr_8$ (in at-%). Chemical analysis of the materials used for compression testing are published by Brown et al. and by Mabuchi et al. The laner is close to the target composition but Brown et al. complain a loss of aluminium. Although the four alloys are prepared by four different techniques, stoichiometry seems to have a crucial importance on controlling the mechanical properties. The marked influence of the Cr content on the hardness of Al-Ti-Cr alloys reported by Nic et al. [7] confirms this hypothesis.

For Al_5Ti_2Mn the agreement of the results of the different research groups is better. The alloy of Zhang et al. [67] seems to be considerably softer than those of Brown et al. [65] and of the own compound but a yield stress relatively constant in the temperature range from 300 °C up to about 800 °C is confirmed by all three investigations. There is a difference at very low temperatures. Contrary to the current results, Brown et al. report a pronounced increase in yield stress at temperatures below RT.

As seen in section 4.2.3 for the Al_5Ti_2Fe alloys of the two series, the results of compression tests on such trialuminides published in the literature also differ markedly. Nevertheless, there are two common findings. No marked increase of the yield point at the temperature of liquid nitrogen is observed, neither in the present Al_5Ti_2Fe (1^{st}) compound nor in the work reported by Kumar and Pickens [20]. In every case an anomalous strengthening is seen. In ref. [20] the

stress peaks at about 400 °C, DiPietro, Kumar and Whittenberger [68] observe a peak at 500 °C and in the current case the strengthening continues up to 700 °C.

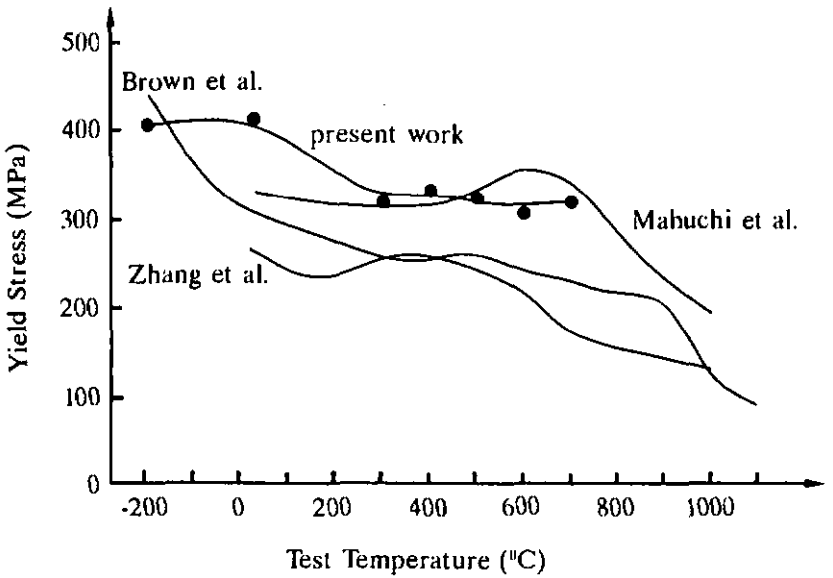

Figure 5.2: Yield stress as a function of the test temperature for different Al_5Ti_2Cr alloys. Synopsis of current results compared with the findings of other research groups.

Considering the reaction schemes of superdislocations on {111} planes presented in section 2.3.4, figure 2.8, the results of the compression tests must be analyzed under this aspect. While antiphase boundary (APB) type dissociation is known to give rise to anomalous strengthening in many cases, superlattice intrinsic stacking fault SISF type dissociation leads to an unusual increase in strength at very low temperatures because the complex, three dimensional fault immobilizes the dislocation in the absence of thermal activation. Prototypes of these two classes are Ni_3Al for the APB type, showing a large anomalous strengthening, and Pt_3Al for the SISF type, known to exhibit a sharp increase of the yield point at temperatures below RT. Figure 5.3 illustrates the yield stress of these two intermetallics and compares it to the behaviour of Al_5Ti_2Fe (1^{st}). It is clearly seen that the anomalous strengthening of the trialuminide is small in comparison to that of Ni_3Al. But at low temperatures, the increase of the yield stress in Al_5Ti_2Fe is negligible in relation to that exhibited by Pt_3Al. The latter fact sustains the findings of TEM analysis, namely that the superdislocations are separated by an

APB. This type of dissociation is confirmed for all compounds examined by TEM, i.e. Al_5Ti_2Cr, Al_5Ti_2Mn and Al_5Ti_2Fe (1^{st}) and none of these three alloys show a pronounced rise in yield stress at cryogenic temperatures. A SISF immobilizes topographically the superdislocation enclosing it, while a superdislocation separated by an APB does neither automatically undergo {111}-{010} cross-slip nor has this cross-slip always a pinning effect on the dislocation. Both depend on the energetic and elastic anisotropy of the crystal. Therefore, $L1_2$ intermetallics showing no distinct anomalous strengthening, like Al_5Ti_2Cr and Al_5Ti_2Mn, can belong to the APB class.

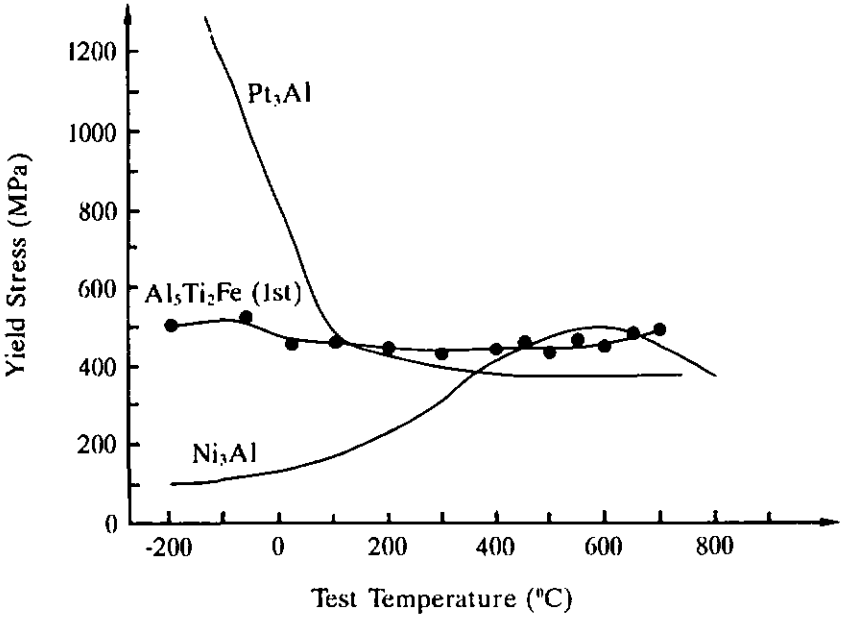

Figure 5.3: Yield stress as a function of test temperature. Data for Al_5Ti_2Fe (1^{st}) are part of the present work, Ni_3Al after Mishima, Oya and Suzuki [69] and Pt_3Al after Wee, Noguchi, Oya and Suzuki [70].

As presented in figure 2.9, a further dissociation of the partials of the superdislocations in Shockley partials is possible. Even under weak beam conditions, such Shockley partials are never observed during TEM investigations. Taking eq. 2.19, it is seen that cross-slip of Shockely partials, so closely separated that they are not resolved in weak beam, is related to an

activation volume $\mathbf{U} \leq 400\ b^3$ for the present alloys with a Burgers' vector $b \approx 0.28$ nm (cf. section 2.3.2).

TEM examinations of Al_5Ti_2Fe (1^{st}) reveal cross-slip between octahedral planes at 500 °C and {111}-{010} cross-slip at 700 °C. The serrated flow is most persistent in Al_5Ti_2Fe (1^{st}). In this compound the saturation during static strain ageing tests becomes unstable at 225 °C already, the activation energy is the lowest and it is the only material which exhibits a few serrations even at 700 °C. In spite of this, the measured activation volume confirms cross-slip being the mechanism controlling deformation between 450 °C and 700 °C. The increasing yield stress seen at these temperatures can be thus be interpreted, as for Ni_3Al alloys, by pinning effects caused by the cross-slip of {111}<011> superdislocations onto the cube plane. The driving force of this cross-slip can be the anisotropy of the APB energy, namely 72 $^{mJ}/_{mol}$ on {111} against 45 $^{mJ}/_{mol}$ on {010} at 700 °C (cf. section 4.3.1). It is also possible that elastic anisotropy may play a role in assisting the cross-slip process.

In Al_5Ti_2Cr and Al_5Ti_2Mn, the experimental activation volume in the range of 450 °C to 600 °C is too high to interpret the dominant deformation mechanism as cross-slip. It is likely that the $\mathbf{U}$ values in this temperature range (500 b^3 and more) are related to the dynamic strain ageing. At first sight, this a disagreement to the findings of the strain ageing tests. In these two alloys, the Portevin-LeChâtelier effect is less persistent and these materials have a higher activation energy, determined as Q_{SA} as well as Q_{APB}. The contradiction that the deformation in this temperature range seems to be dominated by DSA although strain ageing is less favoured in Al_5Ti_2Cr and Al_5Ti_2Mn compared to Al_5Ti_2Fe (1^{st}) can only be solved if the tendency to cross-slip of dislocations in the Cr and Mn alloyed compounds is smaller than in Al_5Ti_2Fe (1^{st}). In this view-point the moderate strengthening identified in these alloys as a constant yield stress between about 300 °C and about 600 °C is attributed to DSA. Above 600 °C, the activation volume drops below 400 b^3, suggesting cross-slip as the deformation mechanism. At the same temperature, a marked increase in the ductility in compression is noticed, indicating that the dislocations may overcome obstacles and reduce stress concentrations. Cross-slip is a plausible explanation of such a dynamic recovery. Bearing in mind that 700 °C corresponds to 0.6 T_m, another possible explanation for this increase in ductility is dislocation climb. Unfortunately, no TEM investigations are available to check the correctness of these two hypothesis.

It is interesting to speculate on the reasons for the differences in behaviour of the Fe containing alloy versus the Al_5Ti_2Cr and Al_5Ti_2Mn alloys. The ease of cross-slip found in Al_5Ti_2Fe (1^{st}) could be attributed to a higher driving force. Although no experimental values of the anisotropy of the APB energy, γ, in Al_5Ti_2Cr and Al_5Ti_2Mn are available, the difference between γ_{111} and γ_{010} are thought to be smaller than in Al_5Ti_2Fe. Using a local density functional approach,

Fu calculates the APB energies for Al_3Sc and Al_3Ti [26]. The high energy on {111} plane is attributed to the directional bonding of d - p electrons. The decrease of the charge transfer from Al to Ti , i.e. the lowering of the directionality of the d - p bonds, accomplished by alloying of less electropositive transition metals has two effects: First, the DO_{22} crystal structure of Al_3Ti is converted to $L1_2$ and second, the APB energy on {111}, γ_{111}, is considerably reduced [60]. The lower directionality of the d - p bonds changes essentially γ_{111} because an antiphase boundary on an octahedral plane involves exclusively nearest neighbours with this type of bonding. The APB energy on {010} is less affected [26]. As stated at the beginning of this section, Cr and Mn lower the directionality of the p - d bonds more efficiently than Fe does. The more isotropic bonding in Cr and Mn modified trialuminides gives rise to more equal APB energies and, hence, smaller elastic anisotropy. It seems that dislocation pinning by cross-slip is less common in Al_5Ti_2Cr and Al_5Ti_2Mn than in Al_5Ti_2Fe because the driving force for {111}-{010} cross-slip is insufficient. However, at a certain temperature, about 650 °C in the present case, thermally activated cross-slip assists the dislocations to surmount obstacles, enhances ductility and lowers the work hardening rate.

It is difficult to estimate differences in the shear strength of atomic bonds due to the different alloying additions in $L1_2$ trialuminides. Bearing in mind that all samples fail by transgranular cleavage, that compression samples of all alloys have the same dimensions and that the grain sizes are similar, the variation of the stress at failure of only 30 % between the the most brittle and the most ductile compound at RT suggests that differences in the strength of atomic bonds are relatively small. However, large changes in atomic interaction would destabilize the $L1_2$ crystal structure. The local stress within a stress concentration which leads to the separation of atomic planes is not known. Unfortunately, it seems that for the $L1_2$ trialuminides the cleavage strength is low and does not vary significantly from a phase with one alloying element to a another. Hence, the similar ultimate compression strength observed in the five different materials with $L1_2$ crystal structure (cf. figure 4.7) can be understood, taking into account that all compression samples have the same geometrical dimensions.

Considering the difference at RT in maximum stress R_m and maximum strain, ε_{max}, between the two Al_5Ti_2Fe intermetallics of the 1st and the 2nd series, it is seen that the excessive precipitation in the alloy of the second series reduces both R_m and ε_{max}. At 700 °C, Al_5Ti_2Fe (2nd) fails at a similar strain as at RT but at a higher stress than Al_5Ti_2Fe (1st). This indicates that thermal activation helps the dislocations to overcome the most active site of stress concentration at RT, namely the Al_2Ti precipitates, but the low cleavage strength hinders a further deformation without breaking. Hence, the brittle fracture in all these trialuminides is not particle or impurity induced but is directly related to their intrinsically low cleavage strength.

The tetragonal $Al_3(V,Ti)$ alloy must be considered separately. It does not have five independent dislocation slip systems and deformation is accomplished primarily by twinning and only partially by dislocation movement [14]. Twinning provides only little macroscopic deformation and, consequently, at low temperatures, samples made of this DO_{22} material fail at very low strains, even when deformed in compression. At high temperatures, dislocation slip is enhanced and failure occurs at higher strains but still in a brittle manner. It is likely that $Al_3(V,Ti)$ exhibit also an intrinsically low cleavage strength, since Ni_3V which exhibits the same crystal structure and the same deformation systems, is reported to have a good ductility in compression [16].

As presented in section 4.2.2, the first cracks on the surface of the compression samples appear at very low strains. For the brittle compounds, such as Al_5Ti_2Cu and $Al_3(V,Ti)$, the first cracking is already catastrophic, while in the more ductile intermetallics these flaws grow and join over a large range of strain before failure occurs. The cracks form under tensile stress at the circumference where barrelling of the initially cylindrical sample induces triaxial stress states. In the brittle materials, the cracks seem to run through the whole sample although at very low strains, before barrelling becomes important, the sample is under uniaxial compressive stress. In the ductile alloys, the compressive stress state inside the sample seems to stop the propagation of cracks. In this case, failure occurs after severe deformation. The zone of triaxial stress is full of cracks, extends towards the middle of the sample and loweres the load bearing section. At a certain amount of deformation, shear deformation between the scarcely deformed dead zone and the rest of the sample reaches its limit. Breaking spares the conical dead zones but disintegrates the deformed region of the sample. The fragments found after failure support this failure hypothesis.

Even the alloys appearing ductile in compression exhibit only minor plastic deformation under tensile stress. This is seen in bend testing at RT, where the maximum strain is estimated to be 0.34 % in the best case. Tensile tests carried out by Kumar and Brown confirm the poor tensile ductility [71, 72]. They investigate cast, homogenized and isothermally forged $Al_{67}Ti_{25}Cr_8$ and $Al_{66}Ti_{25}Mn_9$ alloys. At room temperature, no measurable ductility is observed for the Cr modified compound and the Mn modified intermetallic exhibits 0.2 % plastic deformation. At 800 °C, the maximum strain, A, is reported as A = 19 % for $Al_{67}Ti_{25}Cr_8$ and as A = 5 % for $Al_{66}Ti_{25}Mn_9$.

Unfortunately, the ductility of the present trialuminides could not be related and compared to the technically useful fracture toughness, K_{Ic}. K_{Ic} is a measure for the resistance of a material against crack propagation and an interesting value considering the early flaws observed in compression sample. As reported in section 4.2.2, cracks starting from a Vickers indentation are much too irregular to deduce fracture toughness data. Taking the maximum load at which

no cracks form by hardness testing, the materials can be separated into two groups. The first group, containing Al_5Ti_2Cr, $Al_5Ti_2(Mn,Cr)$, Al_5Ti_2Mn and Al_5Ti_2Fe (1^{st}), exhibit a crack free load of about 30 kgf and extensive plastic deformation around the indentation. The second group includes Al_5Ti_2Fe (2^{nd}), Al_5Ti_2Cu and $Al_3(V,Ti)$ and withstands a load of about 5 kgf without cracking and at higher loads, the cracks are irregular. Qualitatively, the indentation experiments confirm the findings of ductility in compression.

The publication of Turner et al. [23], mentioned in section 2.1.4, considers the deformation occuring by slip of undissociated <110> dislocations, because at that time, these authors do not see separated superdislocations by TEM examinations. Although the present work proofs the dissociation of the dislocations into pairs of $^1/_2$<110> partials, the Rice-Thomson citerion ($\mu b/\gamma_s < 10$ for ductile behaviour, [22]) is still fulfilled, since a single partial dislocation cannot slip away from the crack tip and the Burgers' vector $b = a$<110> must be considered. Taking $b = 0.56$ nm and $\mu = 84$ GPa [60] and the true surface energy, $\gamma_s \approx 2.4$ Jm^{-2} [23], the Rice-Thomson ratio is calculated as $\mu b/\gamma_s \approx 20$ for the present $L1_2$ trialuminides. Hence, the Rice-Thomson approach predicts brittleness correctly. Decreasing the Rice-Thomson ratio would require either lowering the shear modulus or increasing the surface energy or finding a smaller Burgers vector. The latter is bound to the operating slip system and the other two parameters depend on the electronic structure of the crystal and can be modified by suitable alloying. As shown previously, varying the ternary alloying additions does not provide an effect which would suppress cleavage and enhance ductility fundamentally. Another criterion, similar to the Rice-Thomson ratio, is proposed by Pugh [73]. He expects ductile behaviour if $K/\mu > 2$, where K is the bulk modulus. For Al_5Ti_2Fe, the bulk modulus is reported as K = 89 GPa [23], giving rise to $K/\mu \approx 1.1$. Again, the Pugh criterion predicts brittleness correctly.

5.3 Activation Volume and Dislocation Dynamics

The dependence of the activation volume, U, on temperature in zone I proofs that deformation occurs not by an athermal process (cf. table 2.1). An increasing U with increasing applied stress, σ, can be interpreted as the increase of the thermal stress component $(\sigma - \sigma_{int})$, where σ_{int} is the internal stress. As reported in section 2.3.2, Biget and Saada observe a dependence of the activation volume on stress as

$$U = B(\sigma - \sigma_{int})^{-2} \qquad (2.23)$$

where B is a constant [49]. There is a reasonable agreement with eq. 2.23 for the current intermetallic alloys. As an example, figure 5.4 depicts a plot of the applied stress as a function of $U^{-0.5}$ for Al_5Ti_2Mn (figure 5.4a) and Al_5Ti_2Fe (1^{st}) (figure 5.4b) at RT.

Unfortunately, only a few data on σ and U at the temperatures of zone I are available. Even worse, the yield stress measured at - 60 °C is unusually high for Al_5Ti_2Mn and Al_5Ti_2Fe (1^{st}) (cf. table 4.3), so that a statistically relevant extrapolation of the activation volume at 0 K following the method of Biget and Saada [49] is not possible. In spite of this, the consequences of such an extrapolation will be discussed qualitatively.

Bearing in mind that at 250 °C the internal stress in Al_5Ti_2Mn is determined as $\sigma_{int} = (0.95 \pm 0.03)\,\sigma$, thus $(\sigma - \sigma_{int}) = (0.05 \pm 0.03)\sigma$, figure 5.4a shows in fact a dependence $U \sim (0.05\sigma)^{-2}$. Al_5Ti_2Cr and Al_5Ti_2Fe (1^{st}) are believed to behave similarly although neither measurements of activation volume at temperatures below RT are performed in the first case nor data on σ_{int} are available in the second case. The following discussion focuses on Al_5Ti_2Mn as an example for all three alloys. Considering the small variation of the yield stress between - 196 °C and 300 °C only a mild dependence of σ_{int} on temperature is expected. On the other hand, at very low temperatures close to absolute zero, σ is expected to increase which in turn gives rise to a large difference $(\sigma - \sigma_{int})$.

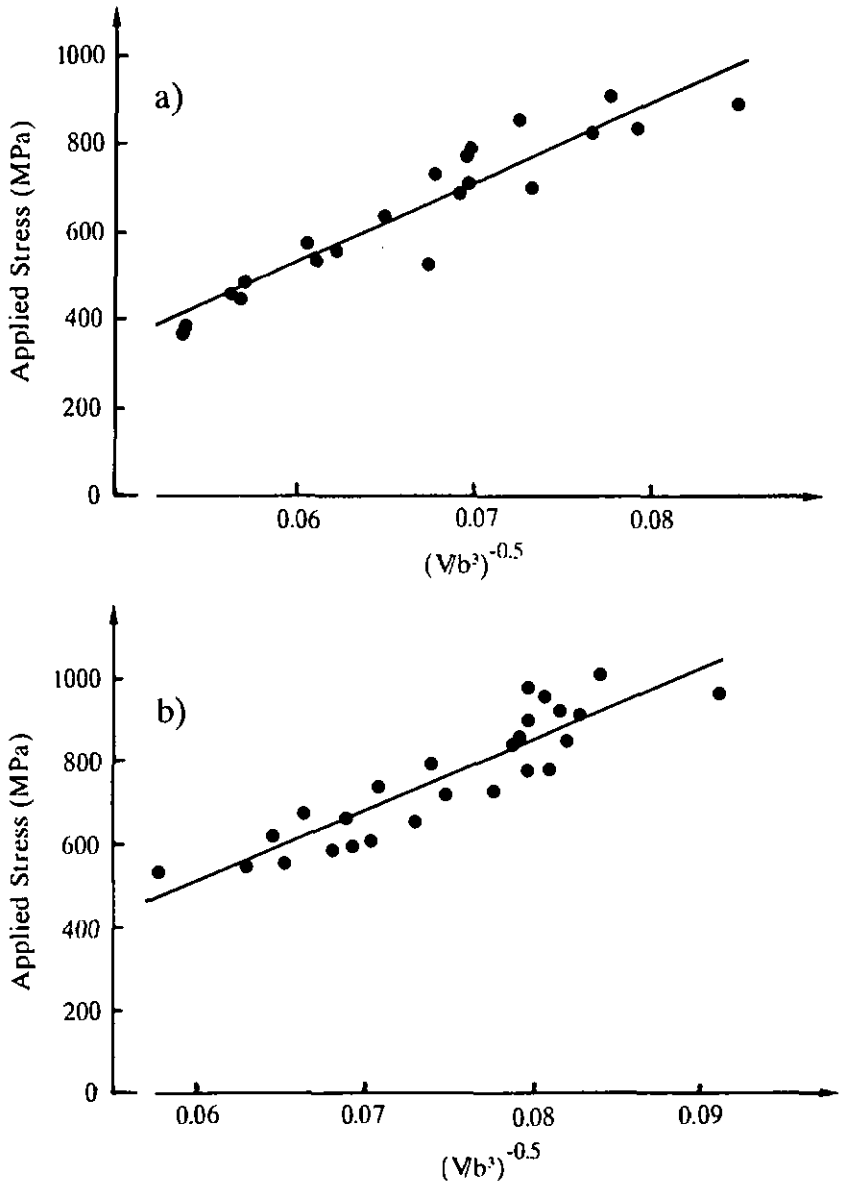

Figure 5.4: *Applied stress as a function of* $(V/b^3)^{-0.5}$ at RT. a) Al_5Ti_2Mn (cf. figure 4.12b) and b) Al_5Ti_2Fe (1^{st})

Assuming for a Peierls' mechanism $\mathbf{U} = 10\,b^3$ at 0 K, it is seen by means of eq. 2.22 that $(\sigma - \sigma_{int})$ would have to increase by a factor of five, i.e. a drop by a factor of 25 in $\mathbf{U}$, between RT and 0 K, which would lead to a yield stress of more than 450 MPa at 0 K (compared to 310 MPa at RT and 340 MPa at -196 °C). However, a relatively sharp increase of the yield stress between 77 K and 0 K as would be expected for $V \leq 10\,b^3$ at 0 K seems rather unlikely, since such a behaviour of the flow stress is common for ordered phases which deform by superdislocations separated by a SISF and not by an APB as the present trialuminides. In this viewpoint, a Peierls' mechanism controlling deformation at very low temperatures is not excluded but unlikely.

If solution hardening dominates dislocation glide at 0 K, the expected activation volume at this temperature can be deduced using eq. 2.20. Assuming a concentration of oxygen in solution of 200 ppm (cf. ref [57]), the corresponding activation volume is deduced as $70\,b^3 \leq \mathbf{U} \leq 350\,b^3$ (depending on x in eq. 2.20). Even the lower limit is more than the measured $\mathbf{U}$ at -196 °C, while $\mathbf{U}$ is thought to decrease towards lower temperatures. Under the condition that the order of magnitude of the limit of solubility of O in Al_5Ti_2M type intermetallics is correct [57], oxygen as the element responsible for solution hardening is ruled out. Taking the concentration of the ternary alloying addition, 8 %, the corresponding activation volume at 0 K is estimated as $4\,b^3 \leq \mathbf{U} \leq 18\,b^3$, depending on x in eq. 2.20. For $\mathbf{U} = 18\,b^3$, $(\sigma - \sigma_{int})$ would have to increase by a factor of 3.5 between RT and 0 K. In turn, this would give rise to a yield stress in the magnitude of 400 MPa at 0 K, which seems a reasonable value for an ordered alloy in which dislocations are dissociated by an APB and for which no marked increase of the flow stress at very low temperatures is expected.

It must be emphasized that this is a rough estimation using the small data base on the activation volume available at low temperatures. Qualitatively, $\mathbf{U}$ is expected to decrease considerably (e.g. by a factor of two) but not drastically (e.g. by a factor of ten) between the lowest experimentally measured value at -196 °C and absolute zero. The consequences for the deformation mechanisms are the following:

- A Peierls' mechanism controlling the dislocation movement at very low temperatures is unlikely.

- Solution hardening as the mechanism controlling deformation at 0 K would base on solutes in a concentration in the order of magnitude of %. The ternary alloying additions (Cr, Mn and Fe) with a concentration of 8 % cannot be excluded as the solute atoms responsible for solution hardening.

In zone II, beginning at RT, the influence of dynamic strain ageing (DSA) becomes increasingly important. Solute atoms are shown to act as obstacles and control dislocation slip at low temperatures. But in zone II, these obstacles evolve during dislocation movement, or more precisely, solution hardening becomes more pronounced during the waiting time a dislocation is pinned in front of an obstacle. The interaction of solute atoms with dislocations draws the solutes towards the dislocation and they segregate around it. While the model of the activation volume considers one single dislocation, i.e. one single superpartial in the present case, DSA affects the superdislocation as a system comprising the pair of partials and the APB ribbon. For example, the increasing concentration of solutes at the APB will change the APB energy which additionally influences the mobility of the whole dislocation system. Another example, the leading partial of a superdislocation cannot break away of the solute pinning unless the trailing partial is also enabled to do the same. It is not a simple atmosphere of solutes which affects the dislocation slip but a complex diffusional process increasing the effective local solution hardening as well as lowering the APB energy. Compared to this, the base of the model of activation volume, i.e. slip of one independent superpartial, does not hold. Hence, the values of U measured in zone II have poor significance. Just as the findings of activation volume measurements and static strain ageing experiments cannot be compared directly because the atomic model of the dislocation is different in each case. In this view-point it is also useless to try an interpretation of the quantitative difference of the activation volume of Al_5Ti_2Mn and Al_5Ti_2Fe (1^{st}) in zone II. The plastic behaviour at the temperatures of zone II is dominated by the dynamic strain ageing. The strain ageing experiments provide a further description of this process, which take into account the whole superdislocation as a system, cf. section 5.4.

Dynamic strain ageing controls deformation in zone III. As mentioned above, a further interpretation of the deformation mechanisms in terms of the activation volume are impossible.

In zone IV, Shockley cross-slip is the most likely mechanism controlling deformation in Al_5Ti_2Fe (1^{st}). This means that there is a continuous transition from the DSA process to the cross-slip process. Indeed, both processes could exist in parallels over a certain range of temperature. In this case, the mechanism controlling deformation is that one which provides the more effective dislocation pinning. Cross-slip gives rise to the anomalous strengthening, while the effect of DSA on strength is much lower and in Al_5Ti_2Fe (1^{st}) it is probably even masked by the influence of {111} - {010} cross-slip. Hence, the immobilizing effect of cube cross-slip on dislocations must be higher than in the case of DSA.

The parallel existence of DSA and cross-slip, even at the same temperature, is illustrated by the fact that at low strains, serrated flow is observed, while at higher strains, the flow is continuous (cf. figure 4.8, 600 °C). This suggests that DSA plays a major role in the small range of deformation at the beginning of the plastic flow (cf. table 4.5). A prerequisite for measurements

of U is homogeneous flow, thus no experimental data of the activation volume in the regions of serrated flow are available, but U is expected to be negative. The activation volume indicates the mechanism relevant to deformation or, in other words, identifies the main obstacle to dislocation slip. Considering the model of Paidar, Pope and Vitek for the anomalous strengthening, {111} - {010} cross-slip can pin a superdislocation before it has completely cross-slipped, i.e. before the APB it encloses, lies on the cube plane. Although <110> superdislocations on {010} are observed only at 700 °C, cube cross-slip can be the most important obstacle to dislocation glide in the whole temperature range of zone IV. This implies that the driving force for cube cross-slip must be relatively high in Al_5Ti_2Fe (1^{st}), otherwise the effect of strain ageing, i.e. an "atmosphere" of solutes dragged along with the dislocation, could not be masked by the cube cross-slip. The anisotropy of the APB energy in Al_5Ti_2Fe ($\gamma_{111}/\gamma_{010}$ = 1.6) support the assumption of a high driving force for {111} - {010} cross-slip.

The activation volume for Al_5Ti_2Cr and Al_5Ti_2Mn, measured when serrated flow is overcome, is considerably higher than that observed for the Fe alloyed compound. The values, $500\,b^3 \leq U \leq 630\,b^3$, cannot be attributed to one of the obstacles to dislocation glide presented in section 2.4.2. There is no objection, neither on the microscopic nor on the macroscopic level, to suppose that dominant deformation mechanism in the region of homogeneous flow is the same as in the region of serrated flow. This means that there is a transition from severe dynamic strain ageing, manifested as the Portevin-LeChâtelier effect with a corresponding negative U, to DSA manifest as a solute "atmosphere" dragged along with the moving dislocation and changing the dissociation distance of the superpartials quasi instantly. This steady strain ageing gives rise to a macroscopically continuous flow and controls the dislocation movement in Al_5Ti_2Cr and Al_5Ti_2Mn in the temperature range from 450 °C to about 600 °C. The effect of DSA is not masked by the beginning of {111} - {010} cross-slip as in Al_5Ti_2Fe. This fact indicates that the driving force for such cross-slip is smaller in Al_5Ti_2Cr and Al_5Ti_2Mn. Unfortunately, no experimental data on the APB anisotropy of the latter two alloys are available, but the tendency of Cr and Mn to create more isotropic atomic bonds than Fe does, supports the hypothesis of different driving forces for cube cross-slip established in section 5.2.

At even higher temperatures, the activation volume for Al_5Ti_2Cr and Al_5Ti_2Mn drops to values consistent with cross-slip. As seen above, the {111}-{010} anisotropy of the APB energy in these intermetallics is probably lower than in Al_5Ti_2Fe. Hence, the driving force is smaller and the onset of {111} - {010} cross-slip is shifted to higher temperatures where thermal activation is enhanced. The absence of an anomalous strengthening in these two alloys at 700 °C indicates that the dislocation pinning effect due to cube cross-slip is relatively moderate. In this case, the transition from DSA to cube cross-slip as the dominant deformation mechanism is explained rather by exhaustion of DSA than by energetically more favorable cross-slip. Although less

effective than in Al_5Ti_2Fe, dislocation pinning by cube cross-slip becomes the most important obstacle to dislocation movement in the Cr and Mn alloyed trialuminides, as suggested by the activation volume. However, cross-slip acts not only as anchoring point it is also an auxiliary means for dislocations to overcome obstacles, as indicated by the enhanced ductility of Al_5Ti_2Cr and Al_5Ti_2Mn at 700 °C.

5.4 Diffusion and Strain Ageing

Serrated flow seems to be a phenomenon commonly observed at intermediate temperatures in $L1_2$ trialuminides. It is reported for different alloys, e.g. $Al_{22}Ti_8Fe_3$ [74], $Al_{67}Ti_{25}Ag_8$ [75], Al_5Ti_2Cr, Al_5Ti_2Mn and Al_5Ti_2Cu [57]. Kumar, Herring and Whittenberger observe a coincidence of the temperature range of serrated flow and of the positive temperature dependence of strength in their Fe modified trialuminide [74]. The authors believe the serrations to originate in the cross-slip behaviour intrinsic to this material. Mabuchi, Hirukawa, Katayama, Tsuda and Nakayama see continuous serrations during the compressive deformation of their Ag alloyed compound at 400 °C [75]. For these authors, it is doubtful that this Portevin-LeChâtelier effect is intrinsic to the ternary $L1_2$ alloys, but no explanation is offered. More recently, Potez, Lapasset and Kubin identify the serrated flow of Cr, Mn and Cu modified trialuminides in the temperature range of 300 °C to 500 °C as dynamic strain ageing [57]. This group of searchers try to explain the phenomenon by segregation of oxygen to the dislocations. Two Al_5Ti_2Cu alloys with different O content exhibit almost the same strain rate sensitivity and similar serrated flow at 300 °C. It is argued that, on the one hand, the solubility of O in the $L1_2$ matrix can be lower than the oxygen concentration in the purer intermetallic, thus O can still be responsible for DSA, or, on the other hand, a simple redistribution of solutes within the distorted regions of the dislocation cores can cause DSA.

One reason for the disagreement on the interpretation of the serrated flow is the hardly investigated and poorly understood diffusion properties of solutes in ordered compounds. Van Loo and Rieck [76] investigate diffusion in the binary system Al-Ti. Using diffusion couples of different Al-Ti alloys, the coefficient of diffusion is measured. The diffusivity is seen to be the highest in Al_3Ti compared to all other stable phases in the Al-Ti system. For the diffusion couple Al-Al_3Ti, the activation energy of diffusion is determined as $D = 94\ ^{kJ}/_{mol}$. Conscious of the relatively low temperatures investigated (516 °C to 642 °C), the authors attribute this low value to grain boundary diffusion.

Kumar and Whittenberger deduce the interdiffusion coefficients from concentration-distance profiles that are generated from $Al_{67}Ti_{25}Cr_8$ - $Al_{66}Ti_{25}Mn_9$ diffusion couples which are exposed to temperatures in the range of 700 °C to 1000 °C [77]. Both materials are completely soluble in one another and the couple system is treated as pseudobinary. The activation energy for Mn (Cr) interdiffusion varies between $260\ ^{kJ}/_{mol} \le D \le 350\ ^{kJ}/_{mol}$ depending on the relative Mn concentration. The marked deviation of the interdiffusion data at 700 °C is assumed to be the result of grain boundary diffusion. Considering only the diffusion data between 700 °C and 800 °C, the activation energy is determined as $D \approx 90\ ^{kJ}/_{mol}$, compared to $350\ ^{kJ}/_{mol}$ in the temperature range of 800 °C to 1000 °C. Thus, at intermediate temperatures, there is an

agreement with the activation energy of diffusion in the Al-Al_3Ti couple of van Loo and Rieck [76]. Bearing in mind that Mn replaces Al in Al_3Ti, this seems to be reasonable.

Apparently, there is a large difference between the diffusion coefficients of volume controlled diffusion at high temperatures and of grain boundary or pipe diffusion at intermediate temperatures. It is supposed that the degree of long-range order in Al_3Ti-based ordered compounds hinders bulk diffusion and gives rise to correspondingly high activation coergies for volume diffusion but diffusion in regions of disturbed order such as APB or grain boundaries is much more favorable. It is generally accepted that there is a complex dependence of diffusional mobility and the degree of order. An increase in the degree of long range order, S, leads to a decrease in diffusional mobility. There is experimental evidence for the dependence of the self diffusion coefficients on S in Al-Fe intermetallic phases, in $Ni_3(Al,Ti)$ and in β brass [78]. This is explained by the energy point of view. In a material with a high degree of order, the transfer of an atom to one of the nearest neighbour sites of another sublattice is not favorable. It is assumed that the diffusion mechanism involves the movement of atomic groups without disturbing the long-range order [78]. On the other hand, in a partially ordered alloy a normal diffusion mechanism involving single vacancies is possible. The present case of ternary ordered intermetallics has its own peculiarities. There are not only Al and Ti sublattice sites, furthermore it is not known whether there is a certain preferential ordering of the ternary element within the Al sublattice and what this ordering would comprise. X-ray diffraction shows no peak which can be attributed to such an additional order. Considerations, what a region of disturbed order means on the atomistic level, are only speculation. It is clear that a ternary atom in excess on a shear produced APB reduces the APB energy. Higher concentrations of the ternary alloying additions are thought to destabilize the $L1_2$ order. On the other hand, a shear produced APB creates a new stacking sequence which can represent a new local order (cf. the relationship between DO_{22} and $L1_2$, figure 2.1). However, the great difference in the activation energy of diffusion between high and intermediate temperatures suggest that there is a pronounced preference for diffusion along the superdislocations or grain boundaries in Al_3Ti based compounds at intermediate temperatures.

The activation energy has been determined a second time using the model of varying APB energies. As seen in section 4.3.3, the activation energies calculated for the APB relaxation theory are similar to those for the segregation model for Al_5Ti_2Cr and Al_5Ti_2Fe (1^{st}). For Al_5Ti_2Mn, the marked difference between Q_{SA} (79 $^{kJ}/_{mol}$) and Q_{APB} (29 $^{kJ}/_{mol}$) is explained by the, considering the whole temperature range under investigation, poor approach of the simple APB relaxation model to the experimental results. Q_{APB} determined by the method in section 4.3.3 depends on the temperature homologous to the onset of the unstable saturation. Contrary to the Cr and Fe alloyed compounds, unstable saturation is not yet observed at the highest temperature used during static strain ageing tests for Al_5Ti_2Mn. However, only direct

TEM observations of the evolution of the dissociation distance would supply further APB relaxation data to establish more complex antiphase boundary relaxation kinetic models (cf. ref [38]) or an identification of different ageing steps, e.g. locally higher solution hardening and only minor APB relaxation at lower temperatures and APB relaxation with almost constant local solution hardening at higher temperatures.

Static strain ageing cannot be used to establish diffusion coefficients. The system investigated does not correspond to a diffusion couple. Hence, the pre-exponential factor is not defined and it is not known which species of atoms diffuse. Nevertheless, the values of Q_{SA} can be compared to known activation energies of diffusion to check if there is a correspondence. The activation energies determined by strain ageing tests are believed to describe the same process which controls diffusion in the experiments of van Loo and Rieck [76] and Kumar and Whittenberger at lower temperatures [77]. Diffusion in regions of disturbed order in the case of strain ageing means diffusion around the APB ribbon spread out by the superdislocations. This explains also the increase of the dissociation distance of superpartials observed by in-situ annealing in TEM [62]. Considering that the segregation model agrees better with the experimental data than the APB relaxation model (cf. figure 4.17c to 4.17e and 4.27, respectively), it is supposed that the process of broadening of the APB ribbon comprises not only the rearrangement of atoms lying directly at the fault plane but also the segregation of atoms normally occupying the Al sites to the fault. In disordered alloys this phenomenon is known as Suzuki effect. The driving force is the tendency to equalize the overall energy by lowering the APB energy. The disturbed order at the fault plane promotes diffusion.

Again, the tetragonal $Al_3(V,Ti)$ intermetallic behaves differently. On deforming this material in the critical temperature range, no regular serrated flow is seen. The sporadic drops in the stress-strain curve are clearly due to cracking. It must be kept in mind that this DO_{22} phase is still very brittle at these temperatures. Although no detailed analysis has been accomplished on the strain ageing behaviour of $Al_3(V,Ti)$, it is interesting to speculate on the reasons for the absence of the Portevin-LeChâtelier effect. It is known that deformation in this compound is carried by twinning and dislocation glide together [14]. In the present case, zones of a considerable dislocation density and free of twins are seen in a sample deformed 0.5 % at 300 °C. Figure 5.5 shows a TEM micrograph of such a zone.

The question of the missing pinning effect at this temperature rises. The content of interstitials in $Al_3(V,Ti)$ is thought to be similar to that in the other $L1_2$ intermetallics because the same preparation technique is used. As in Al_5Ti_2Cr, Al_5Ti_2Mn and Al_5Ti_2Fe (1^{st}), segregation of interstitial atoms is unlikely to cause dislocation pinning. There is no evident reason that serrated flow should be intrinsic to the $L1_2$ crystal structure. The active dislocation slip systems are the same and the APB energy is similar, e.g. $\gamma_{111} \approx 200$ mJm^{-2} for Al_3Ti at 400

°C [79]. But in $Al_3(V,Ti)$ the ternary alloying element V does not substitute Al and cannot change the high energy Al*p* - Ti*d* bond by a weaker *d* - *d* interaction. This suggests that in Al_5Ti_2M type trialuminides, the ternary element M segregates to the APB and lowers its energy. The unlike Al-Ti "wrong" neighbours are replaced by more similar M-Ti "wrong" neighbours giving rise to lower ordering energy and lower APB energy. It is not possible to prove this hypothesis with the available experimental data. Only further examinations including in-situ annealing of $Al_3(V,Ti)$ could clarify this point.

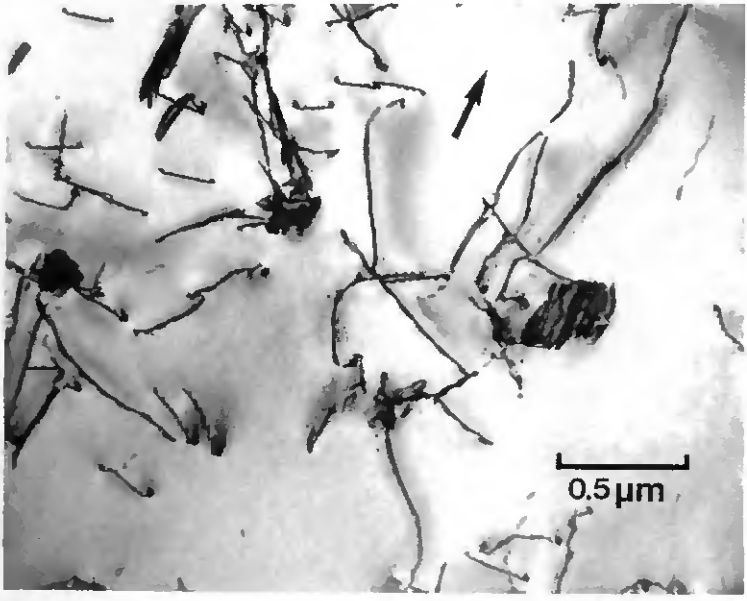

Figure 5.5: TEM micrograph of $Al_3(V,Ti)$ deformed 0.5 % at 300 °C. Foil orientation (010), diffraction vector 200.

6. Two Phase Materials

6.1 Introduction

Since even Al_3Ti-based intermetallic phases with a cubic crystal structure are probably intrinsically brittle, it is obvious to start the research for the combination of the good properties of these trialuminides (low density, good oxidation resistance, good strength at elevated temperatures) with the ductility of other materials. The two methods to improve ductility by creating a composite investigated within the frame of this work are:

- Embedding the brittle intermetallic in a ductile matrix. Such a type of aluminium base "superalloy" is prepared by mechanical alloying of elemental Al and Ti powder.

- Reinforcing the brittle intermetallic matrix with a ductile second phase. This composite is prepared by mixing intermetallic and element powder and HIP.

The results of both material developments are presented in the following section.

6.2 Mechanically Alloyed Al - Ti Materials

6.2.1 Evolution of the Powder Morphology

A detailed analysis of the Al-Ti alloys prepared by mechanical alloying (MA) is reported in ref. [80].

Figure 6.1a and 6.1b show the evolution of the degree of mixing of the elemental components within the Al-12.5%Ti alloy. During the initial stages of milling, a lamellar structure of welded elemental Al and Ti plates is produced. After 5 h milling (figure 6.1a), the coarsest lamellae are a few µm thick. Further milling leads to a refinement of the lamellae thickness. After 10 h milling (figure 6.1b), their thickness is close to the resolution of light microscopy. Still further milling leads to optically uniform powder particles but severe powder welding occurs and only a small fraction of the initial charge can be removed as useful powder. The decrease in particle size with increasing milling time is characteristic for all MA alloys presented here. The grains presented in figure 6.1 correspond to the largest size found in each powder charge. The shape of the powder particles up to a milling time of 10 h is relatively spherical, having a smoother surface with increasing milling time. For alloys containing more Ti a similar evolution of powder morphology is seen. For comparison, figure 6.1c illustrates the lamellar structure of a

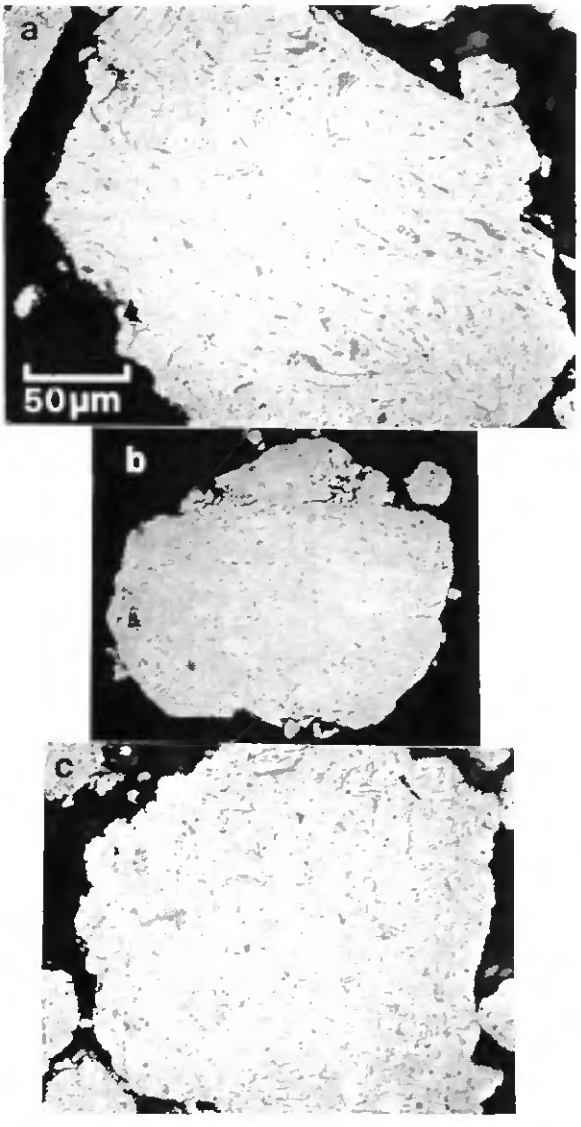

Figure 6.1: Evolution of the powder microstructure of the Al-12.5%Ti alloy after milling for a) 5 h and b) 10 h. c) shows the microstructure of the Al-25%Ti alloy after 5 h milling. Optical micrographs using Nomarski interference contrast.

Al-25%Ti powder particle after 5 h of milling. For alloys with a Ti content from 20 at.% to 26 at.%, severe powder welding began before 10 h milling. Consequently, the majority of the materials is prepared using a milling time of 5 h, giving rise to a fine lamellar structure similar to those in figure 6.1a and 6.1c. The lamellar spacing is sufficiently fine that chemical homogenization and Al_3Ti compound formation take place during subsequent annealing.

6.2.2 Microstructure of Consolidated Materials

Figures 6.2 to 6.4 show the microstructure of three different alloys after homogenization and consolidation. The microstructure of Al-12.5%Ti is illustrated in figure 6.2. This material is milled for 5 h, homogenized at 700 °C for 1 h and extruded at 500 °C. The 500 °C extrusion temperature is selected since at 400 °C the material is too hard to extrude, whilst at 600 °C severe cracking of the extruded material is seen. The microstructure is uniform and consists of particles of Al_3Ti (about 50 vol.%) in an aluminium matrix. The small dark particles are carbides, mostly of the type Al_4C_3, which originate from the organic process control agent added for milling. Some pores in the vicinity of large Al_3Ti particles or particle agglomerates are also observed.

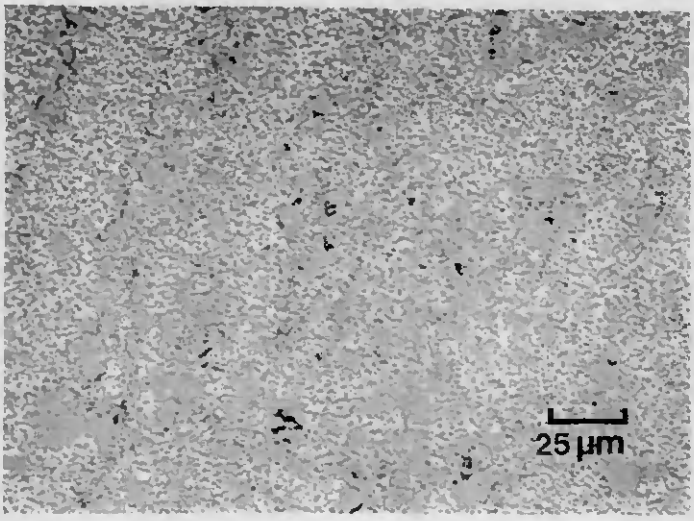

Figure 6.2: Microstructure of the Al-12.5%Ti alloy after 5 h milling, homogenization at 800 °C and extrusion at 500 °C. Optical micrograph.

Figure 6.3 shows the Al-20%Ti material after 5 h milling, homogenization at 800 °C and extrusion at 820 °C. Again the microstructure consists essentially of particles of Al_3Ti in an Al matrix, now with about 80 vol.% Al_3Ti. The amount of the dark carbide particles is considerably larger. The higher consolidation temperature probably enhances the formation of the carbides. No porosity is detected.

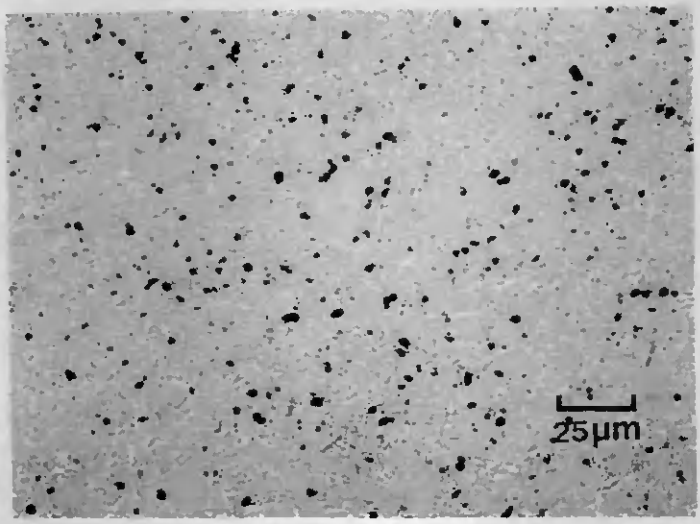

Figure 6.3: Microstructure of the Al-20%Ti alloy after 5 h milling, homogenization at 800 °C and extrusion at 820 °C. Optical micrograph.

Figure 6.4 illustrates the microstructure of Al-25%Ti after 5 h milling, homogenization at 800 °C and hot compaction at 1000 °C. Even after consolidation at such a high temperature, there is evidence of a considerable porosity and poorly bonded powder particles. The amount of carbides is similar to that observed in the Al-20%Ti material in figure 6.3. The microstructure of the Al-25%Ti material is characteristic for all Ti-rich alloys, namely for Al-24%Ti, Al-25%Ti and Al-26%Ti. Even at 1000 °C, these materials are too hard to extrude on the laboratory scale press used in the current work.

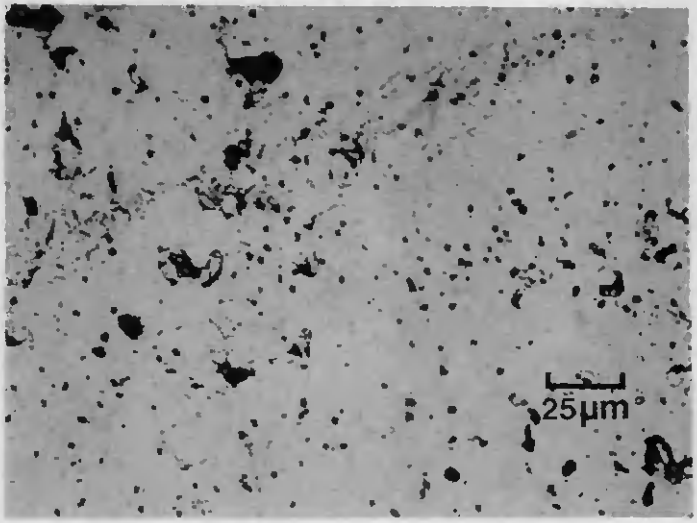

Figure 6.4: Microstructure of the Al-25%Ti alloy after 5 h milling, homogenization at 800 °C and hot compaction at 1000 °C. Optical micrograph.

6.2.3 Mechanical Testing

Tensile tests are restricted to samples of 12.5 % Ti extruded at 500 °C, while compression tests are carried out with all alloys. Table 6.1 summarizes the results of the tensile tests and table 6.2 those of compression testing.

homogenization temperature [°C]	0.2 % yield stress [MPa]	maximum stress [MPa]	reduction of area [%]
600	364	468	1.1
700	382	430	2.9
800	268	379	5.1

Table 6.1: Results of the tensile tests on Al-12.5%Ti material milled for 5 h and extruded at 500 °C.

The yield and maximum strength decrease generally as the homogenization temperatures increases, while at the same time the tensile ductility increases considerably. The material heat treated at 600 °C is not as homogeneous as the two samples annealed at 700 °C and 800 °C (cf. figure 6.2). The properties of this less homogeneous material are expected to be inferior than those of the other two samples.

alloy	consolidation temperature [°C]	0.2 % yield stress [MPa]	maximum stress [MPa]	reduction in length [%]
Al-12.5%Ti	500	340	553	7.5
Al-20%Ti (extruded)	700	490	664	7.8
	800	468	678	8.0
	820	503	625	5.3
	850	474	658	5.8
Al-20%Ti (compacted)	500	839	1295	2.2
	700	1202	1425	0.8
	800	792	947	0.2
Al-24%Ti	800	-	319	0.3
	900	-	734	0.2
	1000	-	894	0.2
Al-25%Ti	700	-	221	0.0
	900	-	357	0.1
	1000	-	795	0.2
Al-26%Ti	800	-	226	0.0
	900	-	278	0.1
	1000	-	449	0.1

Table 6.2: Results of the compression tests on Al-Ti alloys milled for 5 h. Al-12.5%Ti is homogenized at 700 °C all other materials at 800 °C.

Figure 6.5 illustrates graphically the influence of the Ti content and of the temperature used for extrusion (Al-12.5%Ti) or hot compaction (Al-20%Ti, Al-24%Ti, Al-25%Ti, and Al-26%Ti) on the strength of these alloys. For the more ductile materials the 0.2 % yield stress is shown, for the other very brittle materials, the maximum stress is taken. The 12.5 % Ti sample exhibits a strength of 340 MPa and a strain at failure of 7.5 %. The 20 % Ti material is sensitive to the consolidation temperature used. Compaction at 500 °C leads to a weaker but more ductile material. But this sample is not fully dense and the improved ductility may appear because of

densification during testing. Compaction at 700 °C leads to a very strong material with almost 1 % length change. Compaction at the highest temperature of 800 °C leads to a reduced strength and ductility. The 24 % to 26 % Ti alloys all fail in a brittle manner at a stress strongly dependent on the compaction temperature. The strength continues to increase up to the compaction temperature of 1000 °C, implying that still higher temperatures should be used for consolidation. If the compaction temperature is rised towards 1000 °C, all these three alloys begin to show signs of plastic deformation before failure, namely 0.1 % to 0.2 % length change.

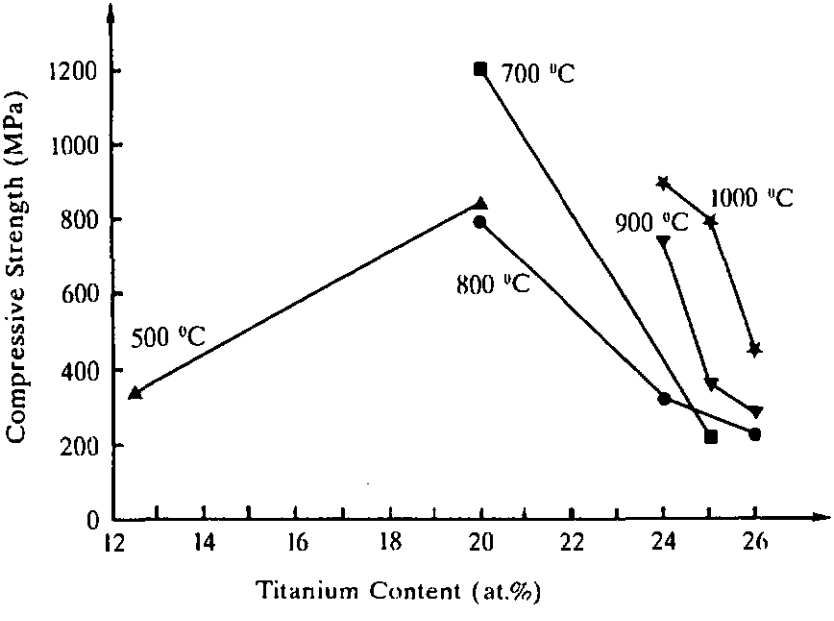

Figure 6.5: Compressive strength as a function of titanium content and of the temperature used for consolidation.

6.2.4 Discussion

Although the powder particles of Al-12.5%Ti and the more titanium-rich alloys have similar microstructures (cf. figure 6.1), the temperature of consolidation has a different influence on materials with either low or high Ti content. For Al-12.5%Ti, a lower homogenization temperature is seen to lead to higher strength. Experiments with a milling time of 12 h show that a fur-

ther gain in yield stress is possible using longer milling times. An optimum strength is reached milling the powders to a fine, almost homogeneous scale of elemental mixing and employing low temperatures of homogenization and consolidation. By this method, a very fine microstructure is maintained. However, in the present experiments the milling time is limited by severe welding of powders to the balls and container which occurs in spite of the process control agent. The coarsening of the microstructure observed after heat treatment at 700 °C or 800 °C suggests that only melting of the aluminium phase promotes the loss of the fine scale microstructure. Considering also the fact that extrusion of Al-12.5%Ti is impossible at 400 °C, the thermal stability and mechanical properties at intermediate temperatures are expected to be good for aluminium alloys.

Densification of this material is a question of filling the voids between the Al_3Ti phase. A temperature low enough to avoid coarsening but high enough for aluminium to form a continuous matrix will be the best compromise for consolidation. While coarsening leads to a decrease in strength and an increase in ductility, insufficient bonding of the Al phase is expected to reduce both strength and ductility. The strength of these MA alloys is related to the effectiveness of the milling process in producing a uniform dispersion of Ti within the Al powder particles, giving rise to a fine uniform dispersion of Al_3Ti in the final alloy. Further, since the Al_3Ti phase is likely to be well bonded to the Al matrix (having been formed "in-situ"), interface decohesion does not hinder plastical deformation, as is confirmed by fracture surface investigations (cf. ref. [80]).

For the materials richer in Ti, namely Al-24%Ti, Al-25%Ti and Al-26%Ti, the influence of homogenization temperature is opposite to that observed for Al-12.5%Ti, i.e. the strength increases with increasing annealing temperature. Furthermore, under the conditions of hot pressing used, it is not possible to effectively consolidate the materials with 24 % to 26 % Ti. The mechanisms involved in consolidation of these materials is completely different from the consolidation process in Al-12.5%Ti. In the latter case, hard Al_3Ti particles are embedded in a soft or even molten matrix during consolidation. For alloys with 24 % to 26 % Ti, there is no evidence of a soft second phase. They consist of nearly single phase Al_3Ti. Densification is a process of diffusional bonding and flow of the former powder particles. After homogenization, these particles are intermetallic Al_3Ti with a very fine microstructure and, probably, still cold worked from MA. It is obvious that a higher consolidation temperature means easier diffusion and better bonding and it is logical that samples compacted at higher temperatures exhibit better strength.

The stress at failure of this not optimally consolidated MA Al-25%Ti material is much greater than the maximum stress reported for cast Al_3Ti [12]. Such cast alloys have a very coarse microstructure with a grain size on the order of 1 mm and are very britle. The strength of the

MA material is still twice that of the closely related $Al_3(V,Ti)$ compound which has a grain size of about 20 µm (cf. table 4.3). This underlines the importance of the fine microstructure on the mechanical strength of the alloys prepared by mechanical alloying.

The compacted Al-20%Ti material exhibits both mechanisms, the drop in strength by consolidation at 800 °C due to structural coarsening as well as the lower strength at the 500 °C consolidation temperature due to insufficient bonding. Following extrusion, the strength of this alloy is considerably lower than after compaction at the same temperature (cf. table 6.2). Two reasons can be advanced to explain this difference. First, during extrusion there is a preferential extrusion of the softer Al phase such that the alloy becomes effectively poorer in Ti content. Second, during extrusion there is a significant adiabatic heating which leads to structural coarsening. Quantitative analysis confirms both, a higher apparent volume fraction of the Al phase as well as coarser Al_3Ti particles in the extruded material [80].

Comprehensively, near single phase Al_3Ti material prepared by MA exhibit very good strength at RT, but the milled powders are difficult to consolidate and the compression samples fail in a very brittle manner. Two phase Al-Al_3Ti materials, similar to Ni-γ superalloys, can be consolidated successfully on a laboratory scale. These alloys have promising mechanical properties and offer the potential to be developed as high temperature aluminium alloys. Properties comparative or better than those of sophisticated Al alloys (e.g. Al-8Fe-4Ce) can be expected.

6.3 Intermetallic Matrix Composites

6.3.1 Introduction

Brittle solids an be toughened by incorporating a ductile second phase into them, i.e. creating a composite. The physical mechanism of toughening is clear: if ductile ligaments bridge the advancing crack, they must stretch as the crack opens until they fracture or decohere. The work of stretching contributes to the energy absorbed to open the crack and increases the overall toughness of the composite. Figure 6.6 illustrates a crack advancing in a brittle matrix, intersected by ductile particles.

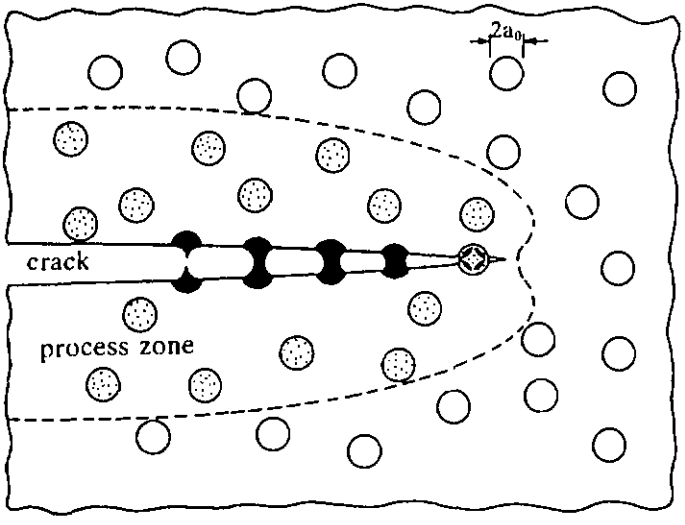

Figure 6.6: A crack in a brittle matrix, bridged by ductile particles.

If the particle is so weakly bonded to the matrix that it easily pulls free from the matrix as the crack approaches, then it is not stretched and there is almost no contribution to the toughness. Apart from decohesion, another mechanism can diminish the contribution to the toughness. If a brittle reaction zone forms between the particle and the matrix, an approaching crack will fracture this weak interface and incorporate it into its path. The ductile particle is not deformed plastically and does not absorb energy. Ashby, Blunt and Bannister show that the energy

absorbed in stretching the particle depends strongly on the degree of constraint [81]. They find that a completely adhering particle can constrain only poorly. Hence, an optimum in toughening effect is achieved if the particle decoheres partially from the matrix at the crack surface. The best effect on increasing the fracture toughness is observed when the particle-matrix interface strength is of the order of magnitude of the shear stress of the matrix.

6.3.2 Microstructure

Figure 6.7 shows the microstructures of HIPped Al_5Ti_2Fe powders mixed with different amounts of elemental Fe powder. In figure 6.7a, the volume fraction of Fe powder is 1.4 vol.%, in figure 6.7b 2.8 vol.%, and in figure 6.7c 5.5 vol.%. Optically, the material is completely dense, but contaminated with some dark appearing impurities. In the intermetallic matrix, the former spherical powder particles are still visible. Around the iron particles there are large reaction zones comprising at least two different layers. It seems that the elemental Fe dissolves in the Al_5Ti_2Fe matrix forming different intermetallic compounds. No chemical analysis of the reaction zones are performed but phases like Al_2FeTi, $AlFe_2Ti$ or $Al_2(Fe,Ti)$ are reported to occur in the ternary phase diagram [6]. The distribution of the Fe grains is not homogeneous over the whole section of the HIP can. There are zones of higher and lower densities of elemental Fe, but there seems to be no preferential site for these zones. All in all, the distribution of the ductile phase can be characterized as almost arbitrary with a slight tendency to form agglomerates. All micrographs in figure 6.7 are taken in zones of higher iron density. As expected, the microstructures of all three composites are very similar apart from the varying content of the Fe phase.

Figure 6.8 depicts composites based on an Al_5Ti_2Mn matrix and mixed with about 4 vol.% of different elemental metal powders, namely Nb, V and W. These materials are prepared by the same method as those presented above. This second series of intermetallic matrix composites seems to be completely dense. Figure 6.8a shows niobium particles in the Al_5Ti_2Mn matrix. As seen in the micrograph, this material is severely cracked after the HIP treatment. There is a large multi-layer reaction zone having a thickness of about 10 μm around each Nb grain. The outermost layer is optically anisotropic which gives rise to the speckled appearance under polarized light. According to the ternary Al-Ti-Nb phase diagram Al_3Ti and Al_3Nb are completely soluble in each other and the phases $AlNb_2$ and $AlNb_3$ have a large range of solubility for Ti [82, 83]. It is likely that the different layers are composed of phases structurally related to the four compounds mentioned before. For TiAl-Nb composites, the existence of the σ phase $AlNb_2$ is confirmed by the work of Evans, Bartlett, Davis, Flinn, Turner, and Reimanis [84]. The reaction zones seem to be very brittle considering the cracks following them. On the other

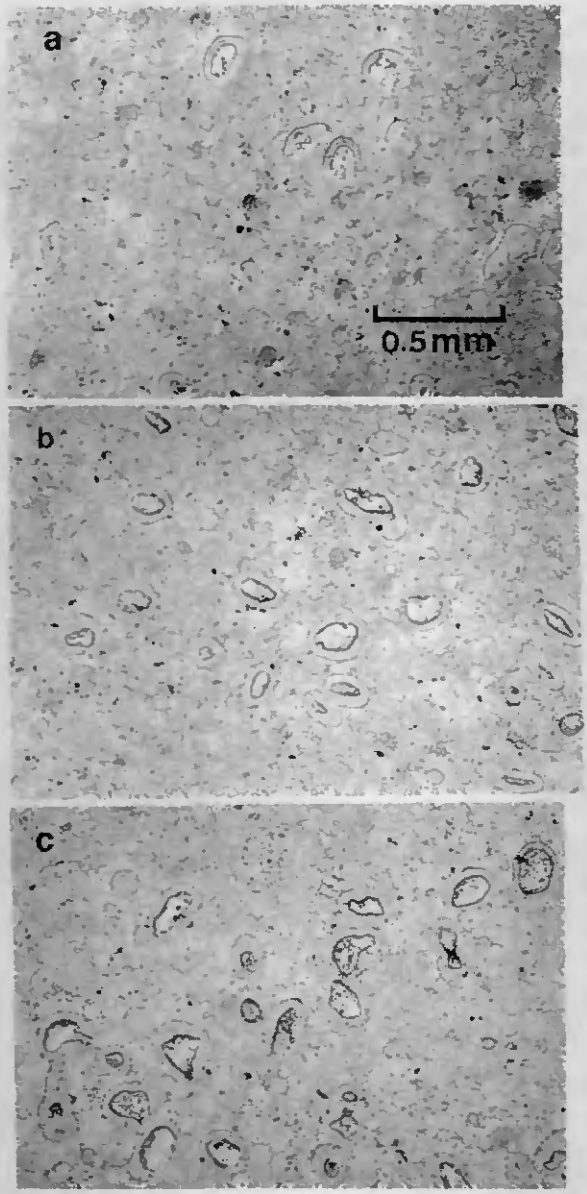

Figure 6.7: Al_5Ti_2Fe overspray powder mixed with different amounts of elemental Fe powder and HIPped. a) Al_5Ti_2Fe + 1.4 vol.% Fe, b) Al_5Ti_2Fe + 2.8 vol.% Fe, and c) Al_5Ti_2Fe + 5.5 vol.% Fe. Optical Micrographs.

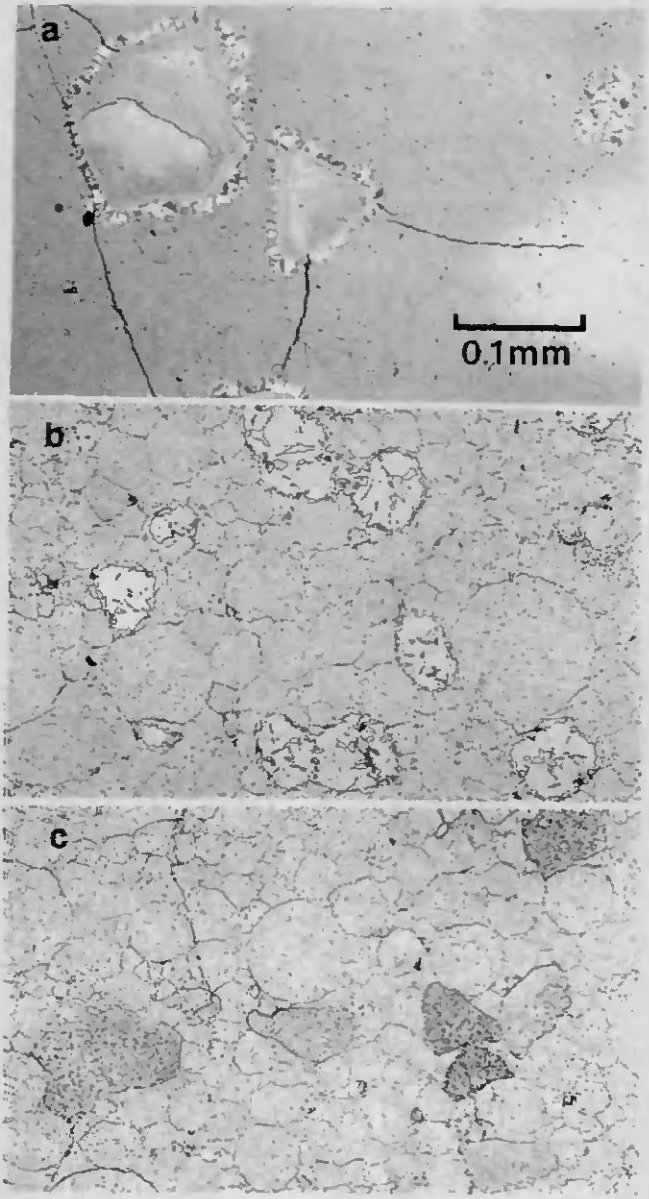

Figure 6.8: Al_5Ti_2Mn overspray powder mixed with about 4 vol.% of different elemental powders. a) Al_5Ti_2Mn + Nb, b) Al_5Ti_2Mn + V, and c) Al_5Ti_2Mn + W. Optical micrographs using polarized light.

hand, crack stopage is seen when the crack tip enters the Nb phase. The reaction zone around vanadium particles (figure 6.8b) is an order of magnitude smaller than that around Nb. In the V composite, the reaction zone consists presumably of Al_8V_5 which has a certain range of solubility for Ti [13]. In this sample, only minor cracking is observed after HIP consolidation. Figure 6.8c presents tungsten particles in the Al_5Ti_2Mn matrix. Optically no reaction zone between W and the intermetallic matrix is seen. This composite shows severe cracking after HIP. If a crack meets a W particle, it does not crack but it does not stop the crack either. The W phase seems not to affect the propagation of cracks.

6.3.3 Ductilization Effect

The aim of the addition of a second, ductile phase to the intermetallic matrix is increasing the toughness by hindering crack growth and bridging existing cracks by plastically deformable particles. Hence, hardness tests are performed to study the crack formation and propagation originating from the indentation (cf. section 4.2.2). Unfortunately, the Al_5Ti_2Mn + Nb and the Al_5Ti_2Mn + W composites are completely cracked, probably due to large differences in thermal expansion. In both materials a flawless zone large enough to assure undisturbed crack growth from an indentation cannot be found. For the Al_5Ti_2Mn + V material, a severely deformed region full of small cracks around the mark of the diamond pyramid and no long cracks starting from the indentation are observed. Consequently, for the Al_5Ti_2Mn based composites the influence of the ductile phase is studied on the existing cracks after HIP. Table 6.3 summarizes the results of the hardness tests and the observations on the crack paths.

composite	hardness [HV_{30}]	crack free load [kgf]	channelling of cracks along reaction zone	crack stop at ductile particles
Al_5Ti_2Fe + 1.4 % Fe	405	5	yes	yes
Al_5Ti_2Fe + 2.8 % Fe	383	3	yes	yes
Al_5Ti_2Fe + 5.5 % Fe	410	5	yes	yes
Al_5Ti_2Mn + Nb	261	-	yes	yes
Al_5Ti_2Mn + V	255	50	no	V particles crack
Al_5Ti_2Mn + W	246	10	no reaction zone	no

Table 6.3: Results of hardness tests and crack path studies.

The hardness of the composites is generally higher than that of the bulk material originating from the same spray deposition run as the overspray powder used as intermetallic matrix. The hardness of the spray deposited compounds is for Al_5Ti_2Fe (1^{st}) HV_{30} = 280 and for

Al_5Ti_2Mn HV_{30} = 183. Three reasons can be advanced to interpret this difference: firstly, the amount of impurities (mostly oxides) is likely to be higher in the HIPped material. Secondly, dissolution of the second phase leads to additional solution hardening and thirdly, the second phase particles act as reinforcement.

It is commonly seen that a crack meeting the ductile phase particle only at its border is channeled along the reaction zone and continues in the matrix behind the particle. This indicates that the reaction zones are generally even more brittle than the trialuminide matrix. Crack stopage can occur when the crack meets the reinforcement close to the middle of the particle. However, in the Al_5Ti_2Mn + V composite the vanadium phase cracks together with the matrix and in the Al_5Ti_2Mn + W material cracks are seen to be unaffected by the tungsten particles. In the latter case, the W particles seem to bridge the crack (cf. figure 6.8c). Both phenomena, crack channelling as well as crack stop are illustrated in figure 6.9 which shows a Vickers indentation in Al_5Ti_2Fe + 5.5 vol.% Fe material.

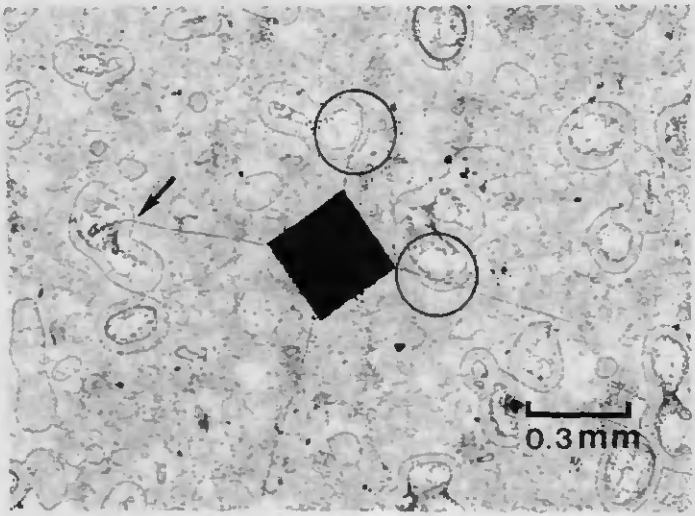

Figure 6.9: Vickers hardness indentation in Al_5Ti_2Fe + 5.5 vol.% Fe, applied load 30 kgf. Crack channelling along the reaction zone (marked by circles) and crack stopage at Fe particle (marked by an arrow) are seen. Optical micrograph.

Bend tests are carried out on Al_5Ti_2Mn + V material. Due obviously to a flaw, the first sample fails at 226 MPa already while a second test gives a strength of 420 MPa. Even this sample fails without the slightest indication of plastic deformation. This maximum stress is

considerably higher than that measured on spray deposited Al_5Ti_2Mn material (σ_{max} = 328 MPa). It seems that the V phase acts rather as strengthening than toughening reinforcement.

6.3.4 Discussion

A large reaction zone is seen to have a detrimental effect on the toughness of the composites. Cracks easily follow the brittle layer between the reinforcing phase and the matrix. Their path is hardly deviated by the second phase and the particles can obviously not bridge the crack. It must be assumed that almost all intermetallic compounds formed in the reaction zone are very brittle, independent of the element used as second phase. Hence, the search for good ductile reinforcements should focus on materials which form only a small reaction zone. No chemical reaction between the particles and the matrix contains the inherent risk of poor bonding between the two phases. Naturally, the reinforcement should be tougher than the matrix, not like the vanadium particles which often fracture in the same manner as the intermetallic surrounding them.

In this view-point, tungsten seems to be a candidate for ductile reinforcements because it bridges cracks. However, two questions remain open: first, how do the W particles behave if the crack opens more? - Do they decohere, fracture or constrain as would be most useful after the Ashby-Blunt-Bannister criterion [81]? Secondly, can cracking of the material during consolidation be avoided? Both questions can only be answered by further investigations. The second problem must be solved first to supply initially crack free material for crack propagation experiments.

The many cracks observed in the Al_5Ti_2Mn + W sample (as in Al_5Ti_2Mn + Nb) are likely to form during cooling after the HIP treatment at 1140 °C. Since no problems were encountered with the first Al_5Ti_2Fe + Fe series, the same industrial HIP cycle with a cooling time of about 3 h was used for the Al_5Ti_2Mn based composites. Bearing in mind that cracking is much less in Al_5Ti_2Mn + V, the differences in coefficients of thermal expansion, α, are thought to be responsible for the cracks formed during HIP. Table 6.4 gives an overview of the coefficients of thermal expansion of the materials concerned. No data are available for Al_5Ti_2M type trialuminides. For comparison, α for Al_3Ti is listed.

material	Al_3Ti	α-Fe	Nb	V	W
α [10^{-6} K^{-1}]	15	14.6	7.9	10.4	4.6
cracking	-	no	severe	minor	severe

Table 6.4: Coefficients of thermal expansion, α. The value for Al_3Ti is taken from [85] all other values from [56].

As seen in table 6.4, the amount of cracking observed in the different composites can be explained by the misfit of the coefficients of thermal expansion. In the Al_5Ti_2Fe + Fe composites, no cracking is observed as expected from the very similar values of α for Al_3Ti and Fe. The coefficient of thermal expansion for V is already one third smaller than α for Al_3Ti, consistent with the few cracks seen in the Al_5Ti_2Mn + V composite. The coefficient of thermal expansion for Nb and W is only one half or one third of the α for Al_3Ti, respectively, in agreement with the severe cracking observed in Nb and W reinforced materials. In the Al_5Ti_2Mn based composites, during cooling the intermetallic matrix contracts more than the metal particles, creating large internal stresses. Below the ductile-brittle transition, i.e. below about 650 °C, the trialuminide matrix cannot reduce these stresses by plastic tensile deformation. As seen for compression samples, tensile stresses beyond the elastic limit necessarily lead to local fracture of the loaded zone.

The problem of cracking can be overcome, on the one hand, by choosing a much lower cooling rate after HIP or, on the other hand, by employing reinforcing materials with a coefficient of thermal expansion close to that of Al_3Ti. Finally, it must be underlined that the subject of composites is not more than a supplement to the present work. The investigations have been interrupted at an early stage and no conclusive results can be offered.

7. Conclusions

It has been shown that Osprey spray deposition can be used successfully to prepare large quantities of intermetallics based on Al_3Ti. After HIP treatment, the deposited billets exhibit a reasonably fine microstructure with no sign of neither fine-scale and large-scale segregation nor porosity. Several types of contaminations are noted in the materials. These fine oxides and nitrides arise from reaction with the atomizing gas used during spray deposition. Other contaminants originate in the insufficient pre-casting and melting procedures used at the beginning of this work. It is important to avoid contamination from crucibles and containers, carefully control alloy composition and casting as well as spraying atmospheres. Improvements of the preparation technique are easily achieved. In fact, a recent third series of spray deposited materials is much cleaner than the earlier trialuminides reponed here.

Compression testing in the temperature range of -196 °C up to 700 °C enables to characterization of the Al_3Ti based intermetallics according to different mechanical properties:

Ductility:

- The DO_{22} $Al_3(V,Ti)$ alloy and the Al_5Ti_2Cu phase with the $L1_2$ structure fail in a very brittle manner at low and intermediate temperatures. While for $Al_3(V,Ti)$ the tetragonal crystal structure hinders the activation of a sufficient number of deformation systems, Al_5Ti_2Cu is additionally embrittled by extensive precipitation of basket weave like Al_2Ti plates.

- Al_5Ti_2Cr, $Al_5Ti_2(Mn,Cr)$, Al_5Ti_2Mn, and Al_5Ti_2Fe (1^{st}) exhibit a reasonable ductility in compression.

- Compared to Al_5Ti_2Fe (1^{st}), Al_5Ti_2Fe (2^{nd}) is strengthened and embrittled by Al_2Ti precipitates

- Al_5Ti_2Cr, $Al_5Ti_2(Mn,Cr)$, Al_5Ti_2Mn, and $Al_3(V,Mn)$ show a brittle-ductile transition at a temperature of about 650 °C.

Strength at RT:

- Al_5Ti_2Fe (2^{nd}) and Al_5Ti_2Cu have a yield stress exceeding 1000 MPa at RT. Both alloys are strengthened by the fine Al_2Ti basket weaves.

- The yield stress of Al_5Ti_2Cr, $Al_5Ti_2(Mn,Cr)$, Al_5Ti_2Mn, Al_5Ti_2Fe (1^{st}), and $Al_3(V,Mn)$ comprises the range of 340 MPa to 460 MPa at RT.

Strength as a function of temperature:

- None of the present trialuminides undergoes a significant drop in strength between -196 °C and 700 °C.

- Al_5Ti_2Cr, Al_5Ti_2Mn, and Al_5Ti_2Fe (1^{st}) show no marked increase in strength at cryogenic temperatures.

- Al_5Ti_2Fe (1^{st}) exhibits an anomalous strengthening, starting at about 500 °C and conserves increasing tendency at 700 °C. The increment in strength is about 50 MPa.

Work hardening rate:

- At RT and 500 °C, Al_5Ti_2Cr, $Al_5Ti_2(Mn,Cr)$, Al_5Ti_2Mn, and Al_5Ti_2Fe (1^{st}) exhibit a very high work hardening rate, almost constant with strain. At 700 °C, the work hardening rate decreases with increasing strain.

- In Al_5Ti_2Fe (2^{nd}), the work hardening rate drops with incraesing strain at these three temperatures.

The high work hardening rate is attributed to strong dipole formation and straight, relatively immobile screw dislocations. Bend testing at RT demonstrates the brittle behaviour of Al_5Ti_2M type trialuminides as tensile stresses are applied. In the best case, for Al_5Ti_2Mn, a plastic deformation of about 0.35 % is reached before failure occurs. Fracture surfaces show no sign of plasticity but an overwhelming amount of transgranular cleavage. Since fracture surfaces of samples failed during compression testing exhibit the same characteristics, the brittleness of $L1_2$ Al_3Ti based intermetallics is attributed to their inability to relax local stress concentrations by dynamic recovery and probably an intrinsic cleavage weakness.

In the relatively ductile alloys, namely Al_5Ti_2Cr, $Al_5Ti_2(Mn,Cr)$, Al_5Ti_2Mn, and Al_5Ti_2Fe (1^{st}), extensive serrated flow occurs in the temperature range of roughly 300 °C to 600 °C during compression testing. This phenomenon, the so called Portevin-LeChâtelier effect, is explained on the basis of segregation of solutes to the dislocation leading to a relaxation of the APB ribbon enclosed by the superdislocations. Such a relaxation is also observed on annealing Al_5Ti_2Fe (1^{st}) deformed at RT. The high fault energy of the shear APB is reduced during treatment in the critical temperature range for serrated flow. On an atomistic level, the

segregation of the substitutional atoms Cr, Mn and Fe to the superdislocations is thought to be responsible for the increase in dissociation distance. However, segregation of interstitial oxygen atoms to the dislocations cannot strictly be excluded as the reason for the serrated flow.

The segregation of atoms to the superdislocations has a mild strengthening effect. This strengthening is known as dynamic strain ageing and must be taken into account to interpret the yield stress at temperatures where the Portevin-LeChâtelier effect occurs.

In the temperature range between -196 °C and 700 °C, deformation is carried by the movement of $2 \cdot {}^1/_2\langle 110\rangle$ superdislocations. At low temperatures these dislocations are very closely separated and mobile on {111} planes. Solution hardening controls the deformation, as confirmed by activation volume measurements.

In Al_5Ti_2Fe (1^{St}), cross-slip is observed at higher temperatures. While at 500 °C cross-slip of the $2 \cdot {}^1/_2\langle 110\rangle$ superdislocations between {111} planes occurs, at 700 °C the dislocations slip from the initial octahedral glide planes onto the {010} planes. For this iron modified trialuminide, the increase in yield stress at these temperatures is explained by the {111} - {010} cross-slip. Dislocations are dissociated to a much larger extent than at low temperatures and the anisotropy factor of the APB energy on {111} and {010}, respectively, is estimated to be about 1.6. This anisotropy of the APB energy acts as driving force for cross-slip. Measurements of activation volume support this analysis of high temperature deformation mode.

For Al_5Ti_2Cr and Al_5Ti_2Mn, the measured activation volume is consistent with cross-slip at 650 °C and 700 °C only. This temperature interval coincides with the increase in ductility in compression observed in these two alloys. Cube cross-slip is not seen acting as strengthening mechanism by pinning dislocations in partially cross-slip configurations but as a mechanism for relaxation of local stress concentrations. At intermediate temperatures, the deformation of these materials is strongly influenced by the occurrence of dynamic strain ageing. This process, involving the increase of the dissociation width of the pair of ${}^1/_2\langle 110\rangle$ superpartials, can be advanced to explain the almost constant yield stress of Al_5Ti_2Cr and Al_5Ti_2Mn in the range of about 300 °C to 600 °C.

Although the brittleness of Al_3Ti base intermetallics has not been overcome during this work, these alloys bear a technically useful value. Applications as single-phase structural materials seem unlikely. Contrary, composites, comprising a trialuminium phase, like the two phase materials presented in chapter 6, have the potential to be developed to light weight, heat resistant materials. The good oxidation resistance makes Al_3Ti based compounds an interesting candidate as protective coatings for other high temperature materials.

Finally, the present work shows that mechanical properties and deformation mechanisms in apparently closely related intermetallic compounds can vary on a large scale. Findings for one of the Al_5Ti_2M type alloys cannot be generalized for the whole group of $L1_2$ trialuminides.

8. Abbreviations and Symbols

8.1 Abbreviations and Symbols Beginning with a Latin Letter

a	lattice parameter	[nm]
A	activation area	[m^2] or [b^2]
APB	antiphase boundary	
b	Burgers vector	[nm]
c	concentration of solutes	[-]
c	lattice parameter	[nm]
CSF	complex stacking fault	
d	dissociation distance of a superdislocation	[nm]
d_0	dissociation distance of a superdislocation during slip	[nm]
$\bar{d}$	equilibrium dissociation distance of a superdislocation	[nm]
D	diffusivity	[m^2s^{-1}]
DO_{22}	a tetragonal ordered crystal structure	
DSA	dynamic strain ageing	
fcc	face centered cubic	
g	diffraction vector	[m^{-1}]
HIP	hot isostatic pressing	
k	Boltzmann constant	[JK^{-1}]
k_r	rate constant for APB relaxation	[s^{-1}]
$L1_2$	fcc ordered crystal structure	
m_{Arr}	slope of an Arrhenius plot	[K]
MA	mechanical alloying	
n	slope of the logarithmic plot $\Delta\sigma$ vs t_a	[-]
NN	nearest neighbour	
Q_{APB}	activation energy of APB relaxation	[$kJmol^{-1}$]
Q_{SA}	activation energy of strain ageing	[$kJmol^{-1}$]
R	molar gas constant	[$Jmol^{-1}K^{-1}$]
S	order parameter	[-]
SISF	superlattice intrinsic stacking fault	
t_a	ageing time	[s]
t_w	waiting time of a dislocation pinned by an obstacle	[s]
T	absolute temperature	[K]
T_c	critical temperature of order-disorder transition	[K]
T_m	melting point	[K]
U	activation volume	[m^3] or [b^3]

8.2 Abbreviations and Symbols Beginning with a Greek Letter

α	coefficient of thermal expansion	[K^{-1}]
γ	APB energy	[mJm^{-2}]
γ_0	energy of an APB produced by shear	[mJm^{-2}]
γ_{010}	APB energy on {010} plane	[mJm^{-2}]
γ_{111}	APB energy on {111} plane	[mJm^{-2}]
$\bar{\gamma}$	equilibrium APB energy	[mJm^{-2}]
$\Delta\gamma$	change of APB energy during relaxation	[mJm^{-2}]
$\Delta\sigma_f$	strengthening at a fixed ageing time	[MPa]
$\Delta\sigma_{sat}$	saturation value of strengthening	[MPa]
$\Delta\sigma_{125}$	strengthening after 125 s	[MPa]
$\Delta\sigma_{1000}$	strengthening after 1000 s	[MPa]
ε	strain	[-]
$\dot{\varepsilon}$	strain rate	[s^{-1}]
λ	spacing between obstacles to dislocation slip	[nm]
λ_c	critical length of the pinned dislocation segment	[nm]
μ	shear modulus	[GPa]
ρ	density	[gcm^{-3}]
ρ_f	density of forest dislocations	[m^{-2}]
σ	mechanical stress	[MPa]
σ_a	stress applied during ageing	[MPa]
σ_{int}	internal stress	[MPa]
τ	shear stress	[MPa]
τ_{int}	internal shear stress	[MPa]

9. References

[1] Nicholson, D.M., Strocks, G.M., Temmermann, W.M., Sterne, P. and Pettifor, D.G., *MRS Symp. Proc.*, **133**, 17 - 22 (1989)

[2] Eberhart, M.E., Kumar, K.S. and MacLaren, J.M., *Phil. Mag. B*, **61**, 943 - 956 (1990)

[3] Morinaga, M., Saito, J., Yukawa, N. and Adachi, H., *Acta Metall. Mater.* **38**, 25 - 29 (1990)

[4] Pettifor, D.G., *Mat. Sc. Techn.* 4, 675 - 691 (1988)

[5] Raman, A. and Schubert, K., *Z. Metallkunde*, **56**, 99 - 104 (1965)

[6] Seibold, A., *Z. Metallkunde*, **72**, 712 - 719 (1981)

[7] Nic, J.P., Zhang, S. and Mikkola, D.E., *Scr. Met. et Mat.*, **24**, 1099 - 1104 (1990)

[8] Mabuchi, H., Hirukawa, K. and Nakayama, Y., *Scr. Met.*, **23**, 1761 - 1766 (1989)

[9] Zhang, S., Nic, J.P. and Mikkola, D.E., *Scr. Met. et Mat.*, **24**, 57 - 62 (1990)

[10] Massalski, T.B., Murray, J.L., Bennett, L.H. and Baker, H. (ed.), *Binary Alloy Phase Diagrams*, ASM, Metals Park, Ohio, 1986

[11] Villars, P. and Calvert, L.D., *Pearson's Handbook of Crystallographic Data for Intermetallic Phases*, ASM, Metals Park, Ohio, 1985,

[12] Yamaguchi, M., Umakoshi, Y. and Yamane, T., *Phil. Mag. A*, **55**, 301 - 315 (1987)

[13] Yamaguchi, M., Umakoshi, Y. and Yamane, T., *MRS Symp. Proc.*, **133**, 275 - 286 (1989)

[14] Yamaguchi, M. and Shirai, Y., *Dispersion Strengthened Aluminium Alloys*, TMS Symp. Proc., 721 - 741 (1988)

[15] Vanderschaeve,G. and Sarrazin, T., *phys. stat. sol.* (A) **43**, 459 - 646 (1977)

[16] Vanderschaeve,G., Sarrazin, T. and Escaig, B., *Acta Metall.* **27**, 1251 - 1260 (1979)

[17] Zhang, S. and Mikkola, D.E., *Scr. Met. et Mat.* **26**, 1315 - 1320 (1992)

[18] Mazdiyasni, S., Miracle, D.B., Dimiduk, D.M., Mendiratta, M.G. and Subramanian, P.R., *Scr. Met.*, **23**, 327 - 331 (1989)

[19] Kumar, K.S., *Int. Mat. Rew.* **35**, 293 - 327 (1990)

[20] Kumar, K.S. and Pickens, J.R., *Scr. Met.* 22, 1015 - 1018 (1988)

[21] Inui, H., Luzzi, D.E., Porter, W.D., Pope, D.P., Vitek, V. and Yamaguchi, M., *Phil. Mag. A* 65, 245 - 259 (1992)

[22] Rice, J.R. and Thomson, R., *Phil. Mag.* 29, 73 - 97 (1974)

[23] Turner, C.D., Powers, W.O. and Wert, J.A., *Acta Metall.*, **37**, 2635 - 2643 (1989)

[24] George, E.P., Porter, W.D., Henson, H.M., Oliver, W.C. and Oliver, B.F., *J. Mater. Res.* **4**, 78 - 84 (1989)

[25] George, E.P., Horton, J.A., Porter, W.D. and Schneibel, J.H., *J. Mater. Res.* **5**, 1639 - 1648 (1990)

[26] Fu, C.L., *J. Mater. Res.* 5, 971 - 979 (1990)

[27] Cottrell, A.H., *Dislocations and Plastic Flow in Crystals*, 2, 1961

[28] van den Beukel, A., *phys. stat. sol.*, **30**, 197 - 206 (1975)

[29] Kubin, L.P. and Estrin, Y., *Acta Metall. Mater.*, **38**, 697 - 708 (1990)

[30] Friedel, J., *Dislocations*, Pergamon Press, Oxford, 1964

[31] Fleischer, R.L., *Acta Metall.*, **9**, 996 - 1000 (1961)

[32] Labusch, R., *phys. stat. sol.*, **41**, 659 - 669 (1970)

[33] Brown, N., *Phil. Mag.*, **4**, 693 - 704 (1959)

[34] Popov, L.E., Kozlov, E.V. and Golosov, N.S., *phys. stat. sol.*, **13**, 569 - 575 (1966)

[35] Popov, L.E., Golosov, N.S. and Ginzburg, A.E., *Ordered Alloys - Structural Applications and Physical Metallurgy*, 3, 307 - 319 (1970)

[36] Morris, D.G., Besag, F.M.C. and Smallman, R.E., *Acta Metall.*, **22**, 801 - 811 (1974)

[37] Besag, F.M.C., Morris, D.G. and Smallman, R.E., *Acta Metall.*, **22**, 813 - 817 (1974)

[38] Schoeck, G. and Korner, A., *Phil. Mag. A*, **61**, 917 - 928 (1991)

[39] Kear, B.H. and Wilsdorf, H.G.F., *Metall. Transactions (AIME)*, **224**, 382 - 386 (1962)

[40] Thornton, P.H., Davies, R.G. and Johnston, T.L., *Metall. Transactions A*, **1**, 207 - 218 (1970)

[41] Takeuchi, S. and Kuramoto, E., *Acta Metall.*, **21**, 415 - 425 (1973)

[42] Yamaguchi, M., Paidar, V., Pope, D.P. and Vitek, V., *Phil. Mag. A*, **45**, 867 - 882 (1982)

[43] Paidar, V., Yamaguchi, M., Pope, D.P. and Vitek, V., *Phil. Mag. A*, **45**, 883 - 894 (1982)

[44] Pope, D.P. and Ezz, S.S., *Int. Metals Rew.*, **29**, 136 - 167 (1984)

[45] Paidar, V., Pope, D.P. and Vitek, V., *Acta Metall.*, **32**, 435 - 448 (1984)

[46] Cagnon, M., *Dislocation et déformation plastique* (edited by Groh, P., Kubin, L.P. and Martin, J.L.), p. 53 - 66. Diffusion des Editions de physique, Société Française de Physique (1979)

[47] Groh, P., *Dislocation et déformation plastique* (edited by Groh, P., Kubin, L.P. and Martin, J.L.), p. 67 - 75. Diffusion des Editions de physique, Société Française de Physique (1979)

[48] Haasen, P., *Physikalische Metallkunde (2. ed)*, p. 201. Springer, Berlin, 1984

[49] Biget, M.P. and Saada, G., Phil. Mag. A **59**, 747 - 757 (1989)

[50] Morris, D.G. and Günter, S., to be published

[51] Lerf, R. and Morris, D.G., *Acta Metall. Mater.*, 39, 2419 - 2430 (1991)

[52] Anstis, G.R., Chanticul, P., Lawn, B.R. and Marshall, D.B., *J. Amer. Cer. Soc.*, **64**, 533 - 543 (1981)

[53] Dadras, P., *Metals Handbook*, Vol. 8, 9, p. 118, ASM, Metals Park (1985)

[54] Burt, H., Dennison, J.P. and Wilshire, B., *Metal Science* **13**, 295 - 300 (1979)

[55] Gibbs, G.B., *Phil. Mag. A*, **13**, 317 - 329 (1966)

[56] Brandes, E.A. (ed.), *Smithells Metals Reference Book* **6**, Butterworth, London, 1983

[57] Potez, L., Lapasset, G. and Kubin, L.P., *Scr. Met. et Mat.*, **26**, 841 - 846 (1992)

[58] Kawabata, T., AbumiyaT. and Izumi, O., *Acta Metall. Mater* **40**, 2557 - 2567 (1992)

[59] Morris, D.G, *J. Mater. Res.*, **7**, 303 - 312 (1992)

[60] George, E.P., Pope, D.P., Fu, C.L. and Schneibel, J.H., *ISIJ Int.* 10/91 (1991)

[61] Yoo, M.H., *Acta Metall.* **35**, 1559 - 1569 (1987)

[62] Morris, D.G., *Scr. Met. et Mat.*, **25**, 712 - 716 (1991)

[63] Morris, D.G., *Phil. Mag. A*, **65**, 389 - 401 (1992)

[64] Baluc, N.L., Doctoral Thesis EPF Lausanne, **886** (1990)

[65] Brown, S.A., Kumar, K.S. and Whittenberger, J.D., *Scr. Met. et Mat.* **24**, 2001 - 2006 (1990)

[66] Mabuchi, H., Hirukawa, K., Tsuda, H. and Nakayama, Y., *Scr. Met. et Mat.* **24**, 505 - 508 (1990)

[67] Zhang, S., Nic, J.P., Milligan, W.W. and Mikkola, D.E., *Scr. Met. et Mat.* **24**, 1441 - 1446 (1990)

[68] DiPietro, M.S., Kumar, K.S. and Whittenberger, J.D., *J. Mater. Res.* 6, 530 - 538 (1991)

[69] Mishima, Y., Oya, Y. and Suzuki, T., *MRS Symp. Proc.* 39, 263 - 277 (1984)

[70] Wee, D.-M., Noguchi,O., Oya, Y. and Suzuki, T., *Trans. JIM* **21**, 237 - 247 (1980)

[71] Kumar, K.S. and Brown, S.A., *Phil. Mag. A* **65**, 91 - 109 (1992)

[72] Kumar, K.S. and Brown, S.A., *Acta Metall. Mater.* **40**, 1923 - 1932 (1992)

[73] Pugh, S.F., *Phil. Mag.* 45, 823 - 843 (1954)

[74] Kumar, K.S., Herring R.A. and Whittenberger, J.D., 1990 TMS Annual Meeting, Anaheim, CA (in *JOM* **41**, 92 (1989))

[75] Mabuchi, H., Hirukawa, K., Katayama, Y.K.,Tsuda, H. and Nakayama, Y., *Scr. Met. et Mat.* **24**, 1553 - 1558 (1990)

[76] van Loo, F.J.J. and Rieck, G.D., *Acta Metall.* **21**, 61 - 71 (1973)

[77] Kumar, K.S. and Whittenberger, J.D., *J. Mater. Res.* **7**, 1043 - 1045 (1992)

[78] Larikov, L.N., Geichenko, V.V. and Fal'chenko, V.M., *Diffusion Processes in Ordered Alloys*, p. 123. Oxonian Press, New Delhi ,1981

[79] Hug, G., Douin, J. and Veyssière, P., *MRS Symp. Proc.* **133**, 125 - 130 (1989)

[80] Lerf, R. and Morris, D.G., *Mat. Sc. Eng.* **A128**, 119 - 127 (1990)

[81] Ashby, M.F., Blunt, F.J. and Bannister, M., *Acta Metall.* **37**, 1847 - 1859 (1989)

[82] Bendersky, L.A. and Boettinger, W.J., *MRS Symp. Proc.* **133**, 45 - 50 (1989)

[83] Dève, H.E., Evans, A.G., Odette, G.R., Mehrabian, R., Emiliani, M.L. and Hecht, R.J., *Acta Metall. Mater.* 38, 1491 - 1502 (1990)

[84] Evans, A.G., Bartlett, A., Davis, J.B., Flinn, B.D., Turner, M. and Reimanis, I.E., *Scr. Met. et Mat.* **25**, 1003 - 1010 (1991)

[85] Smialek, J.L., Gedwill, M.A. and Brindley, P.K., *Scr. Met. et Mat.* **24**, 1291 - 1296 (1990)

Acknowledgements

Foremost, I would like to thank the director of my thesis, Professor D.G. Morris. His enthusiasm encouraged me and his good advice accompanied my work in the last three and a half years. I am thankful for the many fruitful discussions during which I learnt much from his great experience.

Further, I give thanks to:

- Professor W. Form, former director of the "Institut de Métallurgie Structurale", for the friendly reception and for accepting to be a member of the jury.

- Professor J.L. Martin of the "Ecole Polytechnique Fédérale de Lausanne" and Dr. P. Furrer from Alusuisse-Lonza, Neuhausen, who kindly accepted to examine this thesis.

- Mr. G. Höllrigl from Alusuisse-Lonza, Neuhausen, for the skillful work of preparing the materials.

- All collaborators of the "Institut de Métallurgie Structurale" for their direct and indirect contribution to the realization of the present work.